Technical Report

TR-03-05

Inspection of copper canisters for spent nuclear fuel by means of ultrasound

Nonlinear acoustics, synthetic aperture imaging

Fredrik Lingvall, Ping Wu, Tadeusz Stepinski
Uppsala University, Signals and Systems,
Department of Materials Science

March 2003

Svensk Kärnbränslehantering AB
Swedish Nuclear Fuel
and Waste Management Co
Box 5864
SE-102 40 Stockholm Sweden
Tel 08-459 84 00
+46 8 459 84 00
Fax 08-661 57 19
+46 8 661 57 19

Inspection of copper canisters for spent nuclear fuel by means of ultrasound

Nonlinear acoustics, synthetic aperture imaging

Fredrik Lingvall, Ping Wu, Tadeusz Stepinski
Uppsala University, Signals and Systems,
Department of Materials Science

March 2003

Abstract

This report contains results concerning inspection of copper canisters for spent nuclear fuel by means of ultrasound obtained at Signals and Systems, Uppsala University in year 2001/2002.

The first chapter presents results of an investigation of a new method for synthetic aperture imaging. The new method presented here takes the form of a 2D filter based on minimum mean squared error (MMSE) criteria. The filter, which varies with the target position in two dimensions includes information about spatial impulse response (SIR) of the imaging system. Spatial resolution of the MMSE method is investigated and compared experimentally to that of the classical SAFT and phased array imaging. It is shown that the resolution of the MMSE algorithm, evaluated for imaging immersed copper specimen is superior to that observed for the two above-mentioned methods.

Extended experimental and theoretical research concerning the potential of nonlinear waves and material harmonic imaging is presented in the second chapter. An experimental work is presented that was conducted using the RITEC RAM-5000 ultrasonic system capable of providing a high power tone-burst output. A new method for simulation of nonlinear acoustic waves that is a combination of the angular spectrum approach and the Burger's equation is also presented. This method was used for simulating nonlinear elastic waves radiated by the annular transducer that was used in the experiments.

Contents

Chapter 1

Introduction

1.1 Outline of the Report

Reliable detecting and sizing natural defects in EB welds sealing copper canisters for spent nuclear fuel using ultrasound requires applying advanced ultrasonic imaging techniques. In this report we are presenting our recent results concerning inspection of copper canisters for spent nuclear fuel by means of ultrasound.

Our research activity in this project in year 2001/2002 consisted of two separate main tasks:

- Synthetic Aperture Imaging
- Nonlinear Acoustics

The first task is concerned mainly with an investigation of a new method of synthetic aperture imaging and its comparison to the synthetic aperture focusing technique (SAFT) and the traditional phased array (PA) imaging. The new method presented here is a 2D filter based on minimum mean squared error (MMSE) criteria. Spatial resolution of the MMSE method is investigated and compared experimentally to that of classical SAFT and PA imaging.

The second task includes extended experimental and theoretical research concerning the potential of nonlinear waves and material harmonic imaging. An experimental work is presented that was conducted using the RITEC RAM-5000 ultrasonic system capable of providing a high power tone-burst output. A new method of simulation of nonlinear acoustic waves that is a combination of the angular spectrum approach and the Burger's equation is also presented. This method was used for simulating nonlinear elastic waves radiated by the annular transducer that was used in the experiments.

The third task planned for this year, *Wave phase conjugation* dealing with experimental study of phase conjugation technique for imaging EB welds is not covered in this report since no significant results have been achieved. This task has been conducted in collaboration with *Ecole Centrale de Lille, Groupe Acoustique at Electronique* who has been responsible for the experimental part. Difficulties in modifying the experimental setup in Lille as well as the properties of the inspected material (such as, for example, its high attenuation) are the main reason for the lack of success in the experimental work.

The fourth task planned for this period, *Signal processing toolbox* has been started recently in form of diploma work and will be completed in the beginning of 2003. This task is concerned with practical implementation of signal processing algorithms for the needs of SKB's Canister Laboratory in Oskarshamn.

Chapter 2

Nonlinear Acoustics

2.1 Introduction

In this report we present current results of the research task that started three years ago. Inspired by the tissue harmonic imaging technology widely applied in ultrasonic medicine, in 2000 we initiated an experimental study concerning nonlinear acoustics [1, 2], followed by a theoretical study of nonlinear waves in 2001 [3]. The progress reported here concerns both theory and experiments.

The main goal of this research is exploiting the potential of nonlinear waves and harmonics for material harmonic imaging, material characterization, and evaluation of welds in copper.

The linear relation between stress and strain in an elastic medium defined by the Hooke's law is true only for ideal linear elastic media that seldom exist in reality. This law is commonly used since it serves as a good approximation assuming that stress is infinitesimal and the medium of interest is homogeneous in elastic properties. It is worth noting that most linear theories applied in acoustics and elastics have been established by using linearization under the assumption of infinitesimal amplitudes of acoustic or elastic waves propagating in homogeneous media. For example, a nonlinear term in the relation of the strain tensor with the derivatives of the particle displacements with respect to the coordinates is normally neglected [4].

However, materials in nature are in general nonlinear, and it is not unusual that the amplitudes of ultrasonic waves used for the inspection (for instance, in focal zone of a focused transducer) are so large that the assumption of infinitesimal disturbance fails. For example, copper used for canisters is, like other metals, nonlinear. When an infinitesimal amplitude elastic wave propagates in copper, Hooke's law is an good approximation because the nonlinear elasticity of a material is insignificant. For larger amplitudes the stress-strain relation does not obey the Hooke's law, which means that the nonlinear term in this relation becomes significant. Intensive ultrasonic waves, usually called finite-amplitude ultrasonic waves (in contrast to infinitesimal amplitude waves) are used to investigate the nonlinear properties of solids. The amount of nonlinearity observed in solids is described in terms of third- and higher-order elastic constants. Results of studies reported in [5–8], conducted using finite-amplitude ultrasonic waves, have demonstrated that a pure (single crystal) copper metal has in addition to the linear (second-order) elastic constant nonlinear, i.e., third-, forth- and higher-order elastic constants. Copper's nonlinearity can be attributed to the intrinsic anharmonicity of its atomic lattices. This nonlinearity results in a nonlinear distortion of an initially sinusoidal wave that becomes a nonlinear wave. In the frequency domain the nonlinear distortion reveals itself by additional harmonic components (multiples of the fundamental frequency).

Summarizing, the nonlinear elastic properties of copper can be revealed using an intensive finite-amplitude ultrasound. Obviously, in such case propagation of the ultrasonic waves cannot be treated appropriately with any linear theories.

Application of nonlinear ultrasonic waves (NUW) and harmonics to nondestructive characterization of materials has been reported for more than four decades. In the early works nonlinear ultrasound and harmonics were used to determine the third- and higher-order elastic constants (related to nonlinear elastic properties) of materials [5–9]. The third-order elastic (TOE) constants play a primary role in characterizing the anharmonic and nonlinear properties of solids. Rapid progress in the application of the NUW to NDE has been observed in the last decade. The NUW have been used for evaluating material fatigue and degradation [10–13], for detecting and locating fractured inhomogeneities and defects [14–20], for assessing adhesive joints and bonds [21, 22] and fusion-welds [23], and for conducting material harmonic imaging [1, 2].

Two general sources of nonlinearities can be distinguished for solids: the *geometrical nonlinearity* and the *intrinsic physical nonlinearity* [24]. The geometrical nonlinearity, which does not depend on the material properties arises from the nonlinear connection of the strain tensor

components with the derivatives of the particle displacements with respect to the coordinates. Anharmonicity of the atomic lattice in single crystals may be the source of the intrinsic nonlinearity. For crystals with lattice imperfections (such as dislocations, interstitial, etc.) and polycrystalline solids with precipitate coherency strains, the dislocations are another source of the intrinsic nonlinearity [7, 8, 25–27]. The existence of both nonlinearities makes the stress-strain relation nonlinear resulting in the nonlinear elastic material properties.

When a solid material contains fractured inhomogeneities like defects, micro-cracks, interfaces, etc., its nonlinearity may become anomalously large [14–18, 28]. The nonlinearity induced by inhomogeneities is considerably larger than the intrinsic nonlinearity of the material that is intact.

Recently, a very interesting type of acoustic nonlinearity , called *contact acoustic nonlinearity* (CAN), has attracted attention of researchers in NDE [15–20]. CAN occurs in solids containing cracks and interfaces that may close, that is, their surfaces are in temporary contact with each other when the solids are subject to an intense ultrasound. Welded material with an anomaly known as *kissing bond* or an adhesive-jointed material with a contact non-bonded interface may be named here as examples. The anomalously high nonlinearity, the CAN, arises from the asymmetric elastic vibrations of the kissing faces caused by the intense sound waves. It should be pointed out that kissing-face defects and kissing bonds often exhibit weak reflections and are practically invisible using a linear acoustic reflection mode, while nonlinear waves may enable a very high detection sensitivity [12, 13, 21]. This fact is the primary reason motivating our present research – CAN may appear as a valuable tool for detecting microcracks and kissing bonds in the FSW welds in copper canisters.

Another motivation arises from the fact that nonlinear waves carry much broader spectrum of information on materials' properties comparing to the linear waves, so that the use of the nonlinear waves certainly extends the scope of the existing ultrasonic nondestructive evaluation. Considerable development of applications of nonlinear ultrasound to NDE has resulted in a new term *nonlinear NDE* (NNDE) [15, 16].

We have started this task from a preliminary experimental investigation of nonlinear ultrasonic waves in copper and an evaluation of a simple material harmonics imaging technique [1, 2]. The experimental investigation was performed using Matec TB-1000 PC plug-in card that was used for generating a tone-burst excitation to an ultrasound transducer. Our ALLIN ultrasonic system was used for acquiring data and positioning of a specially designed annular array. A preliminary theoretical study of nonlinear waves followed this step [3]. This study was limited to the case of nonlinear plane waves propagating in fluids.

This report presents an extended experimental and theoretical research conducted recently.

Our experimental setup for harmonic imaging has been upgraded, the Matec TB-1000 card was replaced with the RITEC RAM-5000 ultrasonic system that has a considerably better performance. Since harmonic components observed in ultrasonic signals received from solids are relatively weak it is essential to ensure that any element of the measurement channel (such as, a hydrophone, an amplifier or a pulse generator) does not introduce harmonics with amplitudes comparable with those generated in the inspected solid specimen. Therefore, we started from a thorough evaluation of our new RITEC system that plays a fundamental role in our measurements to ensure that it does not introduce any significant harmonics. A broadband hydrophone made by Precision Acoustics Ltd, was used in the measurements of nonlinear acoustic fields in water radiated by the annular array that was excited by a narrow-band tone-burst from the RITEC system.

The use of RITEC system with the ALLIN system enabled harmonic imaging of material specimens using both nonlinear longitudinal waves (NLW) and shear waves (NSW). To investigate the feasibility of various wave modes and beam types for harmonic imaging, in our

experiments, we used both normal and angled longitudinal waves as well as angled shear waves for harmonic imaging of copper.

Our theoretical work was concerned with simulating nonlinear acoustic and elastic waves radiated by the annular array that was used in the experiments. In the theoretical investigation, we have extended our previous work [1, 3] by calculating nonlinear acoustic beams in water and nonlinear elastic beams in immersed copper. The aim of the theoretical work was to create a tool making possible quantitative interpretation of the experimental results and enabling deeper understanding how nonlinear waves evolve during their propagation. Such a tool is very helpful in finding those features of harmonic fields that may appear to be useful for NNDE.

Results of this work are presented here in three separate sections: evaluation of experimental setups, material harmonic imaging, and simulations. The evaluation section starts from presenting results of the evaluation of the RITEC RAM-5000 ultrasonic system, which is followed by the results of hydrophone measurements of nonlinear acoustic beams that were radiated in water by the annular array. Selected results of material harmonic imaging obtained using NLW and NSW for the imaging of copper specimens are presented in the second section. In the third section we present the simulated nonlinear acoustic beams radiated by the focused transducer into water and nonlinear elastic fields evoked in the immersed copper.

2.2 Evaluation of experimental setups

Many works reporting the measurements of nonlinear acoustic waves from the transducers with different geometries, for example, planar circular and rectangular transducers, spherically focused transducers, can be found in the relevant literature [29–33].

2.2.1 Experimental setups

Our experiments required two slightly different setups, first for measuring nonlinear acoustic fields in water, and the second for investigating different types of nonlinear waves for material harmonic imaging. Those experimental setups are shown in Figure 2.1.

The setup for measuring nonlinear acoustic fields radiated by the annular array is shown at the right hand side of Figure 2.1. It consists of a hydrophone, a preamplifier, a digital oscilloscope and a computer. The hydrophone, used as receiver, is from Precision Acoustics Ltd, UK and calibrated by National Physics Laboratory, UK and has an active element of diameter 0.2 mm and a broad bandwidth extending from 200 kHz to 30 MHz.

The main setup that was used for harmonic imaging of materials (that is copper specimens immersed in water) consists of the two-element annular array, the ALLIN ultrasonic array system, and the RITEC RAM-5000 ultrasonic system. The advanced ultrasonic measurement system RAM-5000 from RITEC Inc., USA, replaced the MATEC TB-1000 plug-in card used in our previous research [1, 3]. The RAM-5000 ultrasonic system was used in this setup for generating narrow-band (tone-burst) excitation to the transmitting transducer as well as for amplifying and filtering signals received by the receiving transducer. The ALLIN ultrasonic array system is used for acquiring data and positioning transducers.

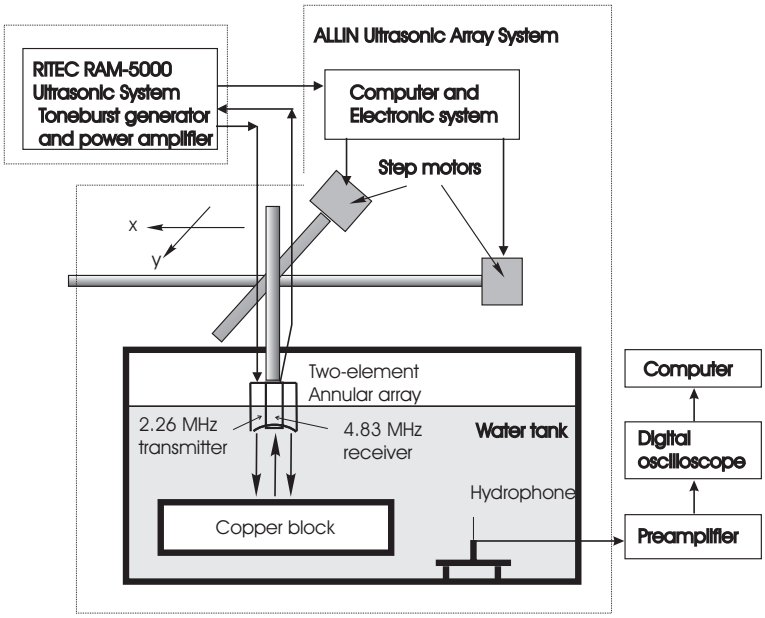

Figure 2.1: Experimental setups.

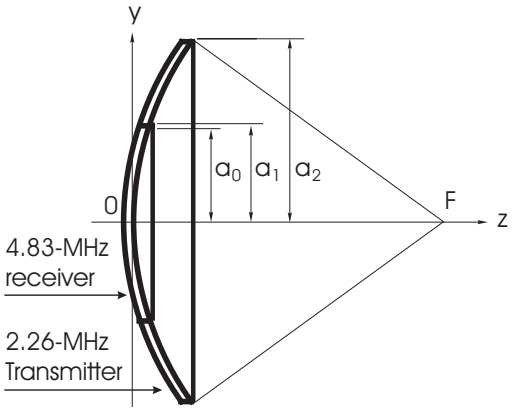

Figure 2.2: Geometry of the annular array. The inner element is used as a receiver with 4.83-MHz center frequency, and the annular outer element as a transmitter. Both elements have the same radius of curvature F = 210 mm.

The two-element annular array (see Figure 2.2) is made up of two spherically concentric elements with radius of curvature of F = 210 mm. The inner element is circular with radius a_0 =10 mm, and has a 4.83-MHz center frequency with a 73% bandwidth. The annular outer element with an inner radius a_1 =10 mm and an outer radius a_2 =19 mm has a 2.26-MHz center frequency and a bandwidth of 69%.

The RITEC RAM-5000 ultrasonic system is a stand-alone system that has a built in gated power amplifier, which can generate a tone-burst output with the adjustable pulse duration, frequency, and amplitude. The output voltage could be adjusted in 100 steps (nonuniform), ranging from some tenths of volt up to one thousand V_{pp} (peak-to-peak) measured when the the outer element of the annular array was connected. RAM-5000 parameters and versatility enabled an accurate examination of the variation of ultrasonic nonlinearity as a function of the excitation amplitude. The tone-burst frequency could be changed from 200 kHz to 20 MHz with a minimum step of 10 kHz, and the burst duration could be adjusted from 0 to 255 cycles in

1-cycle steps or from 0 to 1024 in 4-cycle steps.

The RITEC system has a built-in broadband receiving amplifier with adjustable gain up to 78 dB. The amplifier is provided with a high-pass (HP) filter with three-step adjustable cutoff frequencies of 0.25, 1 and 4 MHz, and a low-pass (LP) filter with cutoff frequencies of 5, 10 and 20 MHz. Various combinations of the cutoff frequencies of the high- and low-pass filters enable creating band-pass filters with nine different bandwidths.

As shown in Figure 2.2 the tone-burst produced by the output of gated amplifier in the RITEC system excites the transmitter (the 2.26-MHz outer element), and the RITEC receiver amplifier with a BP filter is connected to the 4.83-MHz inner element that receives echoes from the inspected materials.

2.2.2 Evaluation of the RITEC RAM-5000 ultrasonic system

The RITEC RAM-5000 ultrasonic system played a fundamental role in our measurements. It generated a narrow band excitation (a tone-burst) to the transmitter, and it amplified and filtered the signals received by the receiving transducer. Any harmonics produced by the RITEC system itself would result in errors in the measurements. Therefore, we started from a systematic investigation of nonlinear distortion introduced by the system. More specific, we have checked spectra of the RITEC tone-burst output, and the distortion introduced by the BP filters for different frequency bandwidths.

Tone-burst output from the RITEC RAM-5000 ultrasonic system

Frequency spectrum of the tone-burst output from the RITEC RAM-5000 gated amplifier loaded with the transmitting transducer was analyzed. This was done to check level of harmonics present in the tone-burst, that is, to estimate potential error due to introducing unwanted harmonics to the transducer.

The tone-bursts from the RITEC system loaded with the 2.26-MHz transducer were measured using Tektronix TDS-210 digital oscilloscope. Some examples of the measured waveforms are shown in Figure 2.3(a) and (c), and their spectra plotted in semi-logarithmic scale are shown in Figure 2.3(b) and (d), respectively. Both tone-bursts consist of 8 cycles a 2.3-MHz sine-wave with different amplitudes. That in Figure 2.3(a) has an amplitude of 28 V_{pp} (where pp stands for peak-to-peak). Its spectrum in Figure 2.3(b) shows the fundamental at 2.3 MHz, but no harmonics. The other tone-burst, shown in Figure 2.3(c) has an amplitude of 400 V_{pp}, and from its spectrum in Figure 2.3(d) we can see a very weak third harmonic (the only harmonic that can be distinguished). It has a small amplitude (39 dB lower than the fundamental) at 7 MHz, which will not cause any significant error in the measurements. Note that neither 2nd nor 4th harmonics are pronounced.

The tone-burst duration was chosen as a result of a tradeoff between the temporal (axial) resolution and the resolution in the frequency domain. The tone-burst must be short enough to ensure good temporal resolution, i.e., ability to resolve objects in the transducer's axial direction in the time domain. On the other hand longer tone-burst improves frequency resolution that is required for distinguishing harmonics in signal spectrum. The tone-burst that we finally chose for harmonic imaging consisted of 8 cycles of 2.3 MHz sine with an amplitude of 400 V_{pp}p.

The conclusion drawn from the tone-burst investigation was that the chosen tone-burst contains mainly a dominant fundamental bandwidth but no significant harmonics, and thus, does not introduce any significant errors in the measurements.

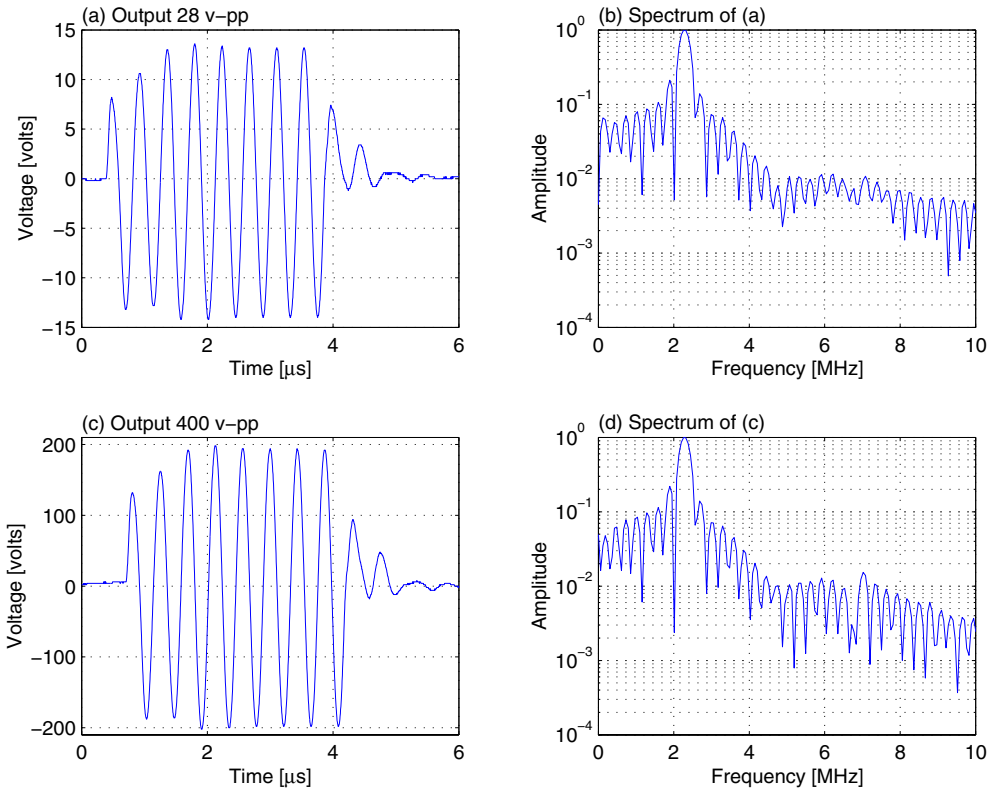

Figure 2.3: Outputs (8-cycle tone-bursts with a 2.3 MHz frequency) from the RITEC RAM-5000 ultrasonic system. (a) 28 V_{pp} and (b) its spectrum, and (c) 400 V_{pp} and (d) its spectrum ('pp' stands for 'peak-to-peak'). Note that in the semi-logarithmic plots the values at the vertical axis, 10^0, 10^{-1}, 10^{-2} and 10^{-k}, correspond to 0, -20, -40, -20k dB, respectively.

Bandpass filters of the RITEC RAM-5000 ultrasonic system

Inherent nonlinearities in the receiver or/and the bandpass (BP) filter may be another source introducing undesired harmonics. The BP filter was formed by combining a HP and a LP filter. 9 available combinations of the HP and LP filters were examined to evaluate the amount of distortion they introduced.

A HP 3314A function generator was used as a source of input signals for the BP filters. The tone-burst generated by the HP 3314A is shown together with its spectrum in Figure 2.4. The tone-burst consisted of 8-cycles a 2.3-MHz sine-wave with amplitude of 15 mV_{pp}. Analysis of its spectrum reveals no harmonics and confirms that the tone-burst is a pure gated sinusoid with the fundamental frequency band.

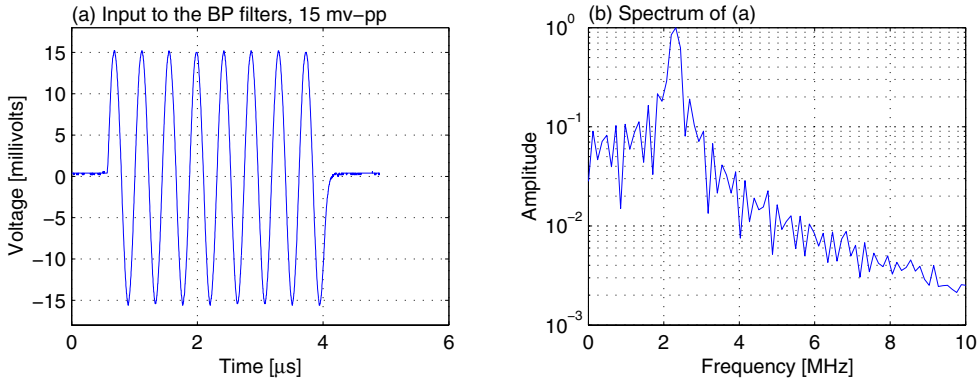

Figure 2.4: Input to the BP filters: a tone-burst from the HP 3314A function generator. (a) The waveform of the tone-burst and (b) its spectrum.

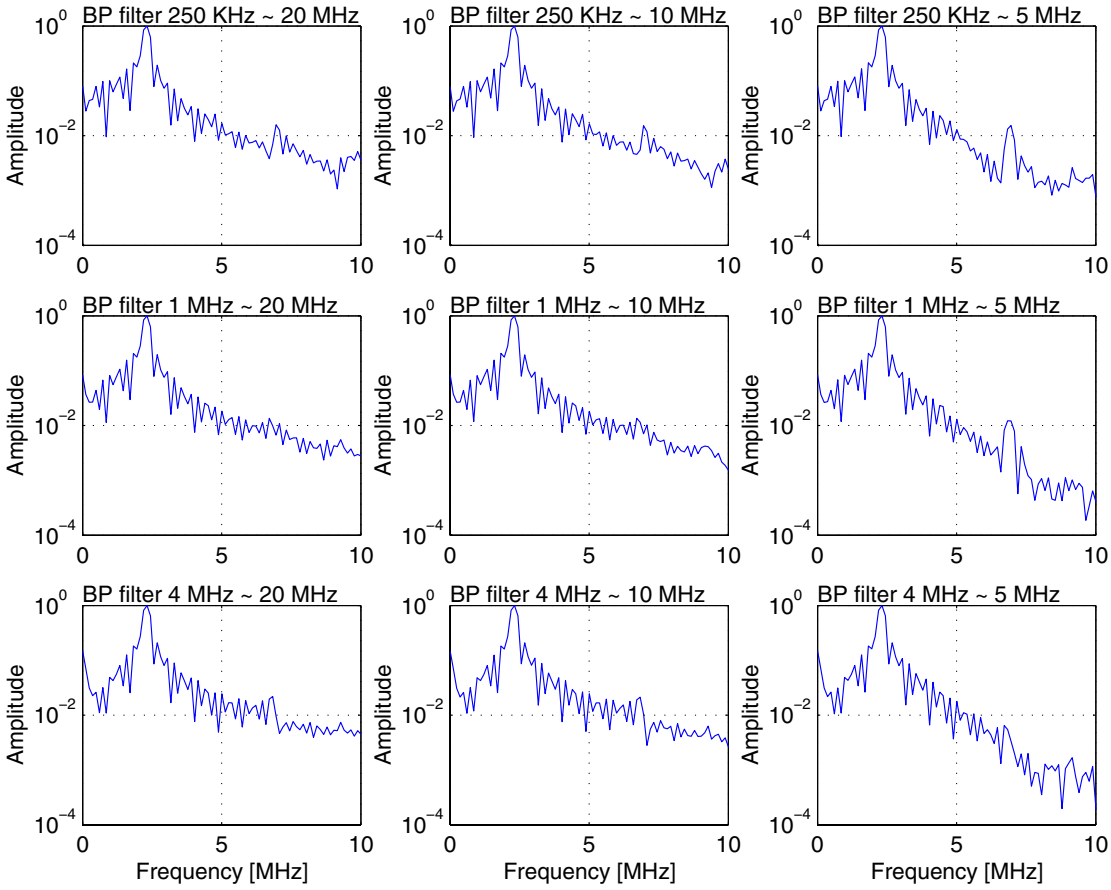

Figure 2.5: Frequency characteristics of 9 BP filters with bandwidths of 0.25-20 MHz, 0.25-10 MHz and 0.25-5 MHz (upper row from left to right); 1-20 MHz, 1-10 MHz and 1-5 MHz (middle row from left to right); 4-20 MHz, 4-10 MHz and 4-5 MHz (lower row from left to right).

Outputs of the 9 BP filters obtained for the tone-burst shown in Figure 2.4 and their spectra are shown in Figure 2.5. Generally, neither 2nd nor 4th harmonics appear in the 9 spectra presented in Figure 2.5. However, weak 3rd harmonic (at 7 MHz) with different amplitudes (39 dB below the fundamental) can be seen in some of the spectra, e.g., those of the BP filters with bandwidths of 250kHz-5MHz and 1MHz-5MHz, etc. Comparing the 9 spectra, it is not difficult to find that the BP filters with the bandwidths of 1-20 MHz and 1-10 MHz have the smallest 3rd harmonics. Therefore, we have chosen the BP filter with a bandwidth of 1-20 MHz for our experiments.

Based on the results of the evaluation of the RITEC system we have chosen the tone-burst consisting of 8-cycles of a gated sine-wave with frequency 2.3 MHz, and the BP filter with a bandwidth of 1-20 MHz. The tone-burst shows a very small amount of harmonics, and the BP filter produces only a very weak 3rd harmonic, which does not introduce a significant error in the measurements.

2.2.3 Examination of nonlinear acoustic fields in water using a hydrophone

The nonlinear acoustic fields radiated by the 2.26-MHz transducer (the outer element of the annular array) were measured using the system consisting of a hydrophone (with bandwidth of 0.2-30 MHz), a broadband preamplifier, a digital oscilloscope and a computer. This setup eliminates the effect of narrow-bandwidth filtering (attenuating higher harmonics) introduced

by the receiving transducer in the measurements of nonlinear fields.

Positioning of the hydrophone was important to the measurements of acoustic fields of the transducer. With help of the ALLIN ultrasonic system this could be easily performed. The hydrophone in this case was connected to the reception port in the ALLIN system (instead connected to the broadband preamplifier) and the transducer being measured was scanned by the ALLIN mechanical scanning system. Using the C-scan function in the ALLIN system we performed an across-axis measurement of the acoustic field from the transducer. An across-axis measurement of the acoustic field in the plane at distance z=31 mm is shown in Figure 2.6. Based on such a measurement we could move the transducer precisely to any desired measurement positions, e.g., on and off the transducer axis.

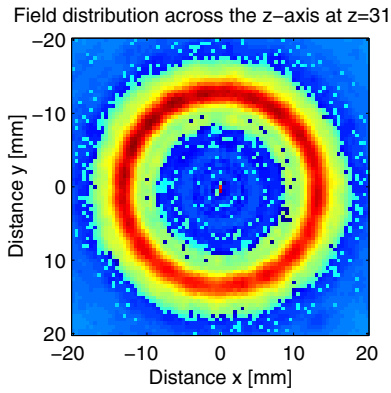

Figure 2.6: Across-axis measurement of the acoustic field using the hydrophone (at z=31 mm).

Nonlinear acoustic fields from the 2.26-MHz transmitter were measured at two different distances from the transmitter plane to the hydrophone plane, i.e., at z=31 and 200 mm, respectively. The 31 mm is the distance at which the inspected copper specimens should be positioned to focus ultrasound at approx. 60 mm below surface in copper. The 200 mm is the distance close to the transducer focus in water, F=210 mm. Measurements at both distances were performed using the transducer tone-burst excitations with amplitudes of 50 and 400 V_{pp}.

The tone-burst pulses measured on the transducer axis at z=31 mm and the corresponding spectra are shown in Figure 2.7. From the spectra in Figure 2.7(b) and (d), we can see that the measured pulse for the 400 V_{pp} excitation shows small 2nd and 3rd harmonics. This indicates that the on-axis nonlinear effect at z=31 mm is small for the 400 V_{pp} tone-burst excitation. However, the nonlinearity off the axis become significantly large, which can be seen from the off-axis measurement at x=14 mm, z=31 mm in Figure 2.8 in which the second and third harmonics are clearly seen and larger than those in the on-axis measurement. These second and higher harmonics at the water/copper interface will also travel into the immersed copper so that the nonlinear signals from inside the copper material contain higher harmonics from two contributions: one from water and the other from the copper material. The ratio of these two contributions will be investigated in the future work.

Looking at the tone-bursts measured at 200 mm and the corresponding spectra in Figure 2.9, we can clearly see the harmonics up to the fourth order in the frequency range of 0-10 MHz even for small 50-V_{pp} tone-burst excitation. For the 400-V_{pp} tone-burst excitation, we can see the harmonics up to 20th order in the frequency range of 0-50 MHz. This demonstrates a very strong nonlinearity appearing in the focal zone, which is because of two reasons: (1) the acoustic energy in the focus zone is much larger than that at 31 mm, and (2) more nonlinear distortion accumulates at a longer propagation distance.

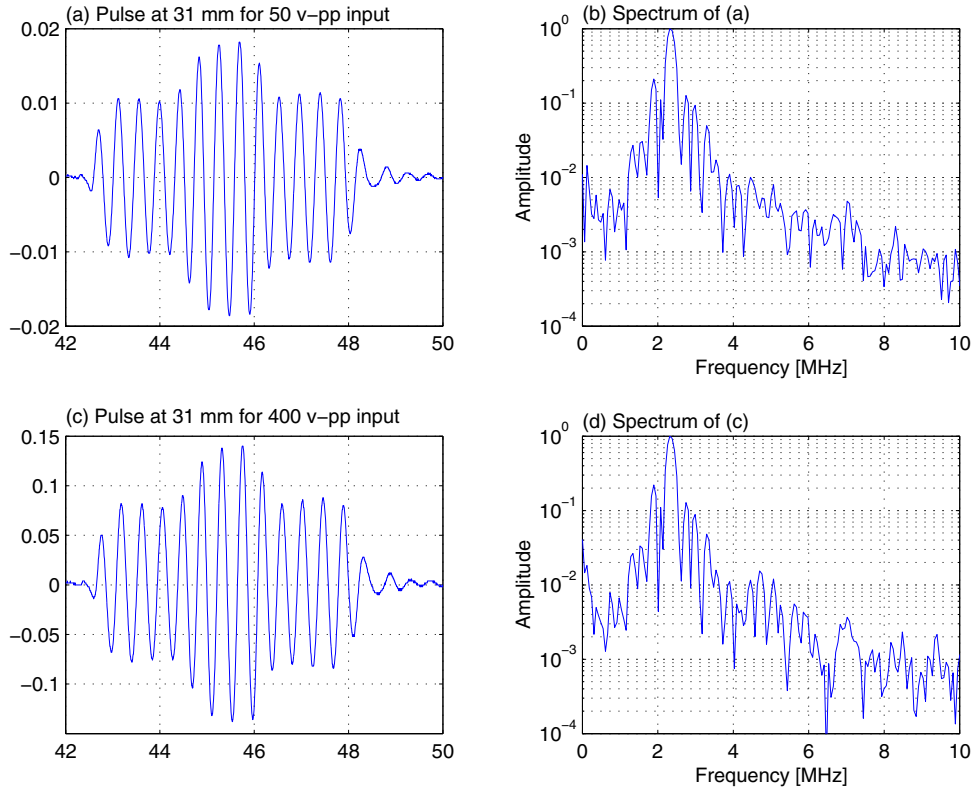

Figure 2.7: Measurements of nonlinear acoustic fields on the axis using the hydrophone at x=0 mm, z=31 mm. (a) The measured waveform for the 50 V_{pp} input and (b) its spectrum, and (c) the measured waveform for the 400 V_{pp} input and (d) its spectrum.

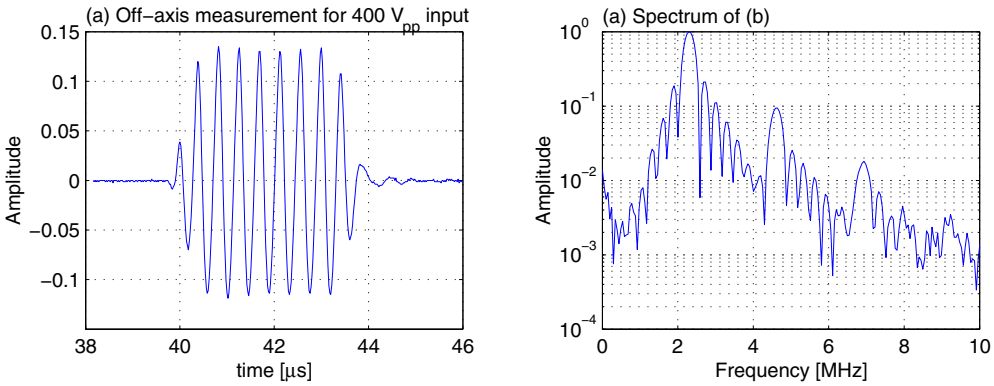

Figure 2.8: Measurements of nonlinear acoustic fields off the axis using the hydrophone at x=14 mm, z=31 mm. (a) the measured waveform for the 400 V_{pp} input and (b) its spectrum.

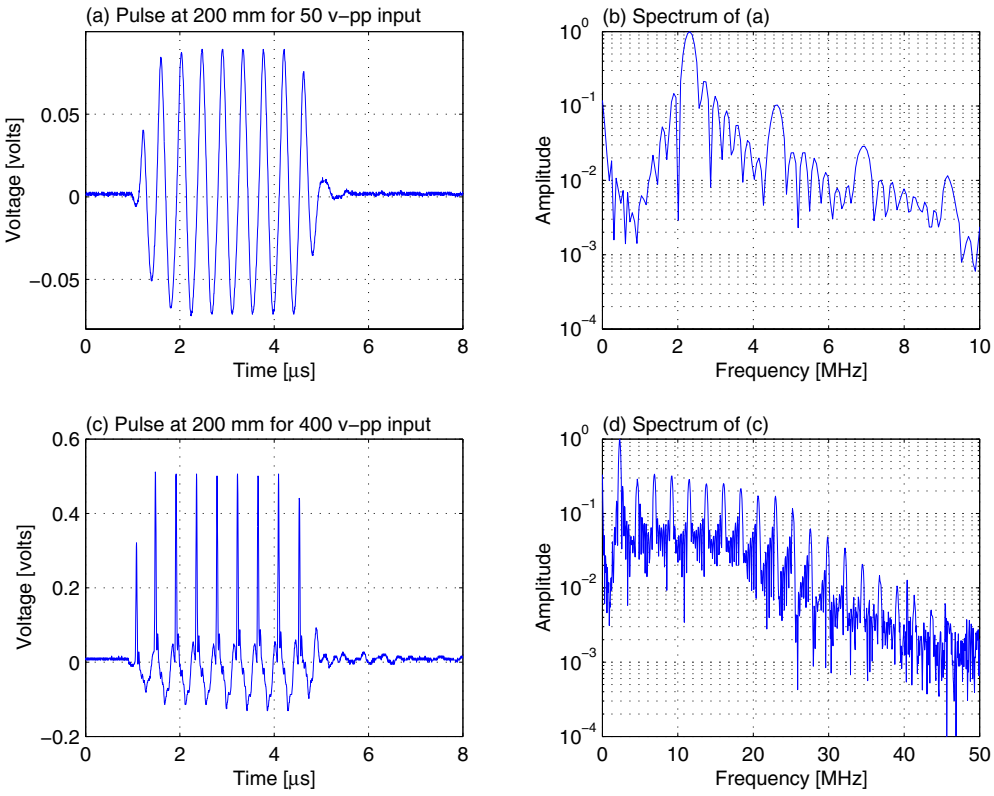

Figure 2.9: Measurements of nonlinear fields using the hydrophone at z=200 mm. (a) Waveform measured for the 50 V_{pp} excitation and (b) its spectrum, and (c) Waveform measured for the 400 V_{pp} excitation and (d) its spectrum.

Variation of the nonlinearity was observed as a function of excitation voltage. The output voltage was changed in 50 steps, corresponding to the voltage range of 28 to 400 V_{pp}. 400 V_{pp} was the maximum voltage used in the measurements because this value was still safe for the transducer and at the same time it was high enough to produce harmonics in the immersed copper blocks.

The nonlinearity as a function of excitation voltage measured at z=200 mm is shown in Figure 2.10. The figure only shows the 2nd, 3rd and 4th harmonics normalized by the fundamental component at the corresponding values of the excitation voltage. From the figure we can see that the harmonics increase with the excitation voltage, which coincides with the nonlinear acoustic theory. In the figure, we can see a 'hump' around the voltage range of 230 to 330 with a jump at 230 V. This is due to the measurement error that has not been explained yet.

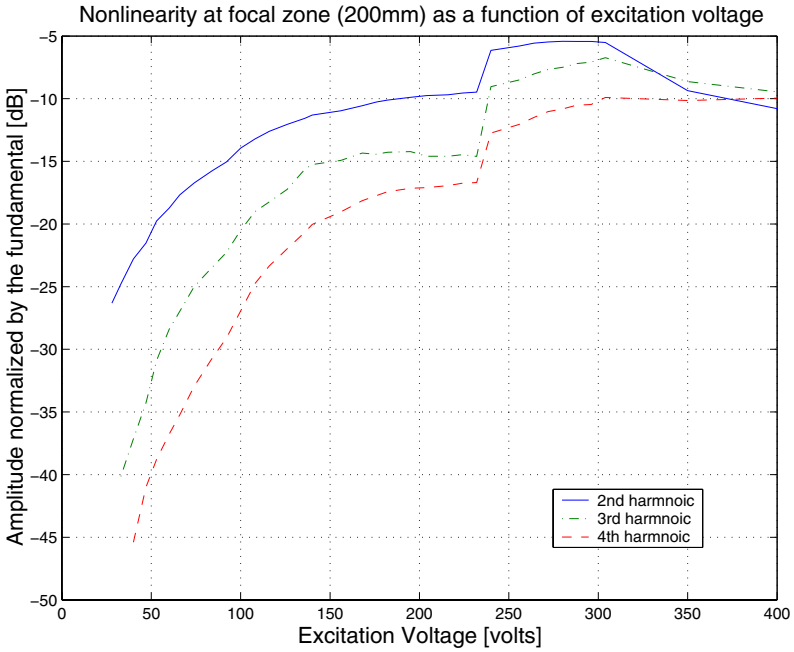

Figure 2.10: Nonlinearity as a function of input voltage.

2.3 Material harmonic imaging of copper material and EB welds

Material harmonic imaging (MHI) has been realized using both the nonlinear longitudinal waves (LW) and the nonlinear shear waves (SW). The MHI has been conducted using the specimen Cu2 (pure copper block) and the specimen CAN1 (section of a copper canister) using the experimental setup shown in Figure 2.1. Pulse-echo mode was used in this case, the 4.83-MHz transducer was used as a receiver while the 2.26-MHz transducer was excited by the 8-cycle tone-burst with a frequency 2.3 MHz and amplitude 400-V_{pp}. It should be noted that since the receiving transducer has a center frequency of 4.83 MHz, that is, close to the second harmonic of the fundamental frequency of 2.3 MHz it amplifiers the second harmonic comparing to the fundamental and the other higher harmonics. The annular array was moved by the mechanic scanning robot in the ALLIN system and the inspection was performed in immersion (water path between the transducer and the materials was 31 mm).

2.3.1 Harmonic imaging of the copper specimen Cu2

Geometry of copper specimen Cu2 is shown in Figure 2.11. The specimen Cu2 contains 18 side-drilled holes (SDH) with diameter 1-mm located at depths of 4, 8, ..., 68, 72 mm, respectively.

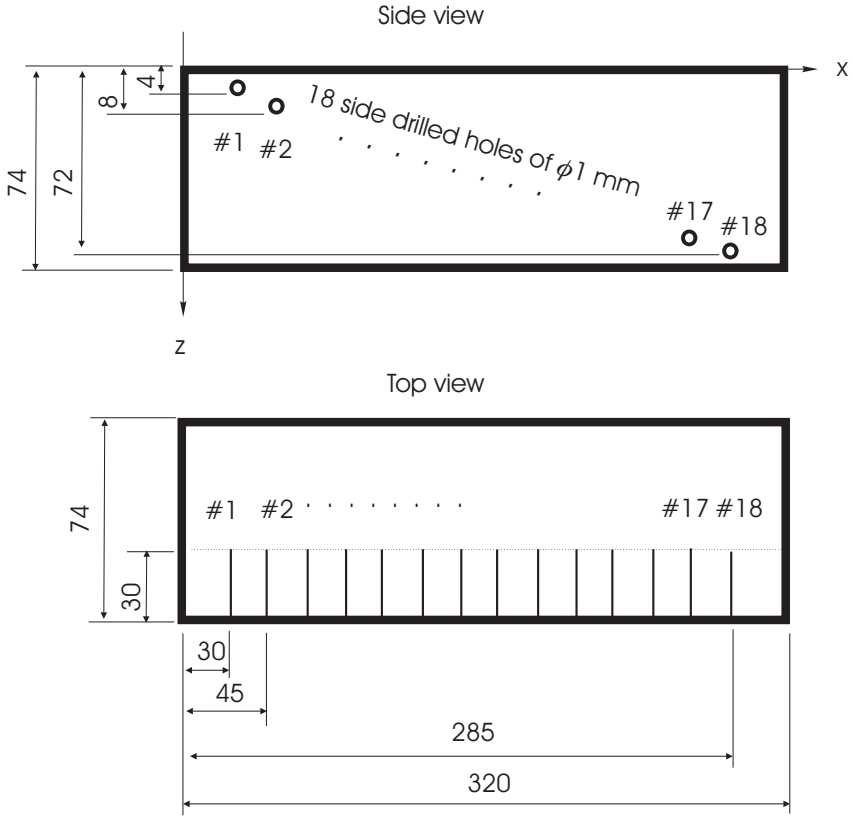

Figure 2.11: Geometry of copper block Cu2.

The ALLIN system was used to scan the annular array along the specimen to obtain a B-scan with all SDHs. The received signal was amplified and BP filtered by the RITEC system and recorded by the Allin system. Ultrasonic image of the specimen Cu2 obtained in this setup is shown in Figure 2.12(a). Material harmonic images of the specimen Cu2 were extracted using Hanning windows in the frequency domain (with center frequencies matching the respective harmonics) for extracting the fundamental and the higher harmonics from the raw data. The images extracted from the fundamental and the 2nd order harmonics are shown in Figure 2.12(b) and (c). The RF signal (echo) from SDH# 11 is shown in Figure 2.12(d). In its spectrum (Figure 2.12(d)) we can clearly see the harmonics up to the third order. Comparing the images reconstructed from the fundamental (Figure 2.12(b)) and the 2nd harmonic (Figure 2.12(c)), we can see that the 2nd harmonic image shows a superior lateral resolution. We can also see that in the 2nd harmonic image the intensity of the echoes from the individual holes increases with the propagation depth in copper. This can be explained by the fact that the nonlinear distortion of the elastic waves increases with the propagation distance.

The nonlinear effect measured as a function of the excitation voltage is plotted in Figure 2.13. The plots are based on the measurements of the echo from Hole #11 that is located at a depth of 44 mm in Cu2. The figure shows the 2nd, 3rd and 4th harmonics normalized by the fundamental component measured at the respective values of the excitation voltage. From the figure it can be seen that the second harmonic manifests a clear monotonic increase with the excitation voltage, while the 2nd and the 3rd harmonics fail to do that. Low signal-to-noise ratio for the 2nd and

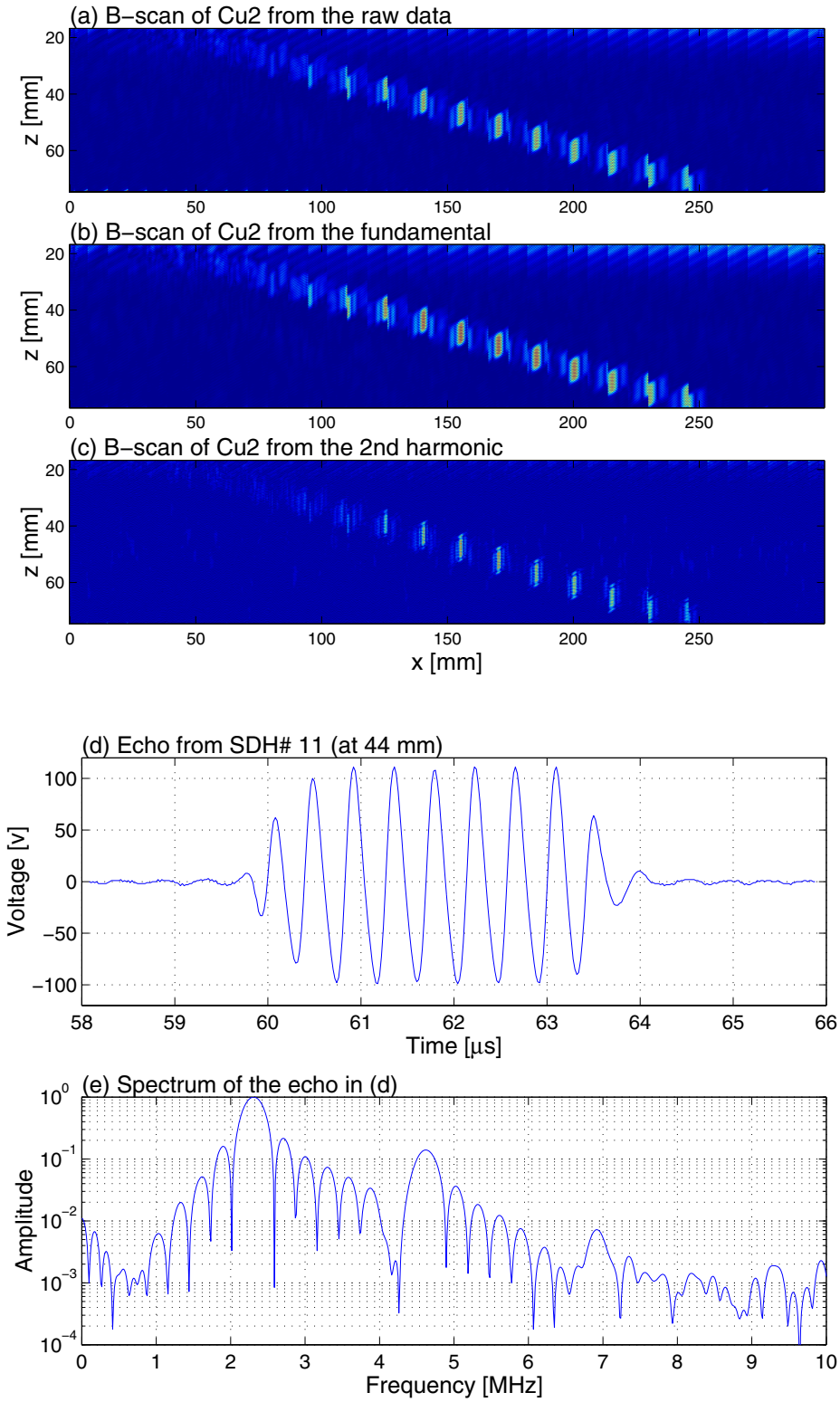

Figure 2.12: Harmonic imaging of immersed copper block Cu2.

the 3rd harmonics, which lowers confidence to the results may be blamed for that.

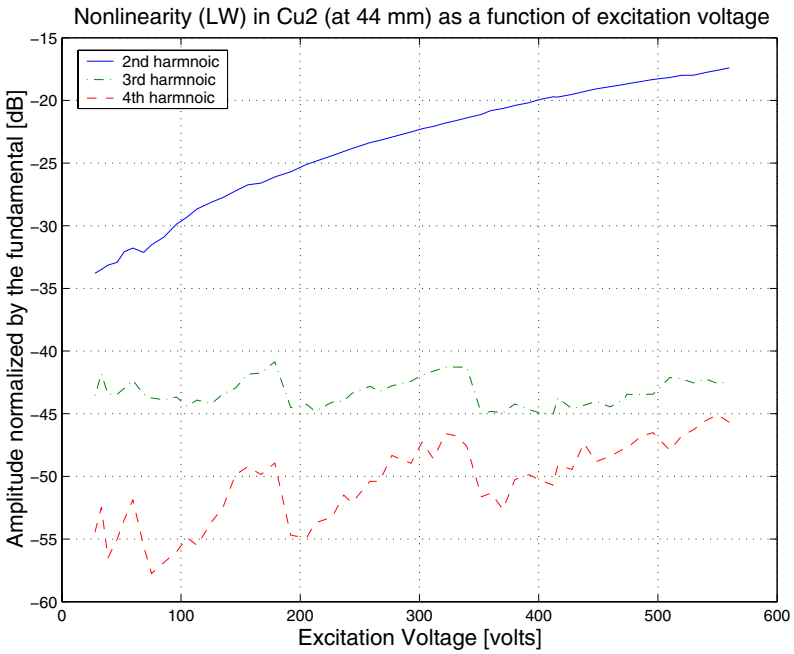

Figure 2.13: Normalized amplitudes of higher harmonics as a function of exciting voltage.

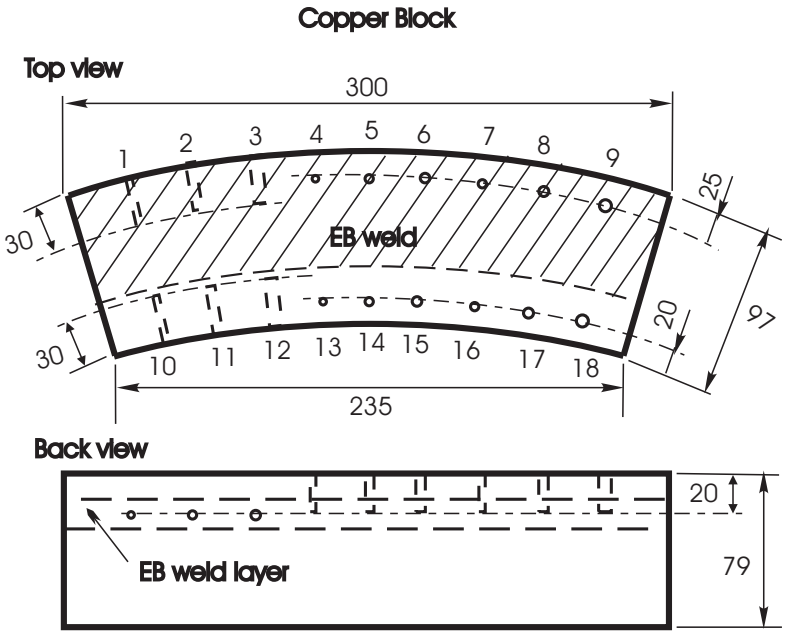

Hole No.	1	2	3	4	5	6	7	8	9
	10	11	12	13	14	15	16	17	18
Type	SDH			FBH			RBH		
Diameter	1.0	1.5	2.0	1.5	2.0	2.5	2.0	2.5	3.0

Figure 2.14: Geometry of the specimen CAN1 (section of copper canister).

2.3.2 Harmonic imaging of the specimen CAN1

Harmonic imaging of the specimen CAN1 (section of a copper canister) shown in Figure 2.14 has been performed using three different types of beams: a normally incident LW beam, an angled LW beam, and an angled SW beam.

Harmonic imaging using a normal LW beam

Harmonic images of CAN1 were created in the same way as those described in the previous subsection. C-scans of CAN1 extracted respectively from the raw data, the 2nd and the 3rd harmonic are shown in Figure 2.15. Comparison of the respective C-scans leads to the conclusion that the higher harmonic imaging has a better lateral resolution.

We also selected two RF echo signals from the raw data, one from the FBH #14 located outside the EB weld zone, and the other from the FBH #5 in the EB weld zone. Those two signals together with their spectra are shown in Figure 2.16. From Figures 2.15 and 2.16 we can see that the harmonics up to the third order in the nonlinear elastic waves can be distinguished in the signals' spectra.

Harmonic imaging using an angled LW beam

In addition to the normal incident LW beam, we also investigated using an angled LW beam for imaging the specimen CAN1. The LW beam at an angle of 40^o was created in copper due to refraction of a 12^o incident beam radiated by the tilted annular array. The ultrasonic images of CAN1 obtained from the fundamental and higher harmonics using the angled longitudinal

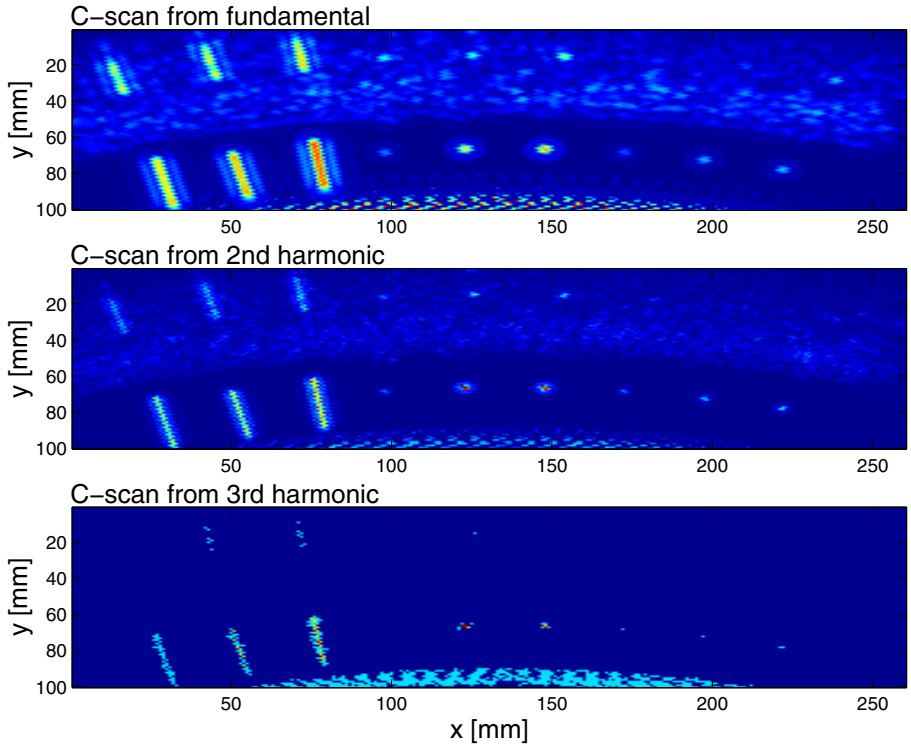

Figure 2.15: Ultrasonic imaging of copper canister CAN1 using normal incident LW beam. The C-scans of EB weld in CAN1 extracted from raw data (a), the fundamental (b), and the 2nd harmonic (c).

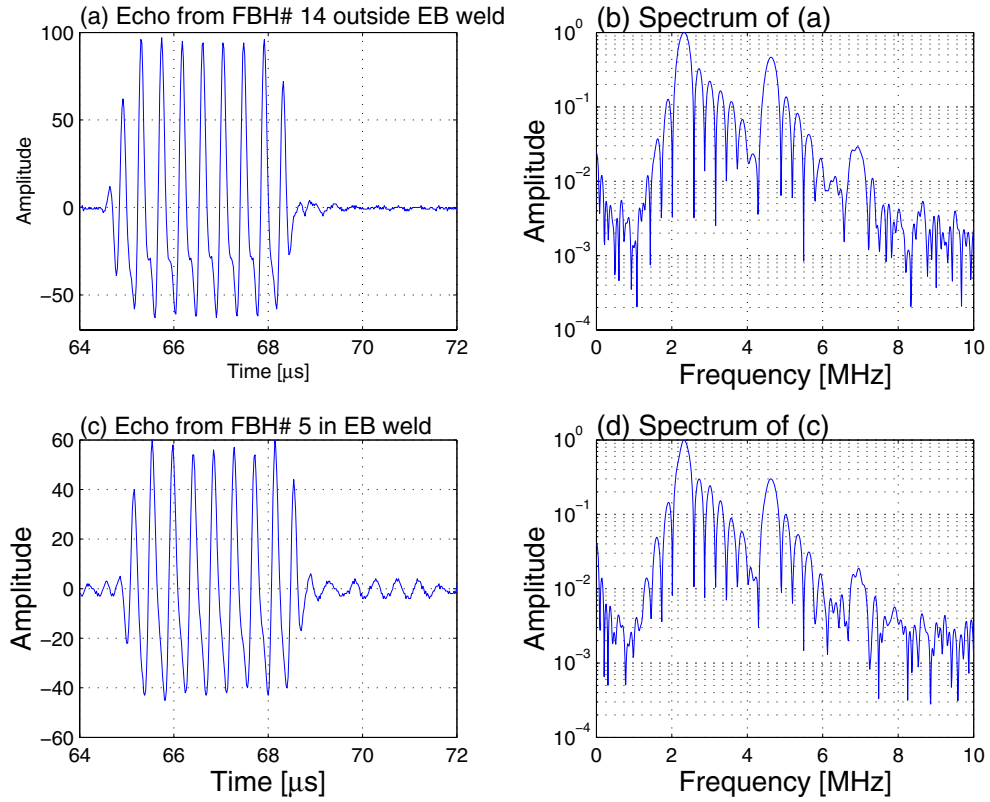

Figure 2.16: Echoes from SDH #14 and SDH #5 (normal incident LW beam).

elastic wave are shown Figure 2.17. Only the SDHs in and outside the EB weld are seen in the C-scans since due to the geometrical conditions bottom drilled holes cannot be seen in the C-scans obtained from the angled beams. C-scans extracted from the raw data and the fundamental do not show much difference. The image extracted from the second harmonic, however, has an improved lateral resolution. In the C-scan from the third-order harmonic only the side-drilled holes located outside the EB weld can be seen. This demonstrates that the third harmonic for the angled LW beam is largely attenuated by the weld.

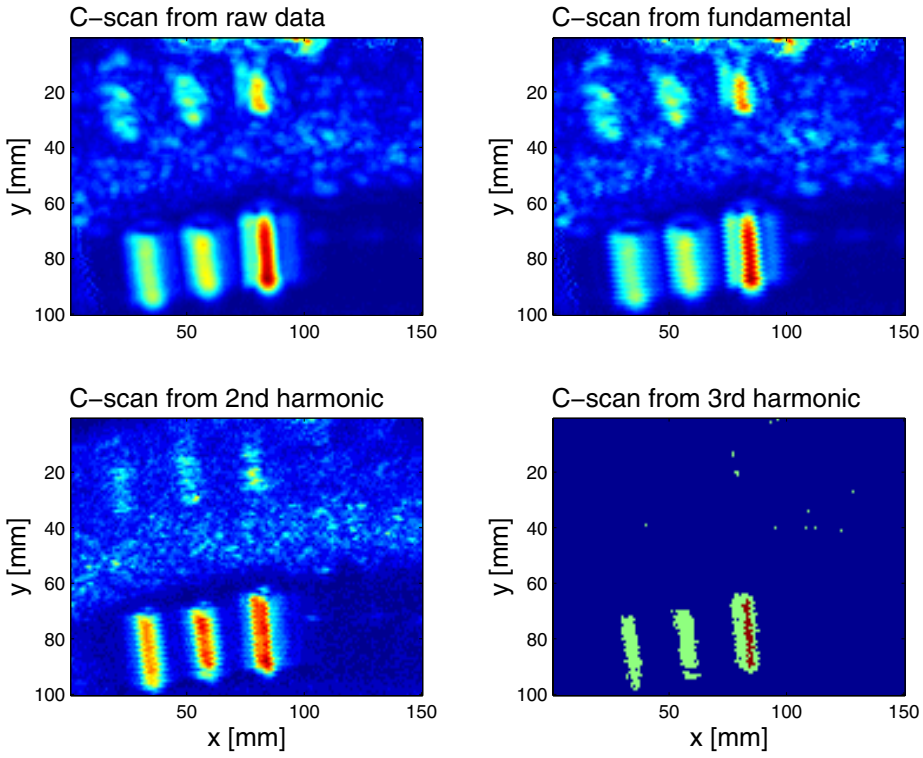

Figure 2.17: Ultrasonic imaging using angled 40^o LW beam. C-scans obtained using respectively, raw data, the fundamental, the 2nd, and 3rd harmonic are shown in the individual panels.

Harmonic imaging using an angled SW beam

In a solid material both LW and SW may exist. The fact that both types of waves have different features motivated us to use the SW for harmonic imaging.

In the immersion case, the SW beam in solid can be generated by refraction using an obliquely incident beam in water. To obtain a pure SW beam, we used an oblique beam with an incident angle of 25^o, which is larger than the critical angle for LW (18.78^o) and less than the critical angle for SW (41.58^o). In this condition the refracted beam in copper had an angle of 40^o.

The ultrasonic images (C-scans) of CAN1 from the raw data, the fundamental and the 2nd harmonic, respectively, obtained using the 40^o SW beam are shown Figure 2.18. The three side-drilled holes outside the EB weld can be seen only in these C-scans. This is due to a very large attenuation of SW in the EB weld.

In Figure 2.19 we see two examples of the SW echoes (from SDH #12 and SDH #11, respectively) together with their spectra. Harmonics up to the third order can be identified in the spectra of the nonlinear SW.

Summarizing the investigation of the usefulness of three different beam types, i.e., normal LW, angled LW and angled SW beams, for harmonic imaging, we may conclude that only the normal LW beam is a good candidate for the harmonic imaging of EB weld, while the angled LW and SW are not due to a considerable attenuation in the EB weld.

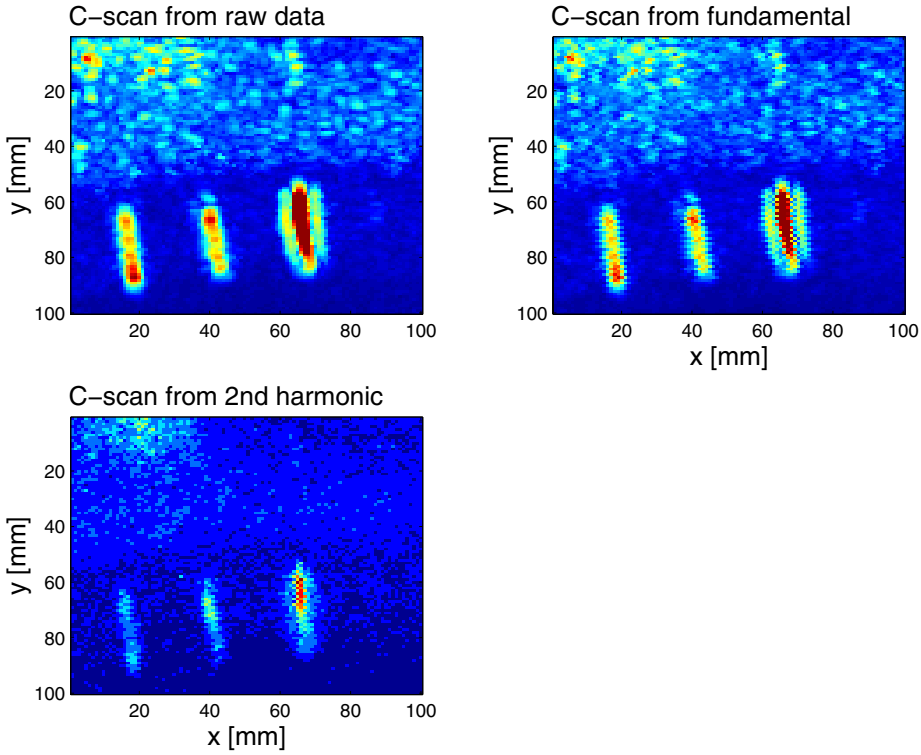

Figure 2.18: Ultrasonic imaging using angled 40^o SW beam. C-scans obtained using respectively, raw data, the fundamental, and the 2nd harmonic are shown in the individual panels.

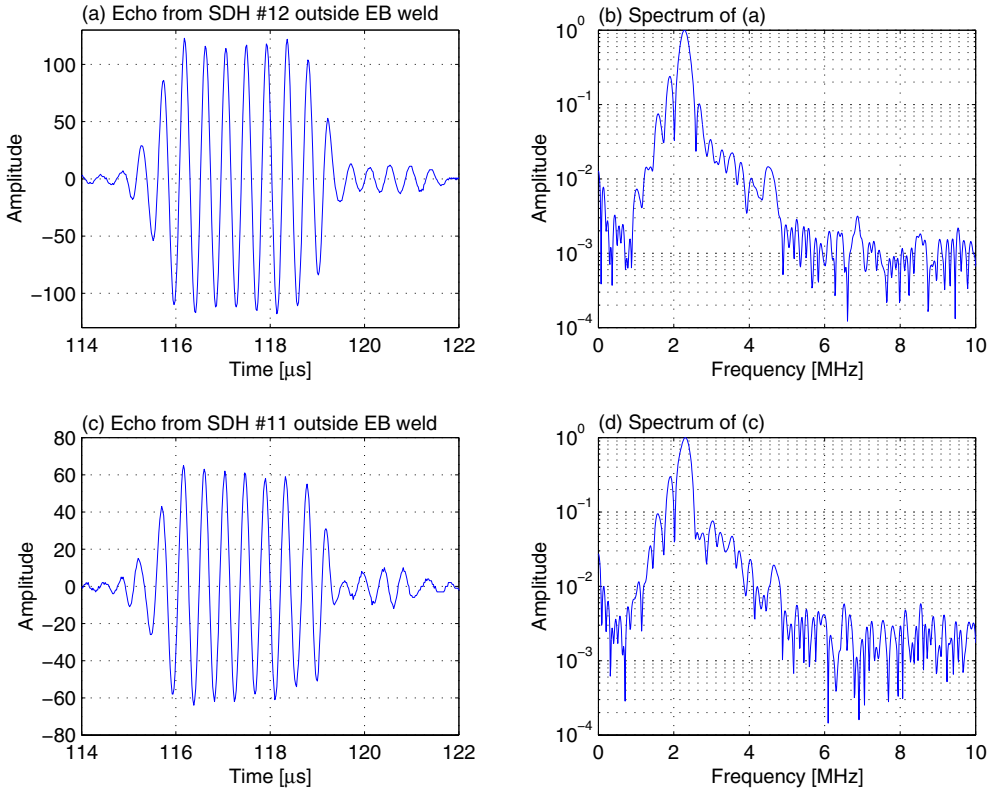

Figure 2.19: Echoes of the SW beam SDH #12 and #11.

2.4 Simulations

Conclusion from the experimental results presented above is limited to two quite obvious general statements:

- a harmonic imaging from higher-order harmonics yields an improved lateral resolution,
- higher harmonics are weak in the near field, and increase with the propagation distance and are strong in the focal zone.

An obvious need of quantitative interpretation of the obtained results motivated the theoretical research presented in this section.

This research was initiated by the simulation of nonlinear propagation of acoustic plane waves in fluids performed previously [3]. A slightly modified version of the method of solving the Burger's equation, proposed by Trivett and Van Buren [34, 35] was used in this simulation. Although the simulations illustrate the way of how a nonlinear *plane* wave develops during its propagation they are insufficient for the interpretation of the recent experimental results that were obtained using ultrasonic beams. The simulations are valid for plane acoustic waves only and do not apply to ultrasonic beams, especially, to the immersion case.

Calculation of nonlinear ultrasonic beams is much more complicated than calculation of linear ultrasonic beams. Only a few methods can be found in the available literature. Those methods may be roughly classified into three categories:

1. The methods based on the solution of the KZK (Kuznetsov-Zabolotskaya-Khokhlov [36, 37]) nonlinear parabolic wave equation [30, 31, 38–40],

2. The methods based on the solution of the nonlinear progressive-wave equation [41], and

3. Frequency-time domain method without the parabolic approximation [42].

All the above-mentioned methods have, up to now, been limited to treating acoustic fields in fluids.

In the present work, we propose a method used for the simulation of the nonlinear fields of ultrasonic beams radiated by a focused annular transducer into water and immersed solids. This method is essentially an operator-splitting approach similar to the method presented by Christopher and Parker [42]. It calculates the nonlinear fields from a transducer by accounting for the diffractive and for the nonlinear effect separately. The method has been extended based on our previous work [1, 3]. The diffractive effect is calculated using the angular spectrum approach (ASA) that was presented in our previous SKB reports [1, 43, 44], and the nonlinear effect is computed using the Burgers equation [34, 35] that was presented in our recent report [3].

The proposed method has been applied to the calculation of both nonlinear acoustic fields in water and nonlinear elastic fields radiated by our 2.26-MHz focused annular transducer in immersed copper. The geometry of the annular array is shown in Figure 2.2 and its parameters are listed above in section 2.2.1.

The following parameters were used in the simulations:

- geometrical parameters of the annular transducer: the inner radius a_1 =10 mm, the outer radius a_2 =19 mm, and the radius of curvature F = 210 mm;
- frequency of the continuous wave excitation to the transducer 2.3 MHz, and the initial source intensity 3W/cm^2, which, we should point out, was not the real initial value on the transducer surface since we could not measure it;
- physical parameters of media: the sound speed in water 1484 m/s, the LW and SW speeds in copper equal to 2260 m/s and 4596 m/s, respectively; the densities of water and copper 1000 kg/m^3 and 8960 kg/m^3, respectively;
- water layer 31 mm;
- nonlinearity parameter β of water and copper 3.6 and 4.54, respectively (the values originate from works published by other researchers [5, 8, 35]).

The nonlinearity parameter β represents the rate of nonlinear distortion of ultrasound, and is thus an important parameter that can be used to characterize nonlinear elastic properties of materials, such as gases, liquids and solids. For solids, the nonlinearity parameter is related to the second and third order elastic constants [7, 8].

The result of simulations of *nonlinear acoustic waves* radiated by the annular focused transducer is shown in Figure 2.20. Figures 2.20(a), (b) and (c) show the fields in the y-z plane of the fundamental, 2nd harmonic and 3rd harmonic, respectively. The on-axis field distributions of the 1st to 4th harmonics are shown in Figure 2.20(d). The cross-axis field distributions of the 1st to 3th harmonics at z=31 mm are shown in Figure 2.20(e) with a linear scale and (f) with a log scale, respectively. The transducer is located on the left hand side at the axial distance z=0 in all plots. The coordinates used in Figure 2.20 are the same as those in Figure 2.2.

From the simulated results (cf Figure 2.20(d)), we can see that higher harmonics on the axis in the transducer near field are small (that is, for axial distance z<35 mm) but they can be significantly large off the axis, e.g., at y=14 mm and z=31 mm (cf Figure 2.20(b), (c), (e) and (f)). This is in agreement with the measurements (Figure 2.8). The 2nd and 3rd harmonic

fields (Figure 2.20(b) and (c)) are more concentrated in the paraxial area of the transducer in comparison with the fundamental field (Figure 2.20(a)) because the side lobes at large angles are so weak that they can not create any nonlinearity, and thus propagate with linear characteristics.

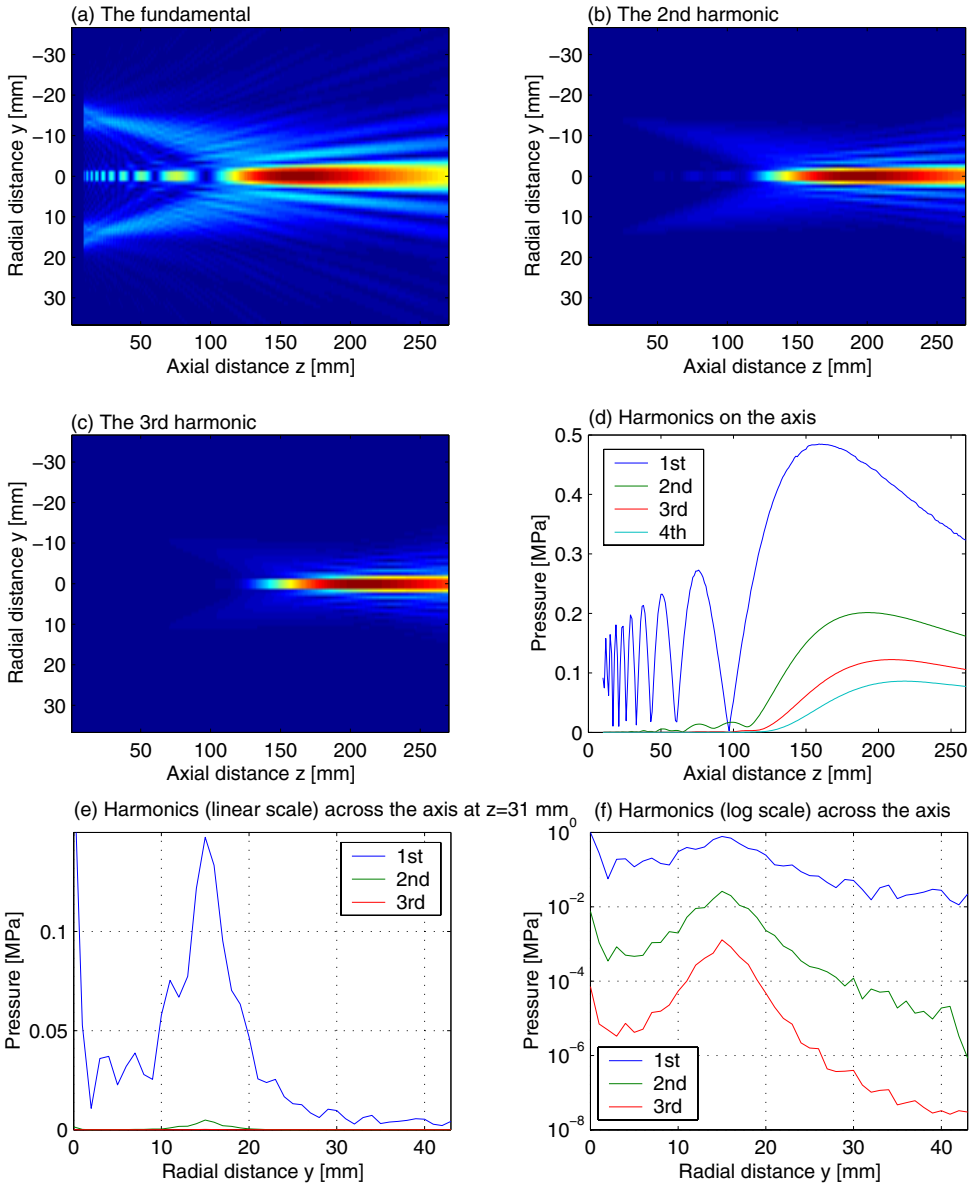

Figure 2.20: Simulations of acoustic waves in water.

In calculating the nonlinear elastic fields in the immersed copper, we used a simplified model by assuming that the elastic waves at the fluid/solid interface excited by the incident acoustic wave only have the fundamental component, and that all observed nonlinear effects are accumulated due to the wave propagation in the immersed copper material. That is, all the higher harmonics at the fluid/solid interface are not taken into account in the calculation at the moment. In the future work, however, we are going to account for all the higher harmonics at the fluid/solid interface in the calculation program and investigate their effect on the whole nonlinearity (the sum of the nonlinearities at the water/copper interface and from inside the immersed copper material).

The result of simulations of *nonlinear elastic waves* from the annular focused transducer is shown in Figure 2.21. The fields in the y-z plane of the fundamental, the 2nd harmonic

and the 3rd harmonic are shown in Figures 2.21(a), (b) and (c), respectively. The on-axis field distributions of the 1st to 4th harmonics are shown in Figure 2.21(d). Note that all the simulations start from z=31 mm where the water/copper interface is located.

Similarly as for *acoustic waves*, the 2nd and 3rd harmonic fields (Figure 2.21(b) and (c)) are more focused in the paraxial area in comparison with those of the fundamental field (Figure 2.20(a)). In comparison with acoustic waves, the beam lobes of the 1st, 2nd and 3rd are broadened.

Comparison of the on-axis distributions of the harmonics in water (Figure 2.20(d)) with those in the immersed copper (Figure 2.21(d)) leads to the conclusion that although the nonlinear parameters of the copper material and water do not differ much (i.e., 3.6 and 4.54, respectively) the nonlinear elastic fields are much smaller than the respective nonlinear acoustic fields. This can be explained by low efficiency of acoustic energy transmission at the water-copper interface – large part of the energy is reflected from the interface. The amount of energy used for the excitation is limited by the transducer safety limit (electrical break down of the piezoelectric material). This observation suggests that we should use contact measurement configuration so as to get much stronger output ultrasound power in the copper material for the same input electric energy to the transducer than the immersion configuration.

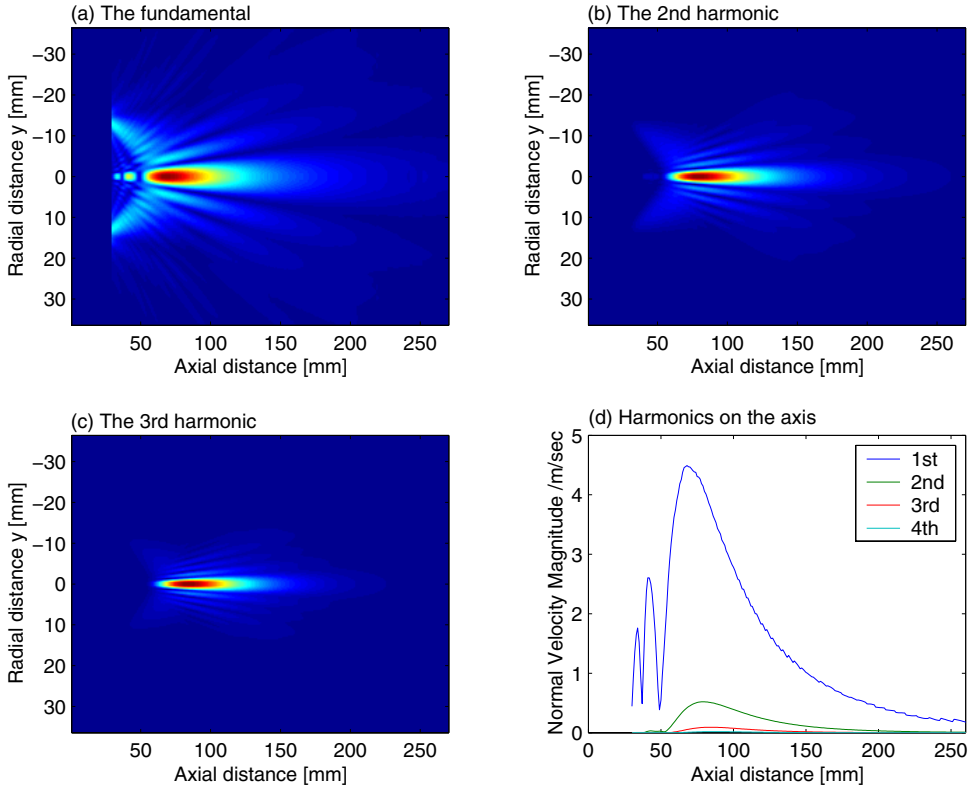

Figure 2.21: Simulations of elastic waves in an immersed copper material.

Material attenuation and ultrasonic frequency used are the two important factors affecting the nonlinear propagation of ultrasound. Generally, ultrasonic attenuation in material increases with frequency. Increasing the resolution by using a high frequency ultrasound is limited by the increasing attenuation of higher harmonics. There exists a balance point on the frequency axis where the attenuation rate and the rate of accumulating higher harmonics are equal. For higher frequencies the attenuation rate becomes larger than the accumulating rate, which results in the decrease of harmonics. Increasing frequency beyond this this point is meaningless since, in

practice it does not improve the resolution.

2.5 Discussions and Conclusions

Extended experimental and theoretical research concerning the potential of nonlinear waves and material harmonic imaging has been reported.

The experimental work has been conducted using the RITEC RAM-5000 ultrasonic system capable of providing a high power tone-burst output for the ultrasonic transmitter to generate intensive ultrasound. Evaluation of the nonlinear distortion that could be introduced by the RITEC system proceeded the experiments. The output of the RITEC gated amplifier as well as its BP filters have been examined as a possible sources inducing unwanted harmonics. The evaluation work resulted in selecting the setting of BP filters that appeared to produce almost no distortion. Also measurements of the near field emitted by the transducer using a hydrophone have shown that the error that may be caused by the measurement system is very small (refer to Figure 2.7).

Measurements of nonlinear acoustic waves in water using a hydrophone were aimed at the evaluation of the nonlinear wave propagation and the harmonics content in water at the water-solid interface. The measurements have shown a strong nonlinearity of the acoustic fields in water increasing with the the increase of the excitation voltage.

Material harmonic imaging was obtained using three different elastic beams, that is, a normal LW beam, a 40^o angled LW beam, and a 40^o angled SW beam. The results revealed that nonlinear elastic LW is a suitable mode for material harmonic imaging while angled SWs are not applicable for the imaging EB welds because of a large attenuation of SW in the weld.

Based on the previous work, a method that is a combination of the angular spectrum approach and the Burger's equation was developed and used for the simulation of nonlinear acoustic waves and nonlinear elastic waves radiated by the annular transducer that was used in the experiments.

Both experiments and simulations have shown that although the nonlinear parameters of copper material and water are not much different the nonlinear distortion observed in copper material is much smaller than that in fluids. This can be explained by a loss of acoustic energy due to the reflection from the water/copper interface so that only a small portion of the acoustic energy emitted by the transducer is transmitted into the copper material. This suggests that we should use contact measurement configuration in order to get much stronger output ultrasound power in the copper material and thus stronger nonlinearity.

Our future work will include investigating contact acoustic nonlinearity (CAN) using a high intensity ultrasound. We plan to apply material harmonic imaging technique to inspect the interfaces, cracks and defects in different materials to find features from the nonlinear waves scattered by cracks and defects suitable for the detection of such anomalies.

Bibliography

[1] P. Wu, F. Lingvall, and T. Stepinski. Inspection of copper canisters for spent nuclear fuel by means of ultrasound - electron beam evaluation, harmonic imaging, materials characterization and ultrasonic modelling. Technical Report TR-00-23, SKB, 2000.

[2] P. Wu and T. Stepinski. Ultrasonic harmonic imaging in nondestructive evaluation: preliminary experimental study. *2000 IEEE Ultrason Symp.*, pages 801–804, 2000.

[3] T. Stepinski, F. Lingvall, and Ping Wu. Inspection of copper canisters for spent nuclear

fuel by means of ultrasound - ultrasonic imaging of eb weld, theory of harmonic imaging of welds, and nde of cast iron. Technical Report TR-01-36, SKB, 2001.

[4] L. D. Landau and E. M. Lifshitz. *Theory of elasticity.* Pergamon Press, San Diego, 1986.

[5] W. B. Gauster and M. A. Breazeale. Ultrasonic measurement of the nonlinear parameters of copper single crystals. *Phys. Rev.*, 168(3):655–661, 1968.

[6] R. D. Peters, M. A. Breazeale, and J. Ford. Third harmonic of an initial sinusoidal ultrasonic wave in copper. *Appl. Phys. Letters*, 12(3):106–109, 1968.

[7] M. A. Breazeale and J. Ford. Ultrasonic studies of the nonlinear properties of solids. *Int J. Nondestr. Test.*, 4:149–166, 1972.

[8] M. A. Breazeale and J. Philip. Determination of third-order elastic constants from ultrasonic harmonic generation measurements. *Phys. Acoust.*, 17:1–60, 1984.

[9] M. A. Breazeale and J. Ford. Ultrasonic studies of the nonlinear behavior of solids. *J. Appl. Phys.*, 36:3486–3490, 1965.

[10] P. B. Nagy. Excess nonlinearity in material containing microcracks. *Rev. Progr. QNDE*, 13:1987–1994, 1994.

[11] P. B. Nagy. Fatigue damage assessment by nonlinear ultrasonic material characterization. *Ultrasonics*, 36:375–381, 1998.

[12] K.-Y. Jhong and K.-C. Kim. Evaluation of material degradation using nonlinear acoustic effect. *Ultrasonics*, 37:39–44, 1999.

[13] K.-Y. Jhong. Application of nonlinear ultrasonics to the nde of material degradation. *IEEE Trans. Ultrason. Ferroelectr.Freq. Contr.*, 47(3):540–548, 2000.

[14] H. Hirose and J. D. Achenbach. Higher harmonics in the far field due to dynamic crack-face contacting. *J. Acoust. Soc. Am.*, 93(1):142–147, 1993.

[15] I. Yu. Solodov. Nonlinear nde using contact acoustic nonlinearity. *1994 IEEE Ultrason Symp.*, pages 1279–1283, 1994.

[16] I. Yu. Solodov. Ultrasonics of non-linear contacts: propagation, reflection and nde-applications. *Ultrasonics*, 36:383–390, 1998.

[17] R. G. Maev and I. Yu. Solodov. Acoustic reflectivity enhancement using higher-order nonlinear reflection mode. *1998 IEEE Ultrason Symp.*, pages 707–710, 1998.

[18] I. Yu. Solodov, N. Krone, and G. Busse. Can: an example of nonlclassical acoustic nonlinearity in solids. *Ultrasonics*, 40:621–625, 2002.

[19] V. Yu. Zaitsev, V. Gusev, and B. Castagnde. Observation of the "luxemburg-gorky effect" for elastic waves. *Ultrasonics*, 40:627–631, 2002.

[20] N. Krohn, R. Stoessel, and G. Busse. Acoustic non-linearity for defect selective imaging. *Ultrasonics*, 40:633–637, 2002.

[21] M. Rothenfusser, M. Mayr, and J. Baumann. Acoustic nonlinearities in adhesive joints. *Ultrasonics*, 38:322–326, 2000.

[22] S. Hirsekorn. Nonlinear transfer of ultrasound by adhesive joints - a theoretical description. *Ultrasonics*, 39:57–68, 2001.

[23] A. Wegner, A. Koka, K. Janser, U. Netzelman, S. Hirsekorn, and A. Arnold. Assessment of the adhesion quality of fusion-welded silicon wafers with nonlinear ultrasound. *Ultrasonics*, 38:316–321, 2000.

[24] A. N. Noriss. *Nonlinear Acoustics*, chapter 9, pages 263–277. Academic Press, San Diego, 1998. edited by M. F. Hamilton and D. T. Blackstock.

[25] M. A. Breazeale. Anharmonicity, piezoelectricity, and solid state nonlinearity. *Rev. Progr. QNDE*, 10:1797–1803, 1991.

[26] J. H. Cantrell and W. T. Yost. Acoustic harmonic generation from fatigure-induced dislocation dipoles. *Phil. Mag.*, 69(2):315–326, 1994.

[27] J. H. Cantrell and W. T. Yost. Effect of precipitate conherency strains on acoustic harmonic generation. *J. Appl. Phys.*, 81(7):2957–2962, 1997.

[28] R. A. Guyer and P. A. Johnson. Nonlinear mesoscopic elasticity: evidence for a new class of materials. *Phys. Today*, 30(4):30–36, 4 1999.

[29] A. C. Baker, K. Anastasiadis, and V. F. Humphrey. The nonlinear pressure field of a plane circular piston: Theory and experiment. *J. Acoust. Soc. Am.*, 84:1483–1487, 1988.

[30] A. C. Baker and V. F. Humphrey. Distortion and high frequency generation due to nonlinear propagation of short ultrasonic pulses from a plane circular piston. *J. Acoust. Soc. Am.*, 92:1699–1705, 1992.

[31] A. C. Baker, A. M. Berg, A. Sahin, and J. Naze Tjϕtta. The nonlinear pressure field of plane, rectangular apertures: Experiment and theoretical results. *J. Acoust. Soc. Am.*, 97:3510–3517, 1995.

[32] M. A. Averkiou and M. F. Hamilton. Measurements of harmnic generation in a focused finite-amplitude sound beams. *J. Acoust. Soc. Am.*, 98:3439–3442, 1995.

[33] M. A. Averkiou and M. F. Hamilton. Nonlinear distortion of short pulses radiated by plane and focused circular pistons. *J. Acoust. Soc. Am.*, 102, 1997.

[34] D. H. Trivett and A. L. Van Buren. Propagation of plane, cylindrical, and spherical finite amplitude waves. *J. Acoust. Soc. Am.*, 69(4):943–949, 1981.

[35] M. F. Hamilton and D. T. Blackstock. *Nonlinear Acoustics*. Academic Press, San Diego, 1998.

[36] V. P. Kuznetsov. Equations of nonlinear acoustics. *Sov. Phys. Acoust.*, 16:467–470, 1971.

[37] E. A. Zabolotskaya and R. V. Khokhlov. Equations of nonlinear acoustics. *Sov. Phys. Acoust.*, 15:35–40, 1969.

[38] S. I. Aanosen, T. Barkve, J. Naze Tjϕtta, and S. Tjϕtta. Distortion and harmonic generation in the nearfield of a finite-amplitude sound beam. *J. Acoust. Soc. Am.*, 75:749–768, 1984.

[39] N. S. Bakhvalov, Ya. M. Zlileinkin, and E. A. Zabolotskaya. *Nonlinear theory of sound beams*. American Institute of Physics, New York, 1987.

[40] Y.-S. Lee and M. F. Hamilton. Time-domain modeling of pulsed finite-amplitude sound beams. *J. Acoust. Soc. Am.*, 97:906–917, 1995.

[41] B. E. McDonald and W. A. Kuperman. The time domain formulation for pulse propagtion including nonlinear behavior at caustic. *J. Acoust. Soc. Am.*, 81:1406–1417, 1987.

[42] P. T. Christopher and K. J. Parker. New approaches to nonlinear diffractive field propagation. *J. Acoust. Soc. Am.*, 90(1):488–499, 1991.

[43] P. Wu and T. Stepinski. Inspection of copper canisters for spent nuclear fuel by means of ultrasonic array system - modelling, defect detection and grain noise estimation. Technical Report TR-99-12, SKB, 1998.

[44] P. Wu, F. Lingvall, and T. Stepinski. Inspection of copper canisters for spent nuclear fuel by means of ultrasonic array system - electron beam evaluation, modelling, and materials characterization. Technical Report TR-99-43, SKB, 1999.

Chapter 3

Synthetic Aperture Imaging

3.1 Introduction

All transducers used for imaging due to their finite aperture introduce distortion in a B-scan image which results in a limited lateral resolution. A considerable work that has been done to improve the image quality can be categorized in two slightly different approaches: ultrasonic image restoration and synthetic aperture imaging (SAI).

The first approach consists in considering an ultrasonic B-scan as an image distorted by the transducer's point spread function (PSF). If the image distortion can be modeled as a convolution then the deconvolution of the transducer's PSF should result in image restoration. Many authors proposed using the Wiener filter for this purpose [1–3]. The Wiener filter requires *a priori* knowledge of the transducer PSF that either has to be calculated or estimated. A number of suboptimal solutions were presented, for instance, Vollman [2] proposed using a Gaussian PSF for the deconvolution.

The second approach, the synthetic aperture focusing technique (SAFT), is based on a concept borrowed from radar imaging techniques. The solution in both application fields is to move a small transducer along a line and process the collected data to simulate a desired large aperture. This technique, in its classical time domain realization, is based on ray acoustics, that is, the waves are assumed spherical. It consists in delaying each echo signal along the synthetic aperture and coherently summing them to form the image at the focal point [4]. SAFT can also be implemented in the frequency domain using the Fourier transform [5]. Mayer at al. [6] have shown that the Fourier transform SAFT is a special solution of the inverse scattering problem. Furthermore, SAFT being a spatial compounding technique, has several practical advantages. For instance, it can reduce speckle noise and improve the signal-to-noise ratio (SNR). In practical implementations of SAFT imaging there is a trade-off between the size of the transducer and the requirement concerning SNR in the received signal. Using larger transducers improves the SNR but at the same time introduces a mismatch between the true wave front from the transducer element and the spherical wave front required by SAFT and results in the reduced the quality of the reconstructed images.

In this chapter we present a comparison of traditional phased array B-scan imaging, SAFT imaging and a new method presented recently in [7, 8]. The presented method takes the form of a 2D filter based on minimum mean squared error (MMSE) criteria. The new method is shortly presented and its resolution is to compared experimentally to that of classical SAFT and phased array (PA) imaging using a copper specimen.

In Section 3.2 a short introduction to phased array imaging is given and in Section 3.3 the SAFT method is introduced. The latter section also treats some of the properties of the SAFT method. In Section 3.4 the concept of spatial impulse responses is introduced and its importance for ultrasonic imaging is discussed. Section 3.5 then discusses the new MMSE method for SAI where spatial impulse responses plays a significant role. The experimental results of the three methods are presented in Section 3.6. Finally Section 3.7 contains a discussion.

3.2 Phased Array Imaging

Phased array (PA) imaging is not a synthetic aperture imaging (SAI) technique as the name of this chapter indicates. The PA method is included here as a benchmark to the two SAI methods presented later in this chapter. The properties of the PA method have been thoroughly discussed in the previous reports [9]. Here we will only give a short summary if its principles.

To achieve focusing the acoustic waves generated by each element of the array should arrive at the point of interest at the same time instant. In a PA this is accomplished by delaying both the transmitted and received signals to (from) the active elements. This focusing method is

based on ray-acoustics, which means that it neither takes the electrical impulse response into consideration nor the size of its elements (the elements are assumed to emit spherical waves). The focusing properties of the PA depend several factors where the most important are the aperture of the array (number of active elements) and the electrical impulse response that determines the temporal resolution. The ALLIN array system used here can use a maximum of 32 elements simultaneously. The elements are located 1 mm apart giving a maximum aperture of 32 mm. The experiments presented in Section 3.6.1 were performed using the maximum number of 32 elements.

3.3 The Synthetic Aperture Focusing Technique

The synthetic aperture focusing technique (SAFT) is a spatial compounding technique where scanning of the area of interest is performed first with a small transducer and then a large synthetic aperture consisting of several measured A-scans is used for focusing.

The conventional time-domain SAFT algorithm performs synthetic focusing by means of coherent summations along hyperbolas. These hyperbolas simply express the distances, or time-delays, from the transducer to the target positions when the transducer is scanned linearly. Note that the PA method uses a real aperture in the same way; that is, compensating for the different propagation delays to the focal point.

There are two assumptions, which justify such approach, they are: 1) the transmitter/receiver is small compared to the wavelength, and 2) the backscattering can be approximated as a sum of contributions from point targets. The first assumption is made to assure that the waveform is the same in all directions so that the signal can be summed coherently. The second assumption implies, for example, that multiple scattering is not considered. Figures 3.1 and 3.2 illustrate how the measured data is formed from a point source. Since both the receiver and the source

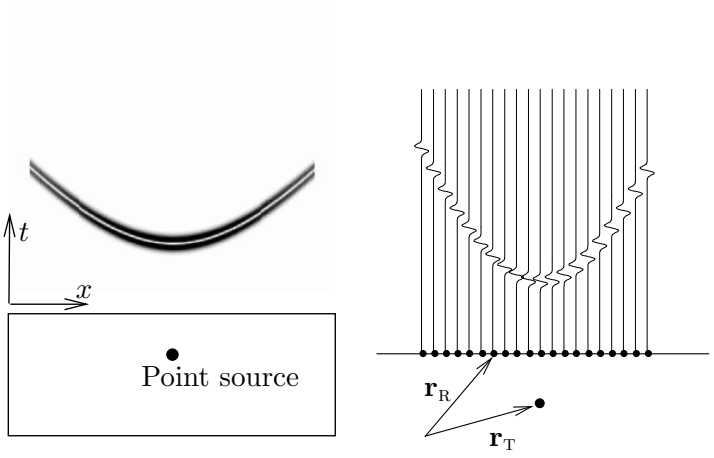

(a) B-scan from a point source

(b) A-Scans

Figure 3.1: Representation of the hyperbola describing the amplitude maxima in the B-scan data originating from a point source at $\mathbf{r}_\mathrm{T}$ (courtesy of R. Hannemann, Kassel University)

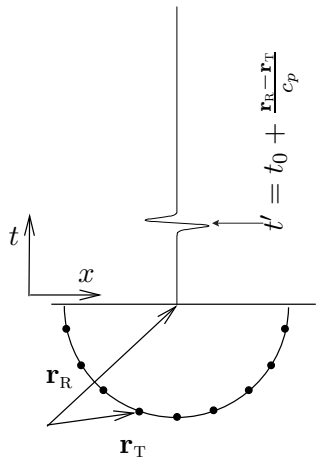

Figure 3.2: The displayed A-scan is caused by a point source located at any position on the half circle with center point $\mathbf{r}_\mathrm{R}$ and radius $|\mathbf{r}_\mathrm{R} - \mathbf{r}_\mathrm{T}|$ (courtesy of R. Hannemann, Kassel University).

.

are small (points) the first non-zero amplitude in the A-scan arrives to the receiver located at $\mathbf{r}_\mathrm{R}$

at time $t' = t_0 + \frac{\mathbf{r}_\mathrm{R} - \mathbf{r}_\mathrm{T}}{c_p}$ where t_0 is the start time of spherical wave from the point source located at $\mathbf{r}_\mathrm{T}$ and c_p is the sound speed of the medium. If pulse-echo imaging is considered then t_0 is the start time of the excitation pulse and propagation delay is doubled. As shown in Figure 3.2 the waveform can originate from any point on the half circle centered at $\mathbf{r}_\mathrm{R}$ with a radius $|\mathbf{r}_\mathrm{R} - \mathbf{r}_\mathrm{T}|$.

As mentioned above, the receiver is scanned first and the focusing is performed afterwards by using a pre-determined set of A-scans to form the synthetic aperture. There are two ways to implement this operation, the so called, A-scan driven approach, and the pixel driven approach [10]. The A-scan driven approach is illustrated in Figure 3.3. Here, a half circle is formed

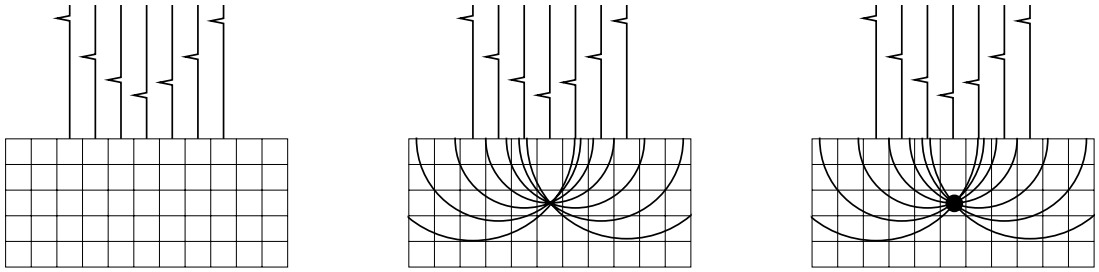

(a) Starting configuration (b) Back propagated circles (c) Finding the scatterer

Figure 3.3: The A-Scan driven approach (courtesy of R. Hannemann Kassel University)

for every sample position in the A-scan where echo is detected. The scatterer is then found at the intersection of all those circles (Figure 3.3(c)). In the pixel driven approach, shown Figure 3.4, a hyperbola is computed for every scatterer position. The amplitude in the reconstructed image is found by adding the number of intersections, or the amplitude at the intersections, of the hyperbolas with the echo responses in the measured data. The maximum value is found when the hyperbola matches the echo response exactly (Figure 3.4(c)). The operation is equivalent to a two-dimensional matched filter if the measured amplitudes in the A-scans are used in the summation along the hyperbolas.

A typical measurement setup for a SAFT experiment is shown in Figure 3.5. The data is collected with a spatial sampling distance Δx between each A-scan at $x_n = n\Delta x$, $n = 0, 1, \ldots, N-1$ and the distance between the target at $\mathbf{r}_\mathrm{T} = (x_{\tilde{n}}, z_m)$ and the receiver at $\mathbf{r}_\mathrm{R} = (x_n, 0)$ is $R = \sqrt{(x_{\tilde{n}} - x_n)^2 + z_m^2}$. Now let the reconstructed image and the measured data be represented by the matrices $\hat{\mathbf{O}}$ and $\mathbf{Y}$ respectively. Then the (pixel driven) SAFT algorithm, which performs reconstruction by compensating for the propagation delay to each image point $(m, \tilde{n})$ by a summation of $2K+1$ terms along hyperbolas, can be expressed as [4]

$$(\hat{\mathbf{O}})_{m,\tilde{n}} = \sum_{\substack{n=\tilde{n}-K \\ \{n|\tilde{n}-K\geq 0, \tilde{n}+K\leq N-1\}}}^{\tilde{n}+K} (\mathbf{Y})_{j,n} \tag{3.1}$$

where j is the propagation delay index given by

$$j \doteq \frac{2}{c_p T_s}\sqrt{(x_{\tilde{n}} - x_n)^2 + z_m^2}. \tag{3.2}$$

The propagation delay index is is a function of $(m, \tilde{n})$—that corresponds to target position $(x_{\tilde{n}}, z_m)$—and the transducer position x_n. The operator $\doteq$ means that j is rounded towards the nearest integer. The synthetic aperture in this case has a length $2K\Delta x$. This operation is essentially a 2D matched filter where the filter is matched to a hyperbola of width $2K\Delta x$.

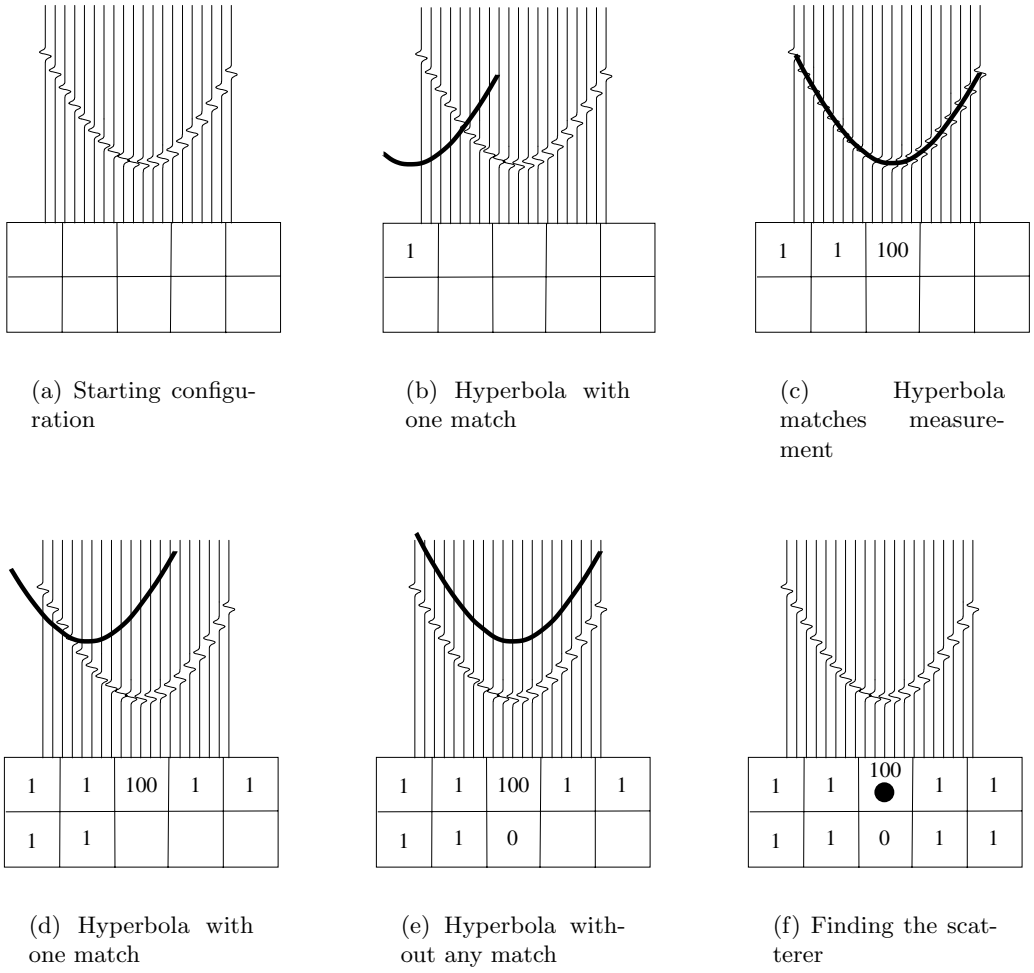

(a) Starting configuration

(b) Hyperbola with one match

(c) Hyperbola matches measurement

(d) Hyperbola with one match

(e) Hyperbola without any match

(f) Finding the scatterer

Figure 3.4: The pixel driven approach (courtesy of R. Hannemann Kassel University)

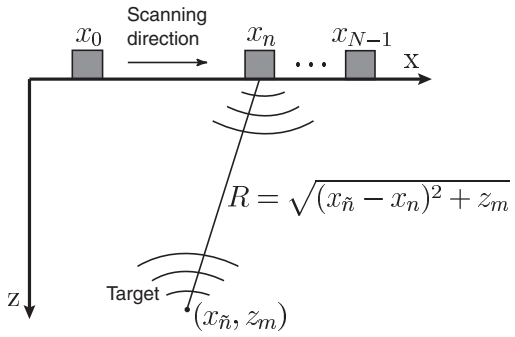

Figure 3.5: Typical measurement setup for a SAFT experiment. The transducer is scanned linearly along the x-axis and at each sampling position, $x_n = n\Delta x$, $n = 0, 1, \ldots, N-1$, a data vector (A-scan) of M samples is recorded. The distance between the transducer, at $(x_n, z = 0)$, and the target position $(x_{\tilde{n}}, z_m)$ is R.

3.3.1 Angular and lateral resolution of SAFT

The purpose of this section is to investigate the characteristics of the SAFT when the transducer size becomes finite, that is, when the transducer is no longer a point source. Since the solution to this problem cannot be obtained using analytical methods, the responses are computed numerically using the DREAM software package [11].

The spatial response of the SAFT formed by N elements located at the distance Δx from each other is defined by its *line spread function* (LSF) known also as a *point spread function* (PSF). For point sources located at any point *(x,y)* in the far field the LSF for single frequency (narrow band excitation) takes the form of the following comb function [12]

$$\text{LSF(x,z)} \cong \frac{\sin(\frac{\pi}{\lambda} N\Delta x \sin(\theta))}{sin(\frac{\pi}{\lambda}\Delta x \sin(\theta))}; \qquad \sin(\theta) = \arcsin\frac{x}{z} \tag{3.3}$$

The maximum amplitude of the LSF occurs at x=0 (see Figure 3.6). The max amplitude is equal to N, which is N times the output of a single element. There is a number of smaller maximums around the main maximum known as *side lobes*. However, the comb function in Eq. 3.3, obtained for continuous wave shows the secondary maximums referred to as *grating lobes* for

$$\sin(\theta_L) = \pm\arcsin\frac{\lambda}{2\Delta x}$$

Therefore, the beam pattern (the main lobe and the sidelobes) repeats itself around each grating

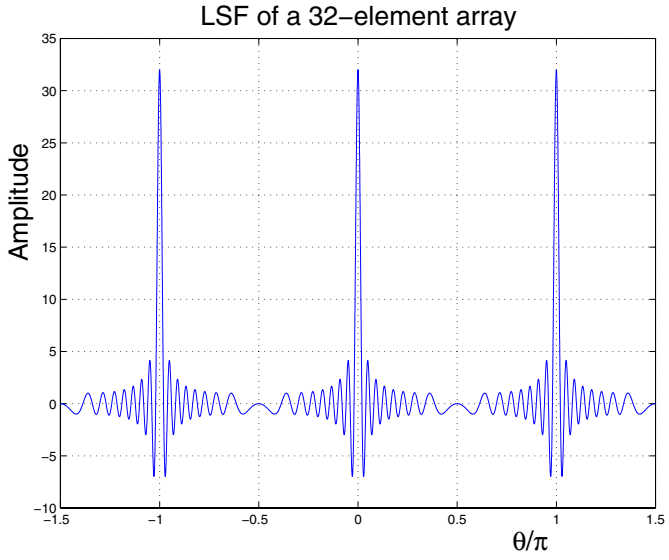

Figure 3.6: LSF of a 32-element array as a function of θ/π.

lobe at θ_L(cf. Figure 3.6). It is worth noting, however, that this effect is substantially reduced if the elements are excited by a short pulse (broadband excitation).

The LSF can be used for the estimation of the resolution of an imaging system. *3-dB angular resolution* of the system is defined as an angle corresponding to the 3-dB width of the LSF function. To facilitate theoretical calculations the resolution δ_θ is often expressed using the angle at which the beam intensity becomes zero, that is

$$\delta_\theta = \arcsin\frac{\lambda}{N\Delta x} \tag{3.4}$$

The corresponding lateral resolution (definition) Δx (expressed in the units of length) at the distance F from the aperture will be

$$\delta_x = F \tan(\delta_\theta) \cong \frac{F\lambda}{N\Delta x} \tag{3.5}$$

Both above expressions are often used as the estimators of the resolution in one-dimensional focusing. However, the LSF defined Eq. 3.3 is an approximation that is valid for point sources in the far field only. In practice, this approximation starts to be valid for the focal distance F at least comparable with the aperture size $N\Delta x$. The accurate solution may be found by numerical evaluation of the Rayleigh's integral defining the field emitted by the aperture.

To illustrate the influence of source size and focal distance on the resolution we present spatial responses of SAFT obtained numerically for three different source sizes at three distances from the aperture. The modeling was performed using parameters of the ALLIN's array in water, that is, frequency 3 MHz and λ=0.5 mm. To avoid spectral aliasing problem the sampling step was $d = \lambda/2 = 0.25$ mm.

The results of modeling are shown in Figure 3.7. Responses obtained for three different source sizes, $a = 0.1$, 3, and 8 mm, respectively, are presented in three columns for three focal distances, $F = 10$, 100 and 190 mm, shown respectively in three rows. Plots of the LSFs in focal plane, corresponding to each row are shown in the first column. The LSFs shown in the three columns are functions of time, obtained for the excitation of one sine period with frequency f=3 MHz. The case $a = 0.1$ models a very small source that corresponds to almost perfect SAFT, a =3 illustrates a realistic value that yields a reasonable resolution for F =100, and, finally, a =8 models the case for which the value of a is much too large. The synthetic apertures for the respective source sizes were constructed of $N = 33$, 125, and 125 elements, respectively, shifted with a step of $\Delta x = 0.25$ mm, which resulted in SAFT apertures, respectively $N\Delta x = 8$, 31, and 31 mm.

Looking at Figure 3.7 we can see that the lateral resolution of a perfect SAFT ($a = 0.1$ mm) increases nearly proportionally to the focal distance according to eq. 3.5. However, this does not apply to the other two cases ($a = 3$ and 8 mm). For a=3 mm the lateral resolution is constant for small focal distances (F=10 and 100 mm) while for a=8 mm this situation occurs for all three focal distances. The resolution for the near located focal points is approximately equal to the source size, which seems to be reasonable since the source in the near field generates a plane wave with a width equal approximately to its size.

3.4 The Spatial Impulse Response

The spatial impulse response (SIR) is an impulse response which is due to the fact that waves coming from different parts of the transducer arrive at different time instants to an observation point. The SIR will not be the same if another observation point is chosen; that is, the SIR acts as a space dependent (low-pass) filter which results in a degradation of temporal and spatial resolution. For an ideal point-like transducer there exist only one (spherical) wave that arrives to the observation point and, therefore, the associated SIR is identical to a Dirac pulse, which means that no temporal smearing is introduced. However, for finite sized planar transducers the SIRs differ significantly from Diracs, particularly in the near field of the transducer. The SIRs must, therefore, be accounted to obtain good performance (high resolution) in ultrasonic imaging when the acoustic waves emitted by the transducer are non-spherical.

The SIRs are determined by the shape of the active area S_R of the transducer, the relative position of the transducer and the observation point (target) $\mathbf{r}_R - \mathbf{r}_T$. In this report two-dimensional imaging is treated where the transducer is scanned linearly along the x-axis. The

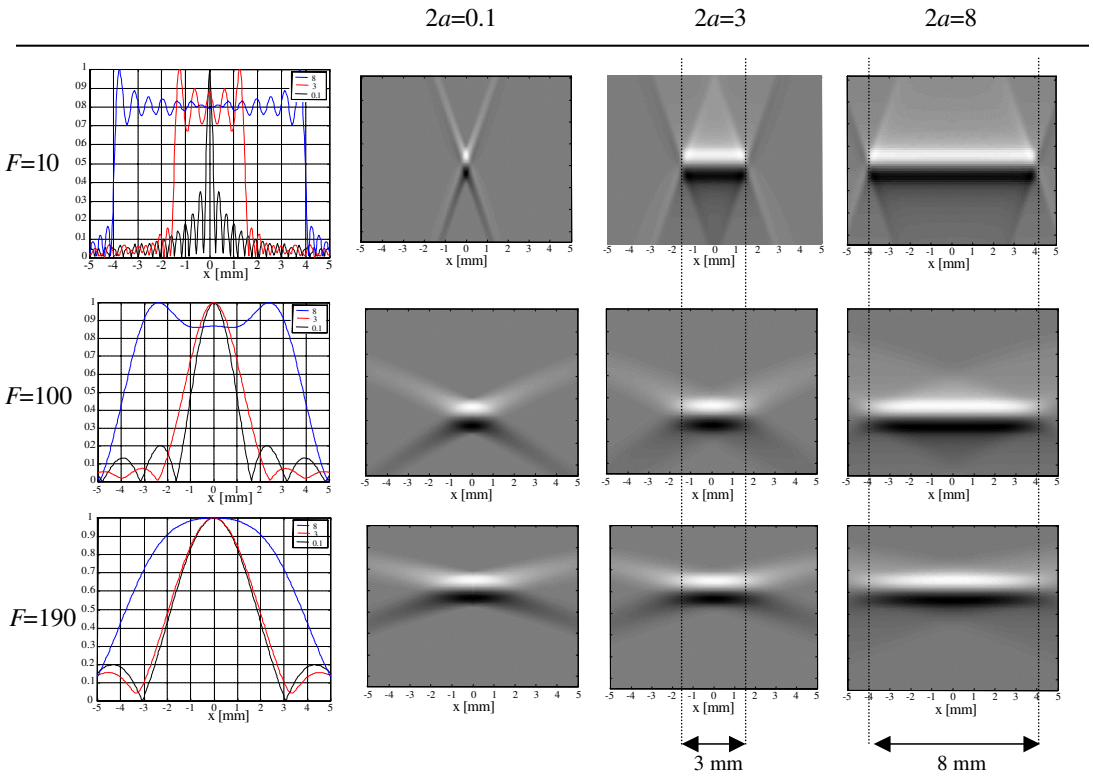

Figure 3.7: Lateral resolution of SAFT for different source size. The LSFs obtained for three different source sizes, $a = 0.1$, 3 and 8 mm, shown in columns for three focal distances, F = 10, 100, and 190 mm, shown respectively in rows. The first column shows the respective LSFs in the focal planes for each row.

SIRs in this case will be a function of transducer position x, time t, and observation point (x', z') only.

For some transducer geometries the SIR can be given analytically but for a general shape of the transducer's active area numerical methods must be employed. The problem becomes even more complicated due to mode conversion, etc, when immersed solids are considered. Since only the two-dimensional case is considered here the computation of the SIR is greatly simplified. For 2D processing to be reasonable responses from scatterers outside the plane defined by $y = 0$ must be small. Therefore, a cylindrically focused transducer is used, shown in Figure 3.8(a), which has a narrow acoustic field around the focal point at 190 mm.

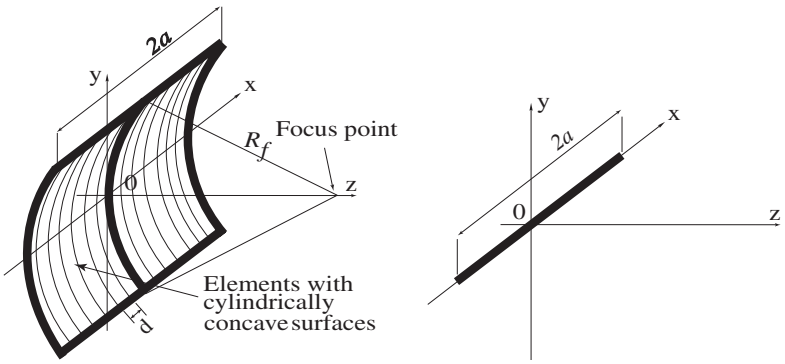

(a) Cylindrically concave transducer ($R_f = 190$ mm, $d = 1$ mm)

(b) Line strip transducer

Figure 3.8: Transducer geometries.

To assure that the numerical algorithm that is used here (and in [7]) to compute the SIRs is resonable it will first be compared with the analytical solution for a line (or strip) transducer (see Figure 3.8(b)). Then, it will also compared with an algorithm from the DREAM software package [11] that is capable of computing SIRs for concave transducers.

Geometrically the strip and the concave transducer are identical in the x-z plane but in the y-z plane they are different. The strip transducer emits spherical waves in the y-z plane, that is, the y-z plane SIRs are all Diracs. The concave transducer also has this property, but only at a straight line located at its focus. Thus, the normalized SIRs of concave transducer at its focus are similar to those of the strip transducer, which implies that the strip SIRs can be utilized for the concave case as well.

These comparisons are valid for the fluid case only. In our experiments immersed solids are used and the numerical line-strip algorithm is modified using a ray tracing technique to also treat immersed solids. This is an approximate technique, since ray tracing is used for SIR calculation and a concave transducer is used for the measurements. The fluid-solid interface impairs slightly the geometrical focusing of the concave transducer resulting in slightly longer y-z SIRs than those for the fluid case. The numerical algorithm that is used below to compute fluid SIRs for the concave transducer is not yet implemented for immersed copper, which is the reason that the strip model is used here.

3.4.1 Spatial Impulse Response in Fluid

If scattering from a point-like target is considered the target can be seen as an equivalent source of spherical waves. Assume that the normal velocity of the transducer surface is $v(t)$, the sound velocity is c_p, the density of the fluid is ρ_0, and that the target has an elementary surface s_e. Then the pressure at the target $\mathbf{r}_\mathrm{T}$ can be expressed as

$$p(\mathbf{r}_\mathrm{T},t) = \rho_0 v(t) * \frac{\partial}{\partial t}\left(\int_{S_R} \frac{\delta(t-(|\mathbf{r}_\mathrm{T}-\mathbf{r}_\mathrm{R}|/c_p))}{2\pi|\mathbf{r}_\mathrm{T}-\mathbf{r}_\mathrm{R}|} dS_R\right)$$

and the total pressure received by the transducer can be expressed as [13]

$$\langle p\rangle(\mathbf{r}_\mathrm{T},t) = \frac{s_e}{2c_p} p(\mathbf{r}_\mathrm{T},t) * \frac{\partial}{\partial t}\left(\int_{S_R} \frac{\delta(t-(|\mathbf{r}_\mathrm{R}-\mathbf{r}_\mathrm{T}|/c_p))}{2\pi|\mathbf{r}_\mathrm{R}-\mathbf{r}_\mathrm{T}|} dS_R\right).$$

This formula states that the received total pressure is a convolution of the double path (velocity potential) SIR with the normal velocity $v(t)$. The total pressure at time t is formed by summing the pressure for all $\mathbf{r}_\mathrm{R}$ on the transducer surface where $t = |\mathbf{r}_\mathrm{R}-\mathbf{r}_\mathrm{T}|/c_p$ is satisfied weighted by the decay of spherical wave propagation $(1/2\pi|\mathbf{r}_\mathrm{R}-\mathbf{r}_\mathrm{T}|)$. First let

$$h(\mathbf{r},t) \triangleq \int_{S_R} \frac{\delta(t-(|\mathbf{r}-\mathbf{r}_\mathrm{R}|/c_p))}{2\pi|\mathbf{r}-\mathbf{r}_\mathrm{R}|} dS_R$$

then the double path SIR is defined as

$$h^{\mathrm{SIR}}(\mathbf{r}_\mathrm{T},t) \triangleq \frac{1}{2\rho_0 c_p} h(\mathbf{r}_\mathrm{T},t) * h(\mathbf{r}_\mathrm{T},t). \tag{3.6}$$

In general a closed form of the SIRs can not be found which implies that numerical methods must be used. For the simple line source used here there exist, however, an analytical solution.

3.4.2 Analytic Solution for a Line Source

The geometry of the line strip is shown in Figure 3.8(b). The double path spatial impulse response of a uniformly excited line strip is given by [14]

$$h_c^{\mathrm{SIR}}(x,z,t) = g(x,t)\frac{2}{\sqrt{t^2-t_z^2}} * g(x,t)\frac{2}{\sqrt{t^2-t_z^2}} \tag{3.7}$$

where the definition of the gating function, $g(x,t)$, is shown in Table 3.1 with $t_z = z/c_p$.

$t_{1,2} = t_z\sqrt{1+\left(\frac{a\mp\lvert x\rvert}{z}\right)^2}$	
$\lvert x\rvert \le a$	$\lvert x\rvert > a$
$g(x,t) = \begin{cases} 2 & \text{for } t_z \le t \le t_1 \\ 1 & \text{for } t_1 < t \le t_2 \\ 0 & \text{otherwise} \end{cases}$	$g(x,t) = \begin{cases} 1 & \text{for } t_1 < t \le t_2 \\ 0 & \text{otherwise} \end{cases}$

Table 3.1: Gating function for the spatial impulse response of a uniformly exited line strip.

3.4.3 Sampling the SIR

In order to implement the algorithms in a computer a discrete representation of the SIRs is needed. This is accomplished here by summing all contributions from the (continuous) SIR in the actual sampling interval. That is, the sampled SIR is defined as

$$h^{\mathrm{SIR}}(x, z, t_m) \triangleq \int_{t_m}^{t_m+T_s} h_c^{\mathrm{SIR}}(x, z, t)dt. \tag{3.8}$$

Figure 3.9 shows two examples of the SIRs calculated using (3.7) and (3.8) for two line strip transducer with widths of 1 and 16 mm, respectively. As can be seen in Figure 3.9 the SIRs are

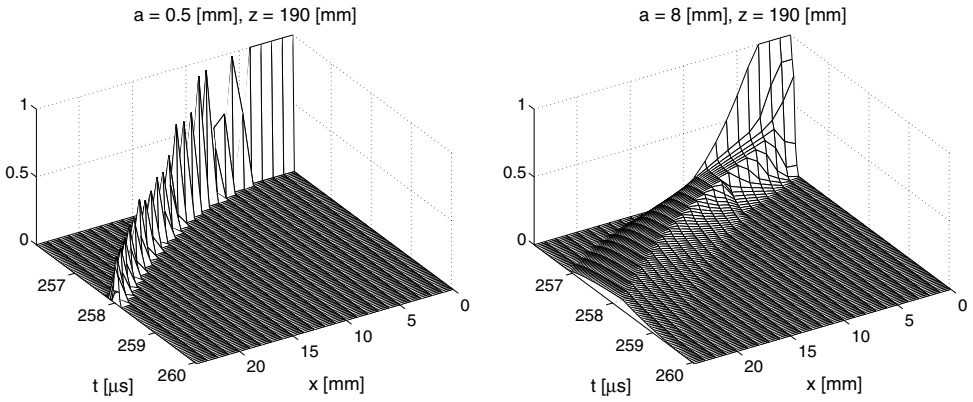

(a) 1 mm strip transducer.

(b) 16 mm strip transducer.

Figure 3.9: Normalized sampled double path spatial impulse responses for the strip transducer at $z = 190$ mm.

much shorter for the 1 mm transducer compared to those of the 16 mm transducer, particularly for $|x| > a$. The SIRs for a small transducer are essentially Dirac-functions with different propagation delays (the property needed for successful application of the SAFT method). Note that the amplitude of the SIRs in Figure 3.8(a) varies in a apparently random manner. This is a numerical effect due to the position of the sampling intervals relative to the time delays of the SIRs. If a SIR is completely inside one sampling interval the amplitude will be high. If the same SIR is shifted so that if falls within two sampling intervals the amplitude will be distributed in both intervals according to Eq. (3.8). The amplitude will, therefore, be lower but the energy in the two SIRs is the same.

3.4.4 Calculation of SIRs for a Cylindrically Focused Transducer using DREAM

The DREAM package is a software tool for numerically computing SIRs for various types of transducers [11]. The present version does not have capability for computing SIRs in immersed solids. Which is one of the reasons for using the strip model.[1] The reason for using a concave transducer was, as mentioned above, the need to obtain a narrow acoustic field in the y-direction so that the field is nearly two-dimensional. Figure 3.10 shows the SIRs computed using DREAM for x- and y-direction, respectively, for the concave transducer. As can be seen in Figure 3.10(b) the y-direction SIRs drops off fast when y increases and the 3 dB width is only 2–3 mm indicating

[1] Another reason for using the strip model is that this method of computation SIRs is much faster than computing SIRs using DREAM.

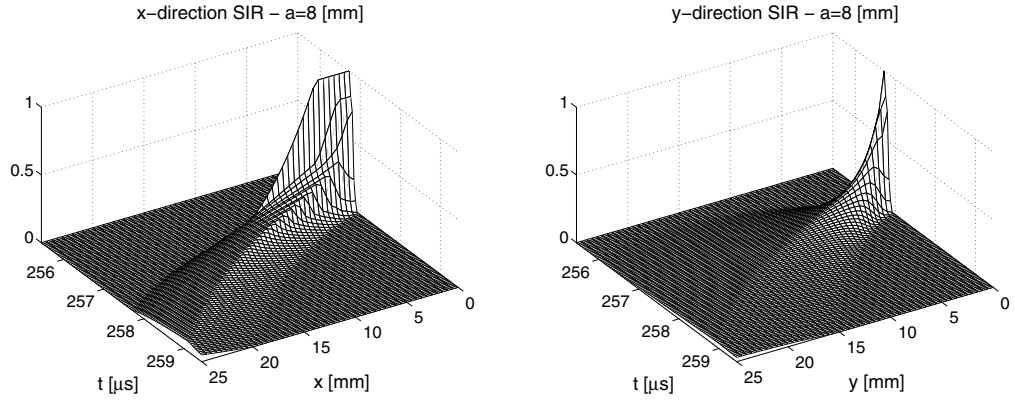

(a) x-direction SIRs ($y = 0$).

(b) y-direction SIRs ($x = 0$).

Figure 3.10: Normalized double path spatial impulse responses at $z = 0$ computed for a cylindrically concave transducer with $a = 8$ mm, $R_f = 190$ mm, with a width in y-direction of 33 mm using DREAM.

that the two-dimensional approach is reasonable. Note that the x-direction SIRs are nearly identical to those for the strip transducer in Figure 3.9(b) (the time interval in Figure 3.10 has been shifted compared to Figure 3.9 to accommodate for the y-direction SIRs that starts earlier than the x-direction SIRs). The modeling error introduced by using strip SIRs instead of SIRs for the concave transducer is, therefore, small in the geometrical focal zone.

3.4.5 Spatial Impulse Response in Immersed Solid

Since the objective here is to perform imaging of immersed copper the fluid SIRs discussed above must be recomputed or compensated. The water-copper interface complicates the computation due to the different sound speeds, mode conversion, reflection coefficients etc. In this report an approximate ray-tracing approach i used. This compensates for the different sound speeds and the different acoustic ray angles in the two media using pressure waves only. Practically this is implemented by compensating the SIRs for the line strip model using Snell's law. Two examples of SIRs computed using the ray-tracing approach are shown in Figure 3.11.

3.5 The Minimum Mean Square Error Filter

As described in Section 3.4 the SIRs introduce a position dependent smearing which results in an unsharp ultrasonic image.[2] To improve resolution in the ultrasonic images a linear model of the imaging system is used and then a linear filter is applied which minimizes the mean squared error (MMSE) of the imaging system. The details about the MMSE filter can be found in [8]. A short summary and the main equations of the MMSE filter is restated here for clarity.

[2]The SAFT algorithm does not take this smearing into consideration. This results in unsharp images if the SIRs have a long duration. As mentioned above a small transducer results in short SIRs, hence the SAFT algorithm requires a transducer with a small active area.

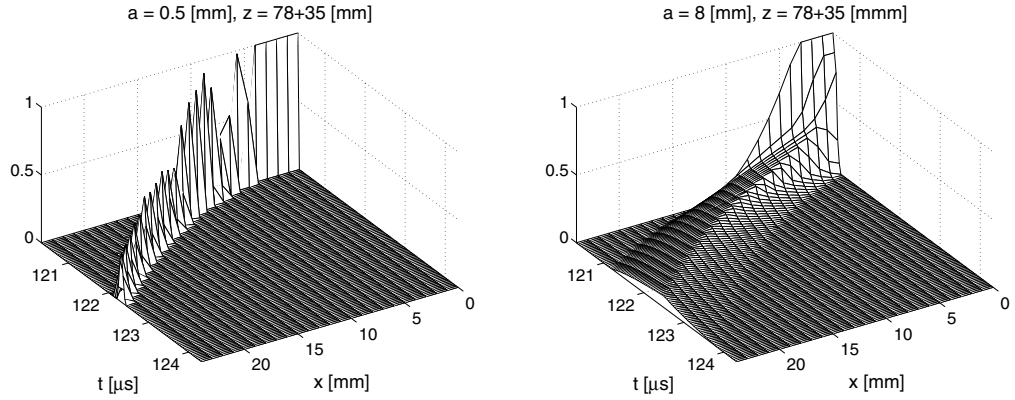

(a) 1 mm strip transducer.

(b) 16 mm strip transducer.

Figure 3.11: Normalized sampled double-path spatial impulse responses at 35 mm in copper with a water path of 78 mm using ray-tracing compensated SIRs for the strip transducer.

3.5.1 A Discrete Linear Model of the Imaging System

If scattering from point-targets only is considered the electrical output $u_{\mathrm{o}}(x,t)$ of the ultrasonic imaging system can be expressed as convolutions of the following form [8, 13]

$$u_{\mathrm{o}}(x,t) = s_{\mathrm{e}} \sum_{(x_{\mathrm{T}},z_{\mathrm{T}})\in\mathcal{T}} h_c^{\mathrm{SIR}}(x-x_{\mathrm{T}},z_{\mathrm{T}},t) * h_{\mathrm{e}}(t) * u_{\mathrm{i}}(t) + e(t) \tag{3.9}$$

The sum is taken over all point target positions $\mathcal{T}$ and $h_c^{\mathrm{SIR}}(x,z,t)$ is the double path continuous time SIR, $h_{\mathrm{e}}(t)$ is the double path electrical impulse response, $e(t)$ is the measurement noise, and $u_{\mathrm{i}}(t)$ is the excitation signal.

A time-discrete version of (3.9) is obtained by sampling the SIRs and the electrical impulse response, and replacing the continuous time convolutions in (3.9) by discrete time convolutions. A discrete representation of the targets is obtained by defining the so called *object function* $o(x,z)$ as

$$o(x,z) \triangleq \begin{cases} s_{\mathrm{e}} & \text{for } \; x,z \in \mathcal{T} \\ 0 & \text{otherwise.} \end{cases} \tag{3.10}$$

If $o(x,z)$ is discretized, it only takes values at the sampling points, hence, $o(x,z)$ can be represented by a matrix $\mathbf{O}$.

A discrete version of (3.9) for an A-scan measurement vector can be expressed as

$$\mathbf{y}_n = \mathbf{H} \sum_{\tilde{n}=n-L}^{n+L} \mathbf{P}_{d(\tilde{n},n)} \mathbf{o}_{\tilde{n}} + \mathbf{e}_n \tag{3.11}$$

where $\mathbf{e}_n$ is the noise, and $\mathbf{H}$ is a $M \times M$ finite impulse response matrix defined by the *system* impulse response $h(t) \triangleq h_e(t) * u_i(t)$. The vector $\mathbf{o}_{\tilde{n}}$ denotes column $\tilde{n}$ in $\mathbf{O}$ and the matrix $\mathbf{P}_{d(\tilde{n},n)}$ contains the sampled SIRs at a distance $d(\tilde{n},n) = x_{\tilde{n}} - x_n$ (which is the horizontal distance between the observation point and the transducer).

Eq. (3.11) is a discrete time model for a single A-scan measurement. By using vectorizing $\mathbf{O}$ and the B-scan measurement matrix $\mathbf{Y}$ into column vectors $\mathbf{o}$ and $\mathbf{y}$ respectively, a B-scan model can be expressed according to

$$\mathbf{y} = \mathbf{H}_0 \mathbf{S}_{\mathrm{SIR}} \mathbf{o} + \mathbf{e} \tag{3.12}$$

where $\mathbf{H_0}$ is a block diagonal $MN \times MN$ matrix with N $\mathbf{H}$s along its diagonal. Eq. (3.12) is a discrete linear model for 2D ultrasonic imaging when the backscattering is considered as a sum of responses from point targets.

3.5.2 The Inverse Filter

The inverse filter is found by minimizing the expected reconstruction error

$$\begin{aligned} J &= E\{\|\mathbf{o} - \mathbf{K}\mathbf{y}\|^2\} \\ &= \mathrm{tr}\{\mathbf{C}_{oo}\} - 2\mathrm{tr}\{\mathbf{K}\mathbf{H}_0\mathbf{S}_{\mathrm{SIR}}\mathbf{C}_{oo}\} + \mathrm{tr}\{\mathbf{K}(\mathbf{H}_0\mathbf{S}_{\mathrm{SIR}}\mathbf{C}_{oo}\mathbf{S}_{\mathrm{SIR}}^T\mathbf{H}_0^T + \mathbf{C}_{ee})\mathbf{K}^T\} \end{aligned} \tag{3.13}$$

where $\mathrm{tr}\{\cdot\}$ is the trace operator and $E\{\cdot\}$ is the expectation operator.

The filter matrix, $\hat{\mathbf{K}}$, which minimizes (3.13), is the minimum mean square error estimator for the linear model (3.12) [15]

$$\begin{aligned} \hat{\mathbf{K}} &= \arg\min_{\mathbf{K}} J = \mathbf{C}_{oo}\mathbf{S}_{\mathrm{SIR}}^T\mathbf{H}_0^T(\mathbf{H}_0\mathbf{S}_{\mathrm{SIR}}\mathbf{C}_{oo}\mathbf{S}_{\mathrm{SIR}}^T\mathbf{H}_0^T + \mathbf{C}_{ee})^{-1} \\ &= (\mathbf{C}_{oo}^{-1} + \mathbf{S}_{\mathrm{SIR}}^T\mathbf{H}_0^T\mathbf{C}_{ee}^{-1}\mathbf{H}_0\mathbf{S}_{\mathrm{SIR}})^{-1}\mathbf{S}_{\mathrm{SIR}}^T\mathbf{H}_0^T\mathbf{C}_{ee}^{-1}. \end{aligned} \tag{3.14}$$

An estimate of the object function $\hat{\mathbf{o}}$ can now be obtained by performing the matrix-vector multiplication $\hat{\mathbf{K}}\mathbf{y}$ or by solving the equation system $(\mathbf{C}_{oo}^{-1} + \mathbf{S}_{\mathrm{SIR}}^T\mathbf{H}_0^T\mathbf{C}_{ee}^{-1}\mathbf{H}_0\mathbf{S}_{\mathrm{SIR}})\hat{\mathbf{o}} = \mathbf{S}_{\mathrm{SIR}}^T\mathbf{H}_0^T\mathbf{C}_{ee}^{-1}\mathbf{y}$.

Note that there is no assumptions regarding the shape of the transducer's active area nor the form if its electrical impulse response. Of course these parameters will be important factors in the total performance of the imaging system but as long as the SIRs can be calculated and the electrical impulse response can be obtained the MMSE will give the filter with the minimum mean squared error for the system at hand.

3.6 Measurements

The objective of this investigation was to evaluate the resolution of the SAFT, MMSE, and PA methods in the Rayleigh's sense; that is, the ability to distinguish between two closely spaced scatterers. The performance of the methods have been investigated using the ALLIN system and an immersed copper block with four pairs of side drilled holes (SDHs) with a spacing between the holes ranging from 1 to 7 mm (see Figure 3.12). The ALLIN array system facilitates the

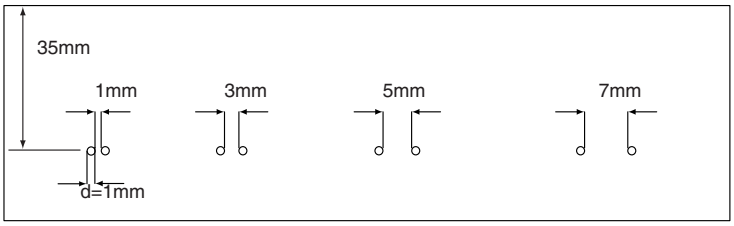

Figure 3.12: Copper Test Block.

measurements since the transmitting aperture easily can be changed by selecting the number of active elements. In our experiments all active elements were fired simultaneously which simulates a planar (non-focused) transducer. Another benefit from using this approach is that the same electronics is used for all transducer sizes giving measurements and results that can be compared directly.

The B-scan data were recorded with a spatial sampling distance of 1 mm between the individual A-scans. The number of elements used for the MMSE algorithm was, respectively, $1, 2, \ldots, 12$, and 20 elements, while for the PA method 32 elements were used. Since the SAFT algorithm requires a small transmitting aperture it was only applied to the 1 element data (B-scan), which was the smallest transducer available. Ideally, the spatial sampling distance should be smaller than 1 mm, particularly for the smaller hole spacing (1 mm and 3 mm). Our present hardware puts, however, limits on the spatial sampling since a finer sampling grid increases amount of memory needed for the filter computation. A quantitative measure of the resolution is, for this reason, not given here, and, as it can be seen in Appendix 3.A, 3.B, and 3.C the results are somewhat sensitive to the starting point of the measurements—a shift of 0.5 mm may give a slightly different result. The spatial sampling is, however, fine enough to evaluate the performance of the methods for this application.

To facilitate the comparison the electrical impulse response was not deconvolved in any of the methods ($\mathbf{H}_0 = \mathbf{I}$ in Eq. (3.14)). Temporal deconvolution, that is, inverse filtering of the electrical impulse response improves the temporal resolution as discussed in [7, 16]. The price that is paid for obtaining the higher temporal resolution is a higher noise level. The performance of this operation depends on the parameters of the deconvolution filter that not necessary are the same in all methods compared here. Temporal deconvolution would, therefore, complicate the comparison of the obtained results.

3.6.1 Results

A summary of the results is shown in Figure 3.13 (the complete results can be found in Appendix 3.A, 3.B, and 3.C). The "profile" plots show the max amplitude in each A-scan and Δd denotes the spacing between the SDHs. From Figure 3.13 can be seen that the resolution of the PA and the SAFT method is in the same order. This is not unexpected since both methods are based on the same idea of delay and summation. The difference between them is that the PA method focuses in both transmission and reception whilst the SAFT algorithm focuses in reception only. A consequence of this is that the SAFT method is more sensitive for nearby scattering. The responses from closely spaced scatterers will contribute to the summation as well, which results in artifacts in the processed images (see Figure 3.16 in Appendix 3.B). The SAFT method has, however, the benefit of improving resolution at all image points in contrary to the PA approach, which only produces focused images at one specific depth.

Analysis of the results presented in Figure 3.13 shows that the MMSE method yields better resolution compared to both the SAFT and the PA. The SAFT and the PA method were able to resolve the SDHs with spacings of $\Delta d \geq 5$ mm while the MMSE resolved all the SDHs. This indicates that the MMSE filter is capable of producing the resolution superior to that of the PA and SAFT methods that essentially are 2D matched filters [17, 18]. Our preliminary results show that the MMSE filter has always better or equal resolution comparing to the matched filter based approaches. Note that the transducer size is important for the MMSE method as well. The resolution drops when the transducer size increases (see figures in Appendix 3.C). This is natural since the ultrasonic data contains little information that can separate two scatterers when both scatterers are located under a planar transducer. The data that is most "informative" is contained in those A-scans that are located close to the edges of the transducer. When the transducer becomes larger the beam will become narrower and the "informative edge A-scans" will thus be fewer.

In summary the MMSE method has a superior resolution compared to that of the PA method and the SAFT. Its resolution, however, is achieved at the price of the increased signal-to-noise ratio (this is clearly seen when comparing the profile plots for the PA and the MMSE method).

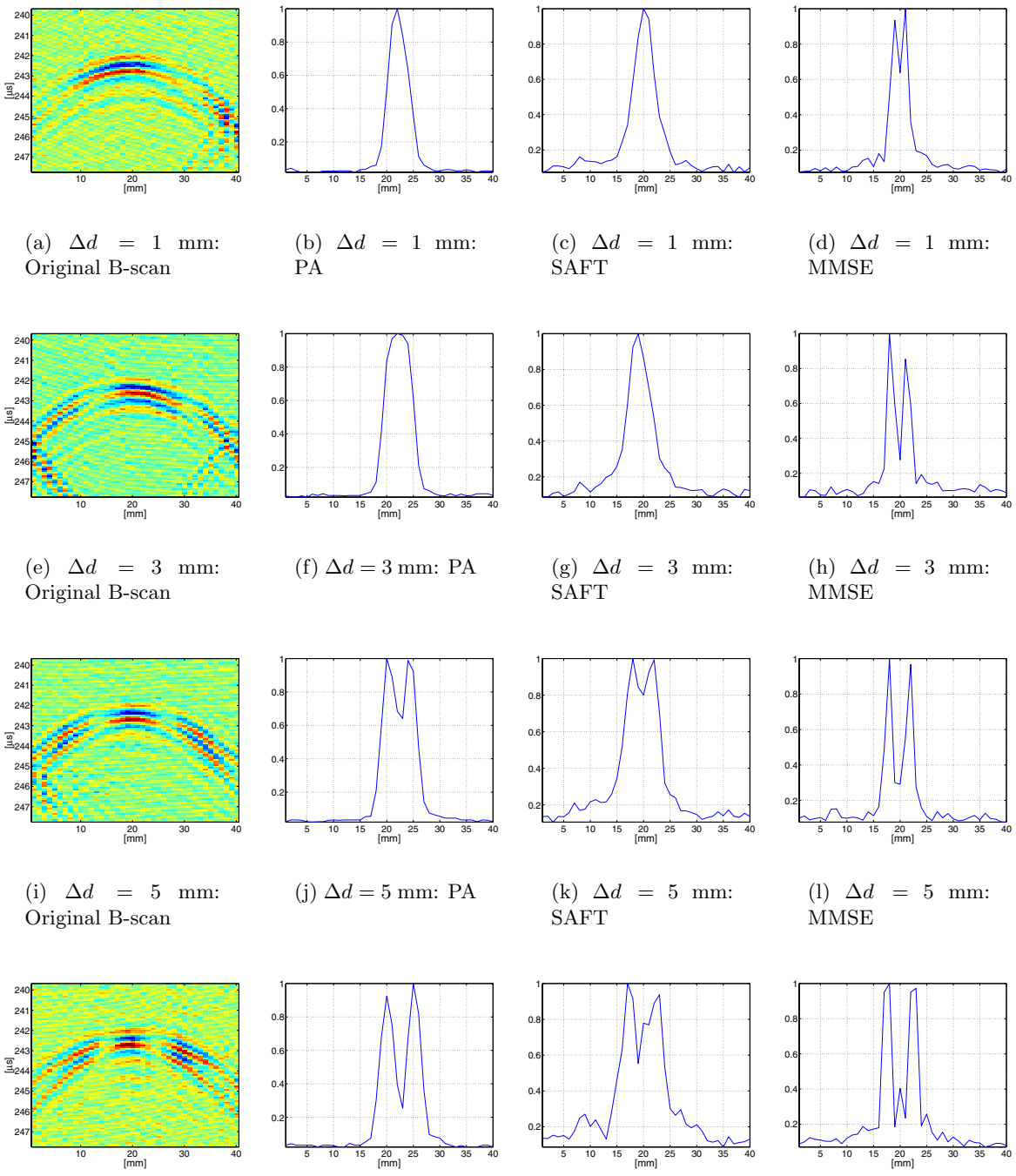

(a) $\Delta d = 1$ mm: Original B-scan

(b) $\Delta d = 1$ mm: PA

(c) $\Delta d = 1$ mm: SAFT

(d) $\Delta d = 1$ mm: MMSE

(e) $\Delta d = 3$ mm: Original B-scan

(f) $\Delta d = 3$ mm: PA

(g) $\Delta d = 3$ mm: SAFT

(h) $\Delta d = 3$ mm: MMSE

(i) $\Delta d = 5$ mm: Original B-scan

(j) $\Delta d = 5$ mm: PA

(k) $\Delta d = 5$ mm: SAFT

(l) $\Delta d = 5$ mm: MMSE

(m) $\Delta d = 7$ mm: Original B-scan

(n) $\Delta d = 7$ mm: PA

(o) $\Delta d = 7$ mm: SAFT

(p) $\Delta d = 7$ mm: MMSE

Figure 3.13: Summary of the results. The data used for the SAFT and the MMSE methods were acquired using 1 element (shown in fig (a),(e), (i), and (m). The PA data (shown in Figure 3.14) was acquired using 32 elements focused at 35 mm in the block.

3.7 Discussion

We proposed a new algorithm for synthetic aperture imaging (SAI) and evaluated its spatial resolution in comparison with classical phased array imaging and SAFT. The proposed algorithm that compensates for the diffraction effects introduced by the transducer takes the form of a 2D filter based on a MMSE criterion.

We have shown that the resolution of the MMSE algorithm is superior compared to both PA imaging and the SAFT method for imaging of an immersed copper specimen. This is a consequence of the fact that the PA and SAFT methods are 2D matched filters [17, 18] that have the property of maximizing the signal-to-noise ratio for one image point without respect to other image points [19]. That is, these methods maximize the energy at one image point without regarding main lobe width and side-lobe levels. The MMSE method, on the other-hand, considers all image points and produces the solution with the maximum resolution possible for the actual measurement noise level. This results in a high resolution if the measurement noise is low and and in a low resolution if the noise is high. It can in fact be shown that the MMSE solution goes toward the matched filter solution when the noise increases. Hence, the MMSE solution has always better or equal resolution compared to the matched filter based approaches.

It is worth noting that the size of the transducer is also important for the MMSE method. The resolution drops when the transducer size is increased because that part of the area-of-interest (AOI) which is under the transducer will also increase. Two scatterers can not be distinguished as long as they are under the transducer since the waves emitted by the middle part of a long transducer are almost planar and when scattered from a small target they do not carry much information about it. If the size of the AOI is fixed while the size of the transducer is increased a smaller part of the received data will contain useful information scattered in different directions. This can be alleviated by increasing the synthetic aperture (i.e., AOI) which consumes more computer memory and CPU time.

An advantage of a large transducer is that it transmits more acoustic energy than a small one resulting in an improved SNR. The receiver gain must, however, be lowered to avoid clipping of the data since the dynamic range of the commonly used analogue-to-digital converters (ADCs) is limited (8 bit ADCs are used in the Allin). Lowering the gain results in lower amplitude of the edge A-scans (the data containing useful information) relative to the dynamic range of the ADCs, which further decreases the performance. Thus, for the MMSE, similarly as for the SAFT method the use of a relatively small transducer ensures good resolution; the reasons for that are, however, different for the two methods. Note that the MMSE method is superior to the SAFT algorithm as well as to the PA method for a transducer size up to 10–12 mm (at the distances analyzed in our experiments).

The strength of the MMSE method is its capability of improving resolution for any shape of the transducer as long as its associated SIRs can be computed or measured. This feature can be applied for upgrading the existing array systems in many applications. Ultrasonic systems commonly used today employ 1D arrays that only allow focusing in one dimension (they may also be provided with a fixed focus in the second dimension). For such systems the MMSE method is capable of significant improving the resolution in the second dimension by performing synthetic focusing using the data obtained from scanning in the unfocused direction. In this way a system with a high lateral resolution in two dimensions can be obtained.

Bibliography

[1] M. Fatemi and A.C. Kak. Ultrasonic B-scan imaging: theory of image formation and a technique for restoration. *Ultrasonic Imaging*, 2:1–47, 1980.

[2] W. Vollmann. Resolution enhancement of ultrasonic B-scan images by deconvolution. *IEEE Trans. on Sonics and Ultrasonics*, 29(2):78–83, March 1982.

[3] D. Iraca, L. Landini, and L. Verrazzani. Power spectrum equalization for ultrasonic image restoration. *IEEE Trans. on Ultrasonics, Ferroelectrics, and Frequency Control*, 36(2):216–222, March 1989.

[4] J.A. Seydel. *Ultrasonic Synthetic-aperture Focusing Techniques in NDT*. Research Techniques for Nondestructive Testing. Academic Press, 1982.

[5] K. Nagai. A new synthetic-aperture focusing method for ultrasonic B-scan imaging by the Fourier transform. *IEEE Trans. on Sonics and Ultrasonics*, 32(4):531–536, July 1985.

[6] K. Mayer, R. Marklein, K.J. Langenberg, and T. Kreutter. Three-dimensional imaging system based on fourier transform synthetic aperture focusing technique. *Ultrasonics*, 28:241–255, July 1990.

[7] Tadeusz Stepinski, Fredrik Lingvall, and Ping Wu. Inspection of copper canisters for spent nuclear fuel by means of ultrasound — ultrasonic imaging of eb weld, theory of harmonic imaging of welds, and nde of cast iron. Technical Report TR-01-36, SKB, 2001.

[8] F. Lingvall and T. Stepinski. Synthetic aperture imaging using sources with finite aperture—deconvolution of the spatial impulse response. *Submitted to J. Acoust. Soc. Am.*, 2002.

[9] T. Stepinski and P. Wu. Ultrasonic inspection of nuclear fuel copper canisters. Technical Report PR-97-01, SKB, 1997.

[10] R. Hannemann. *Modeling and Imaging of Elastodynamic Wave Fields in Homogenous Anisotropic Media*. PhD thesis, Kassel University, 2001.

[11] B. Piwakowski and K. Sbai. A new approach to calculate the field radiated from arbitrarily structured transducer arrays. *IEEE Trans. on Ultrasonics, Ferroelectrics, and Frequency Control*, pages 422–440, 1999.

[12] G.S. Kino. *Acoustic Waves: Devices, Imaging and Analog Signal Processing*, volume 6 of *Prentice-Hall Signal Processing Series*. Prentice-Hall, 1987.

[13] A. Lhémery. Impulse-response method to predict echo-responses from targets of complex geometry. Part I: Theory. *J. Acoust. Soc. Am.*, pages 2799–2807, November 1991.

[14] H. Lasota and R. Salamon. Application of time-space impulse responses to calculations of acoustic field in imaging systems. *Acoustic Imaging*, pages 493–512, 1980.

[15] S.M. Kay. *Fundamantals of Statistical Signal Processing: Estimation Theory*, volume I. Prentice Hall, 1993.

[16] P. Wu, F. Lingvall, and T. Stepinski. Inspection of copper canisters for spent nuclear fuel by means of ultrasound — electron beam evaluation, harmonic imaging, materials characterization and ultrasonic modelling. Technical Report TR-00-23, SKB, 2000.

[17] G.L. Turin. An introduction to matched filters. *IRE Trans. on Information Theory*, pages 311–329, 1960.

[18] A. Papoulis. *Probability, Random Variables and Stochastic Processes*. McGraw-Hill, 2nd edition, 1984.

[19] C.H. Frazier and Jr. W.D. O'Brien. Synthetic aperture techniques with a virtual source element. *IEEE Trans. on Ultrasonics, Ferroelectrics, and Frequency Control*, 45(1):196–207, January 1998.

3.A Results using Phased Array

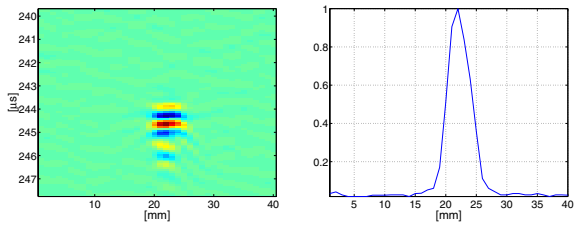

(a) $\Delta d = 1$ mm: B-scan

(b) $\Delta d = 1$ mm: Profile

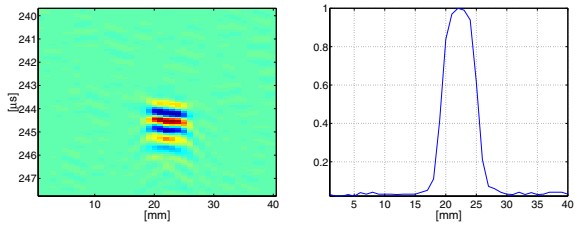

(c) $\Delta d = 3$ mm: B-scan

(d) $\Delta d = 3$ mm: Profile

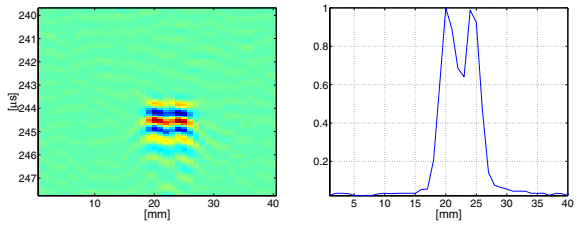

(e) $\Delta d = 5$ mm: Original B-scan

(f) $\Delta d = 5$ mm: Profile

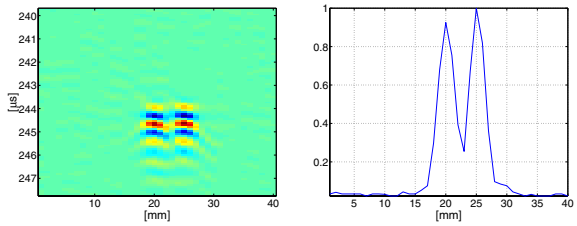

(g) $\Delta d = 7$ mm: Original B-scan

(h) $\Delta d = 7$ mm: Profile

Figure 3.14: Focused Phased Array using 32 Elements.

3.B Results using the SAFT Method

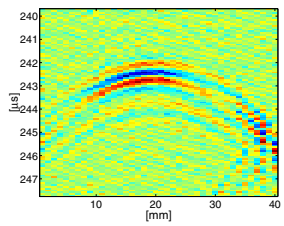

(a) $\Delta d = 1$ mm: Original B-scan

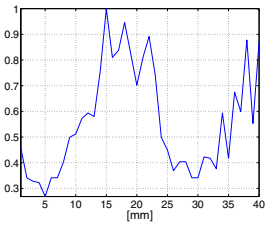

(b) $\Delta d = 1$ mm: Original Profile

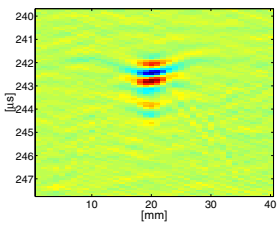

(c) $\Delta d = 1$ mm: Processed B-scan

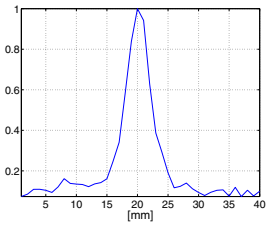

(d) $\Delta d = 1$ mm: Processed Profile

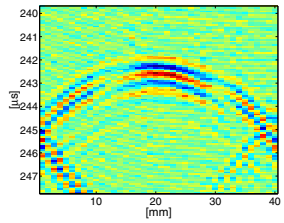

(e) $\Delta d = 3$ mm: Original B-scan

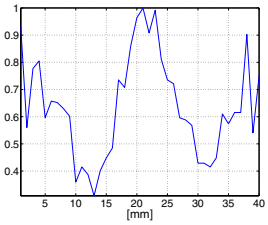

(f) $\Delta d = 3$ mm: Original Profile

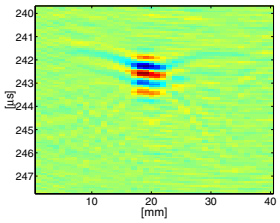

(g) $\Delta d = 3$ mm: Processed B-scan

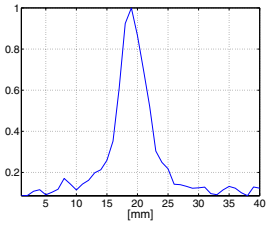

(h) $\Delta d = 3$ mm: Processed Profile

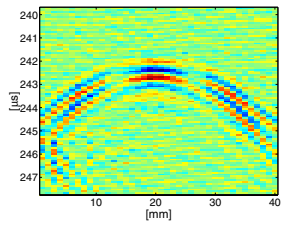

(i) $\Delta d = 5$ mm: Original B-scan

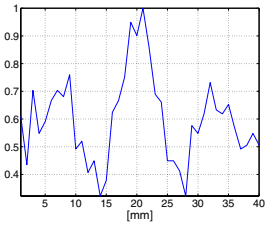

(j) $\Delta d = 5$ mm: Original Profile

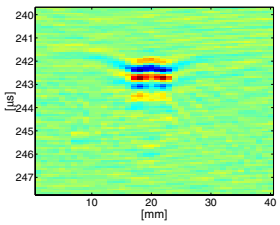

(k) $\Delta d = 5$ mm: Processed B-scan

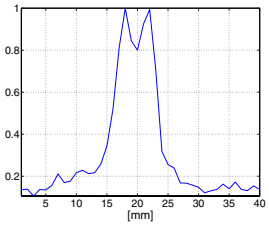

(l) $\Delta d = 5$ mm: Processed Profile

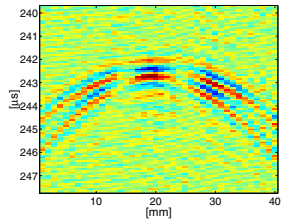

(m) $\Delta d = 7$ mm: Original B-scan

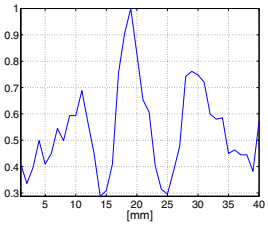

(n) $\Delta d = 7$ mm: Original Profile

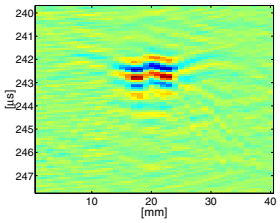

(o) $\Delta d = 7$ mm: Processed B-scan

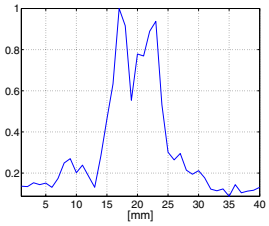

(p) $\Delta d = 7$ mm: Processed Profile

Figure 3.15: SAFT: 1 mm transducer.

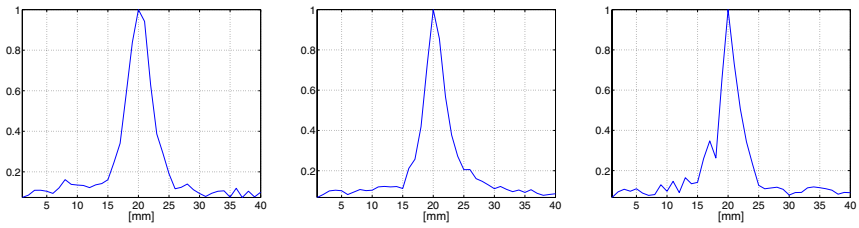

(a) $\Delta d = 1$ mm: Synthetic aperture 22 A-scans

(b) $\Delta d = 1$ mm: Synthetic aperture 30 A-scans

(c) $\Delta d = 1$ mm: Synthetic aperture 40 A-scans

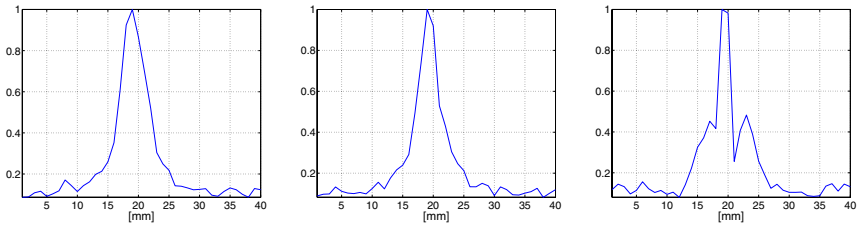

(d) $\Delta d = 3$ mm: Synthetic aperture 22 A-scans

(e) $\Delta d = 3$ mm: Synthetic aperture 30 A-scans

(f) $\Delta d = 3$ mm: Synthetic aperture 40 A-scans

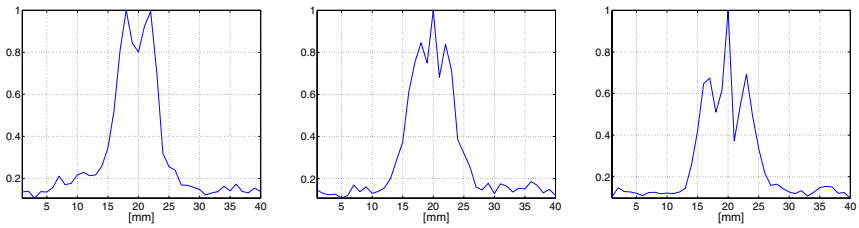

(g) $\Delta d = 5$ mm: Synthetic aperture 22 A-scans

(h) $\Delta d = 5$ mm: Synthetic aperture 30 A-scans

(i) $\Delta d = 5$ mm: Synthetic aperture 40 A-scans

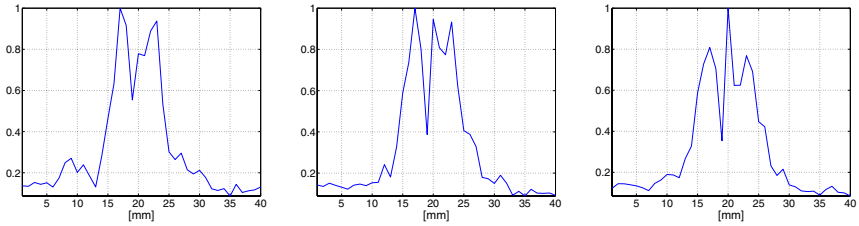

(j) $\Delta d = 7$ mm: Synthetic aperture 22 A-scans

(k) $\Delta d = 7$ mm: Synthetic aperture 30 A-scans

(l) $\Delta d = 7$ mm: Synthetic aperture 40 A-scans

Figure 3.16: Pofile plots of SAFT processed data using the 1 mm transducer using three different synthetic apertures.

3.C Results using the MMSE Method

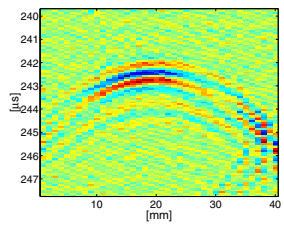

(a) $\Delta d = 1$ mm: Original B-scan

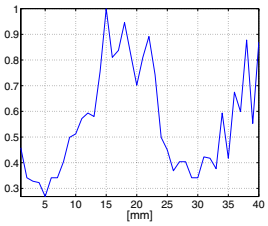

(b) $\Delta d = 1$ mm: Original Profile

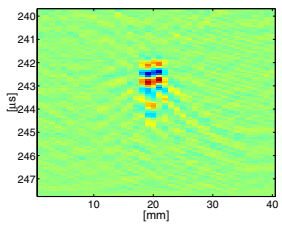

(c) $\Delta d = 1$ mm: Processed B-scan

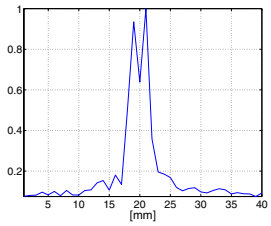

(d) $\Delta d = 1$ mm: Processed Profile

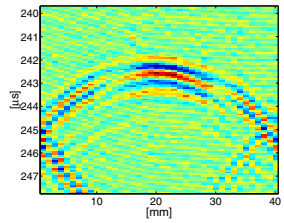

(e) $\Delta d = 3$ mm: Original B-scan

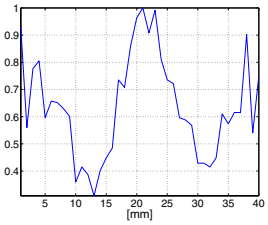

(f) $\Delta d = 3$ mm: Original Profile

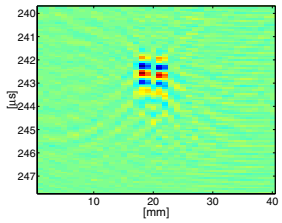

(g) $\Delta d = 3$ mm: Processed B-scan

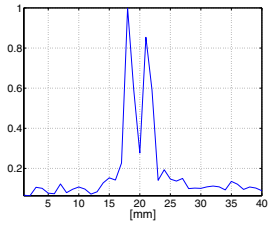

(h) $\Delta d = 3$ mm: Processed Profile

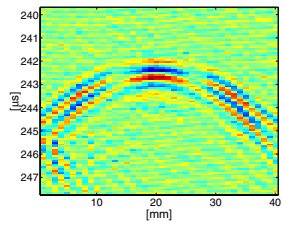

(i) $\Delta d = 5$ mm: Original B-scan

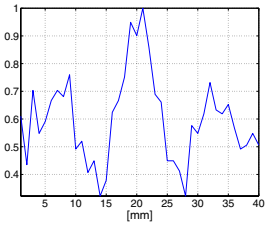

(j) $\Delta d = 5$ mm: Original Profile

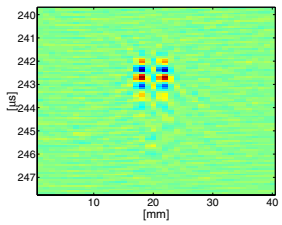

(k) $\Delta d = 5$ mm: Processed B-scan

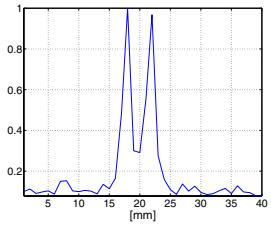

(l) $\Delta d = 5$ mm: Processed Profile

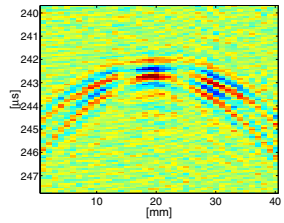

(m) $\Delta d = 7$ mm: Original B-scan

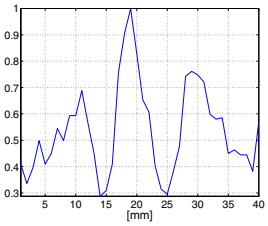

(n) $\Delta d = 7$ mm: Original Profile

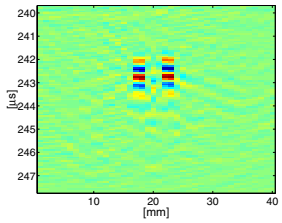

(o) $\Delta d = 7$ mm: Processed B-scan

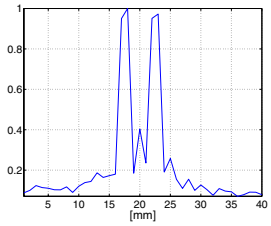

(p) $\Delta d = 7$ mm: Processed Profile

Figure 3.17: MMSE: 1 mm transducer.

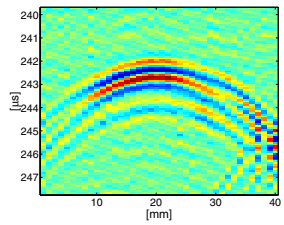

(a) $\Delta d = 1$ mm: Original B-scan

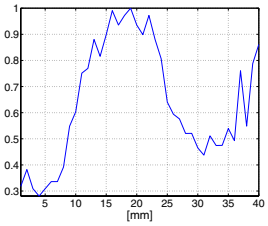

(b) $\Delta d = 1$ mm: Original Profile

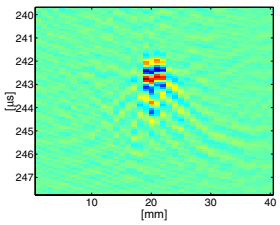

(c) $\Delta d = 1$ mm: Processed B-scan

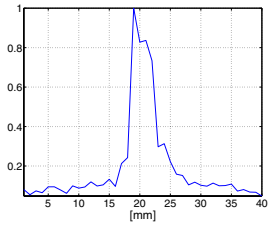

(d) $\Delta d = 1$ mm: Processed Profile

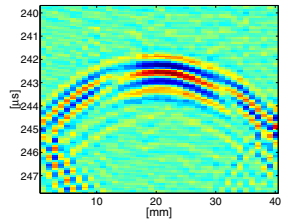

(e) $\Delta d = 3$ mm: Original B-scan

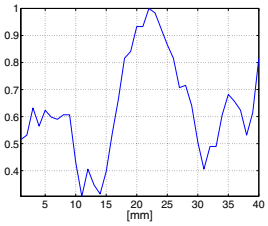

(f) $\Delta d = 3$ mm: Original Profile

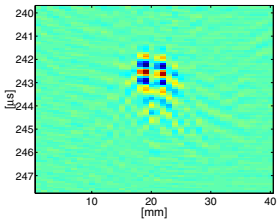

(g) $\Delta d = 3$ mm: Processed B-scan

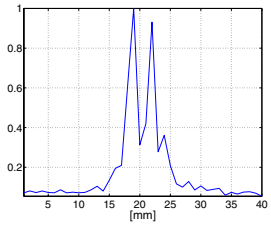

(h) $\Delta d = 3$ mm: Processed Profile

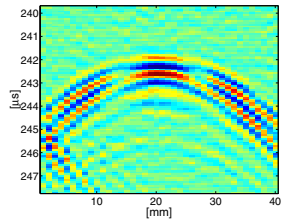

(i) $\Delta d = 5$ mm: Original B-scan

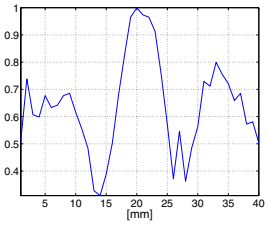

(j) $\Delta d = 5$ mm: Original Profile

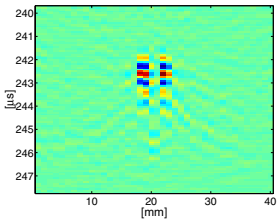

(k) $\Delta d = 5$ mm: Processed B-scan

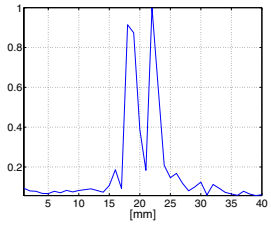

(l) $\Delta d = 5$ mm: Processed Profile

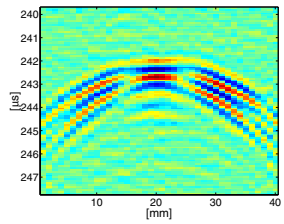

(m) $\Delta d = 7$ mm: Original B-scan

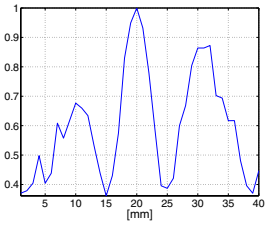

(n) $\Delta d = 7$ mm: Original Profile

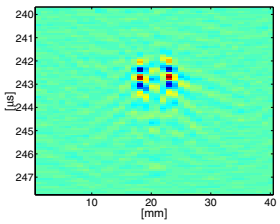

(o) $\Delta d = 7$ mm: Processed B-scan

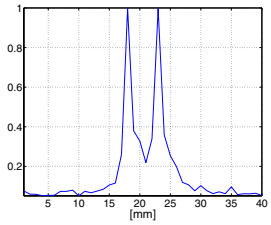

(p) $\Delta d = 7$ mm: Processed Profile

Figure 3.18: MMSE: 2 mm transducer.

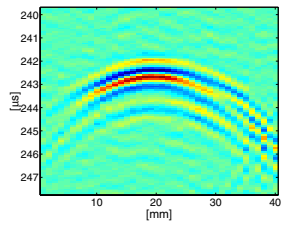

(a) $\Delta d = 1$ mm: Original B-scan

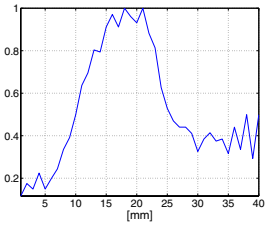

(b) $\Delta d = 1$ mm: Original Profile

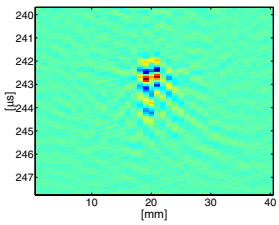

(c) $\Delta d = 1$ mm: Processed B-scan

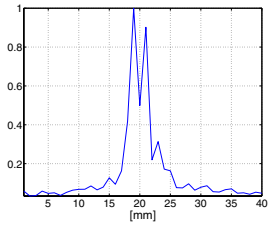

(d) $\Delta d = 1$ mm: Processed Profile

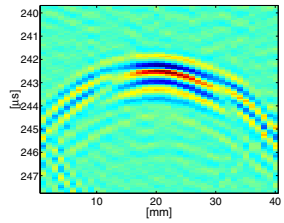

(e) $\Delta d = 3$ mm: Original B-scan

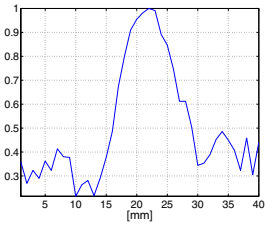

(f) $\Delta d = 3$ mm: Original Profile

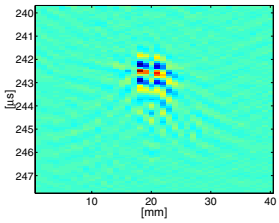

(g) $\Delta d = 3$ mm: Processed B-scan

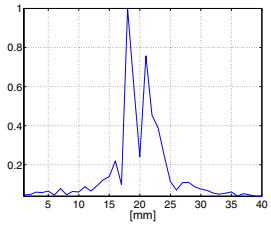

(h) $\Delta d = 3$ mm: Processed Profile

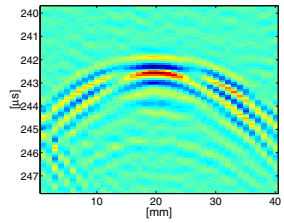

(i) $\Delta d = 5$ mm: Original B-scan

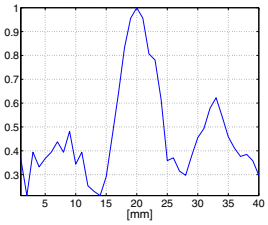

(j) $\Delta d = 5$ mm: Original Profile

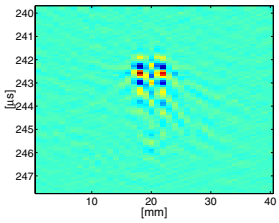

(k) $\Delta d = 5$ mm: Processed B-scan

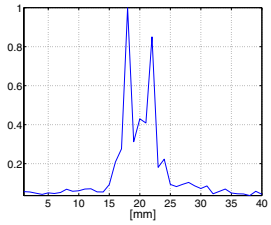

(l) $\Delta d = 5$ mm: Processed Profile

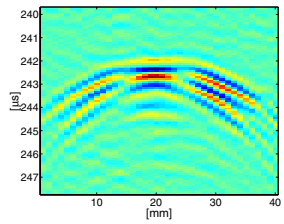

(m) $\Delta d = 7$ mm: Original B-scan

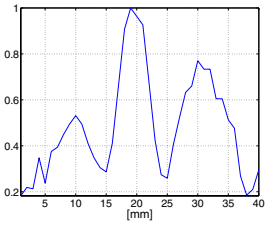

(n) $\Delta d = 7$ mm: Original Profile

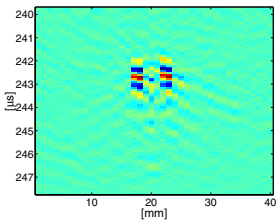

(o) $\Delta d = 7$ mm: Processed B-scan

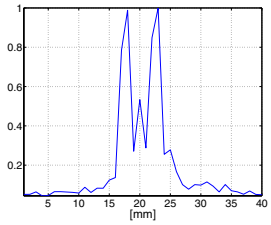

(p) $\Delta d = 7$ mm: Processed Profile

Figure 3.19: MMSE: 3 mm transducer.

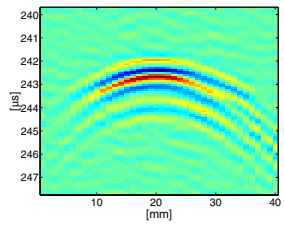

(a) $\Delta d = 1$ mm: Original B-scan

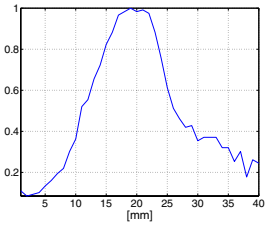

(b) $\Delta d = 1$ mm: Original Profile

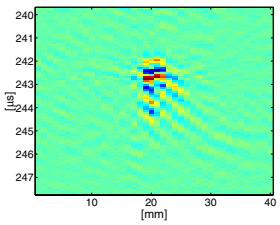

(c) $\Delta d = 1$ mm: Processed B-scan

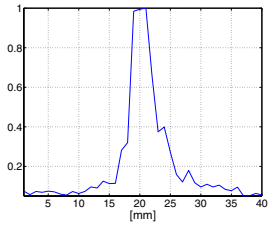

(d) $\Delta d = 1$ mm: Processed Profile

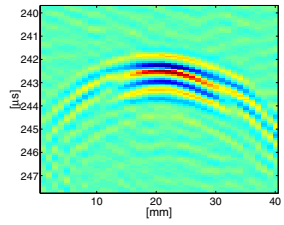

(e) $\Delta d = 3$ mm: Original B-scan

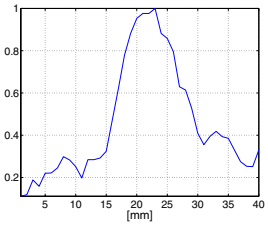

(f) $\Delta d = 3$ mm: Original Profile

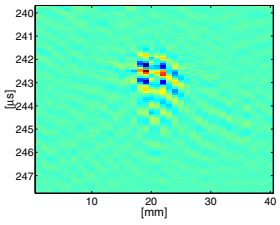

(g) $\Delta d = 3$ mm: Processed B-scan

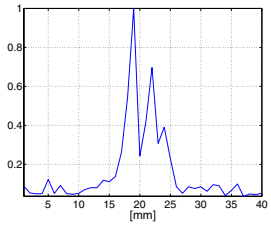

(h) $\Delta d = 3$ mm: Processed Profile

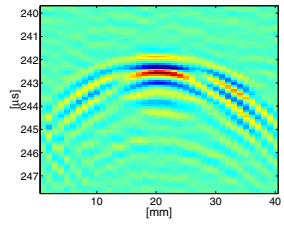

(i) $\Delta d = 5$ mm: Original B-scan

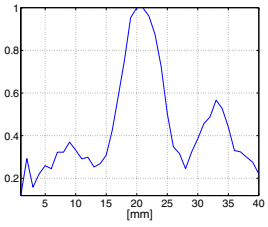

(j) $\Delta d = 5$ mm: Original Profile

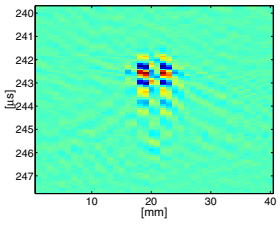

(k) $\Delta d = 5$ mm: Processed B-scan

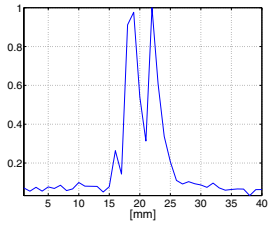

(l) $\Delta d = 5$ mm: Processed Profile

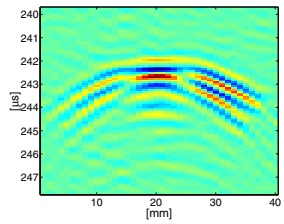

(m) $\Delta d = 7$ mm: Original B-scan

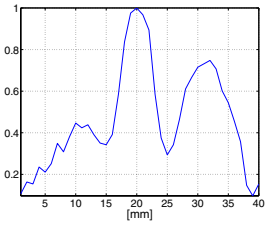

(n) $\Delta d = 7$ mm: Original Profile

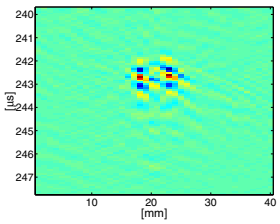

(o) $\Delta d = 7$ mm: Processed B-scan

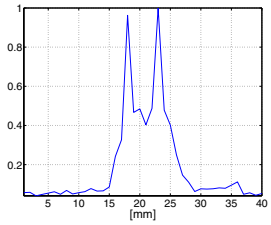

(p) $\Delta d = 7$ mm: Processed Profile

Figure 3.20: MMSE: 4 mm transducer.

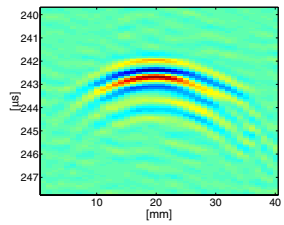

(a) $\Delta d = 1$ mm: Original B-scan

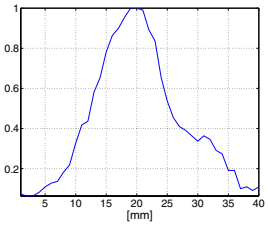

(b) $\Delta d = 1$ mm: Original Profile

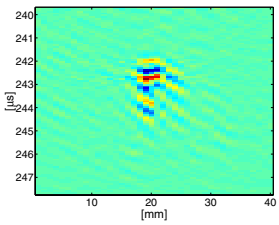

(c) $\Delta d = 1$ mm: Processed B-scan

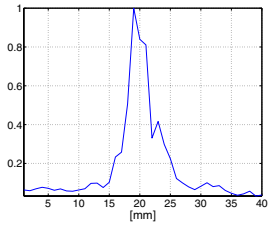

(d) $\Delta d = 1$ mm: Processed Profile

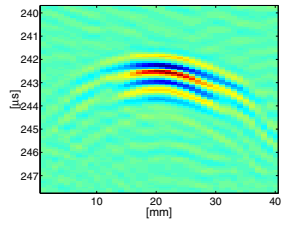

(e) $\Delta d = 3$ mm: Original B-scan

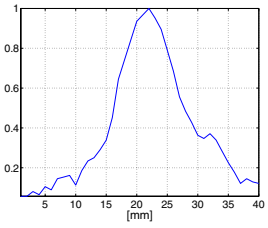

(f) $\Delta d = 3$ mm: Original Profile

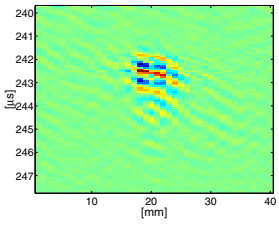

(g) $\Delta d = 3$ mm: Processed B-scan

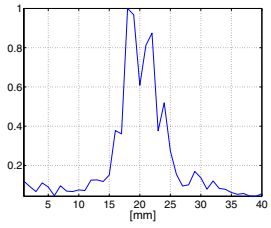

(h) $\Delta d = 3$ mm: Processed Profile

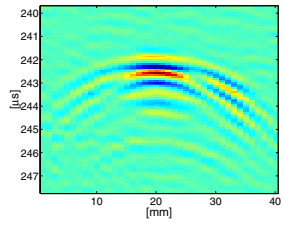

(i) $\Delta d = 5$ mm: Original B-scan

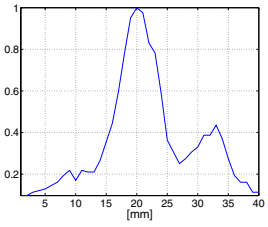

(j) $\Delta d = 5$ mm: Original Profile

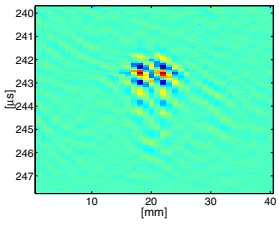

(k) $\Delta d = 5$ mm: Processed B-scan

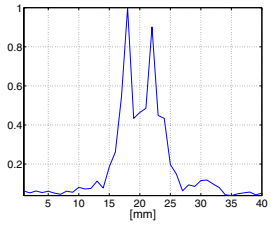

(l) $\Delta d = 5$ mm: Processed Profile

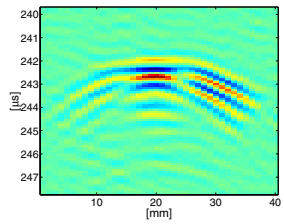

(m) $\Delta d = 7$ mm: Original B-scan

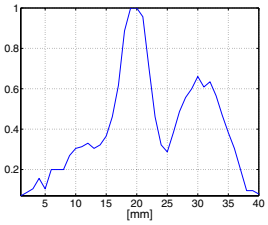

(n) $\Delta d = 7$ mm: Original Profile

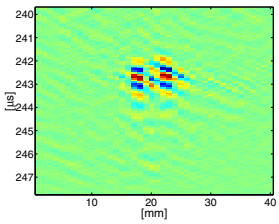

(o) $\Delta d = 7$ mm: Processed B-scan

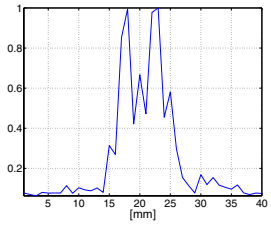

(p) $\Delta d = 7$ mm: Processed Profile

Figure 3.21: MMSE: 5 mm transducer.

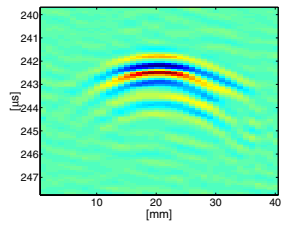

(a) $\Delta d = 1$ mm: Original B-scan

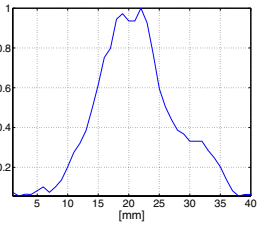

(b) $\Delta d = 1$ mm: Original Profile

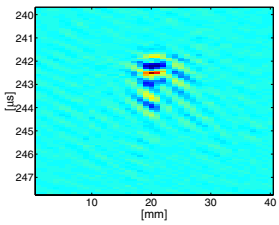

(c) $\Delta d = 1$ mm: Processed B-scan

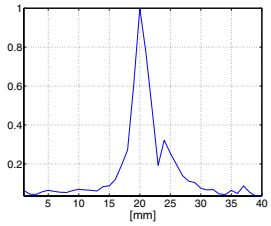

(d) $\Delta d = 1$ mm: Processed Profile

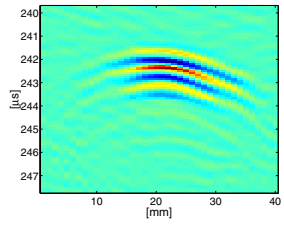

(e) $\Delta d = 3$ mm: Original B-scan

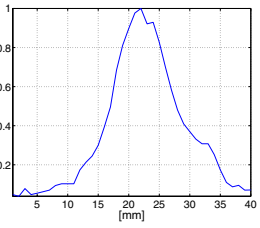

(f) $\Delta d = 3$ mm: Original Profile

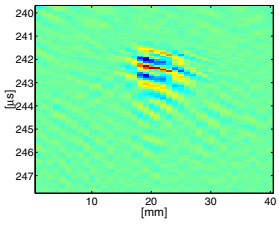

(g) $\Delta d = 3$ mm: Processed B-scan

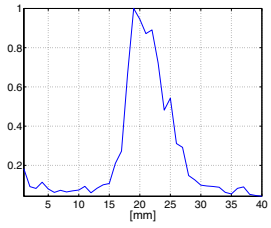

(h) $\Delta d = 3$ mm: Processed Profile

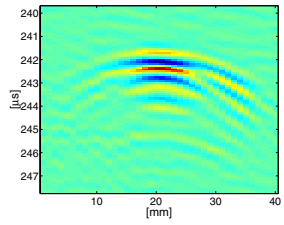

(i) $\Delta d = 5$ mm: Original B-scan

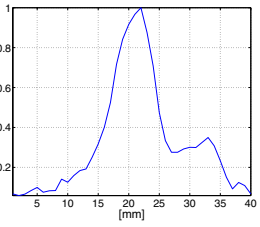

(j) $\Delta d = 5$ mm: Original Profile

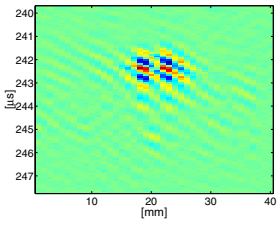

(k) $\Delta d = 5$ mm: Processed B-scan

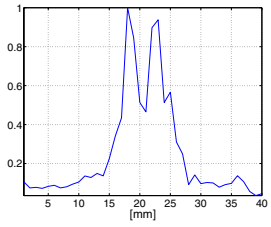

(l) $\Delta d = 5$ mm: Processed Profile

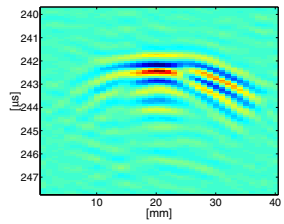

(m) $\Delta d = 7$ mm: Original B-scan

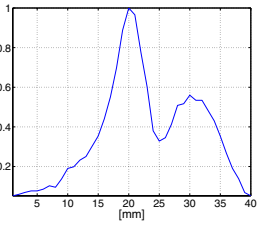

(n) $\Delta d = 7$ mm: Original Profile

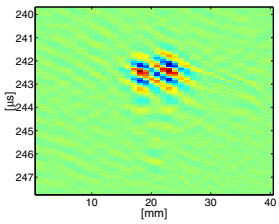

(o) $\Delta d = 7$ mm: Processed B-scan

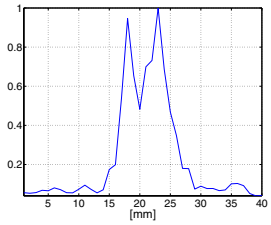

(p) $\Delta d = 7$ mm: Processed Profile

Figure 3.22: MMSE: 6 mm transducer.

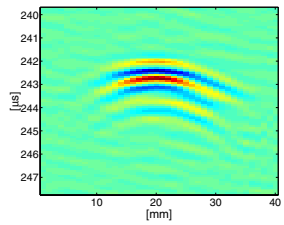

(a) $\Delta d = 1$ mm: Original B-scan

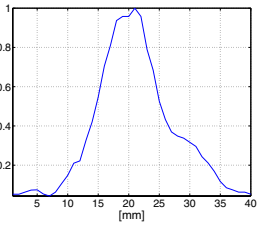

(b) $\Delta d = 1$ mm: Original Profile

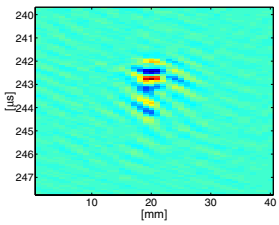

(c) $\Delta d = 1$ mm: Processed B-scan

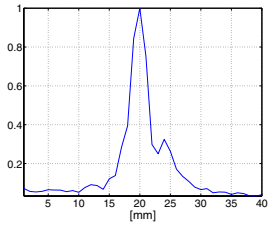

(d) $\Delta d = 1$ mm: Processed Profile

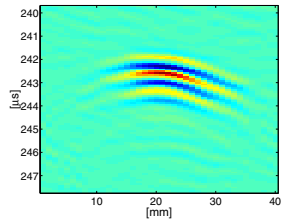

(e) $\Delta d = 3$ mm: Original B-scan

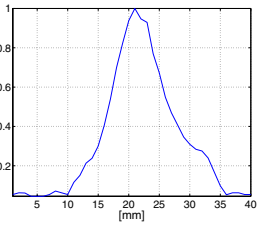

(f) $\Delta d = 3$ mm: Original Profile

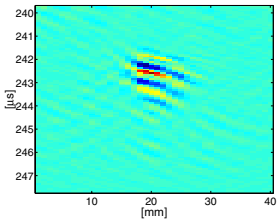

(g) $\Delta d = 3$ mm: Processed B-scan

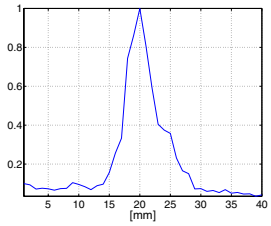

(h) $\Delta d = 3$ mm: Processed Profile

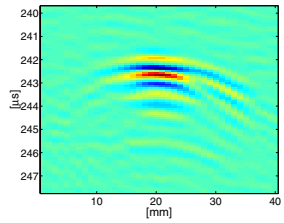

(i) $\Delta d = 5$ mm: Original B-scan

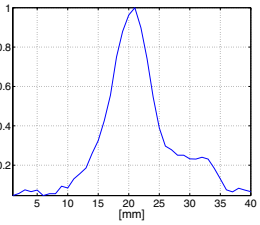

(j) $\Delta d = 5$ mm: Original Profile

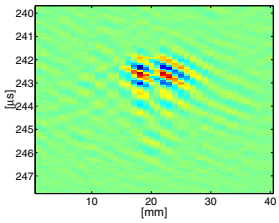

(k) $\Delta d = 5$ mm: Processed B-scan

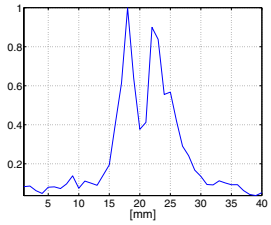

(l) $\Delta d = 5$ mm: Processed Profile

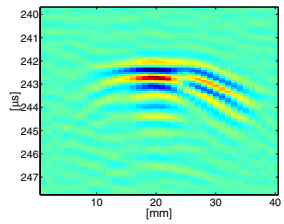

(m) $\Delta d = 7$ mm: Original B-scan

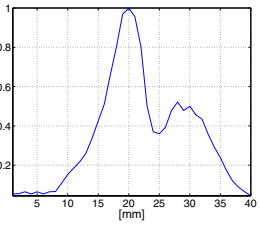

(n) $\Delta d = 7$ mm: Original Profile

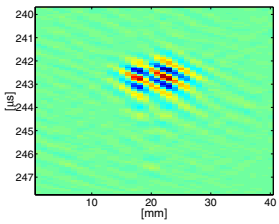

(o) $\Delta d = 7$ mm: Processed B-scan

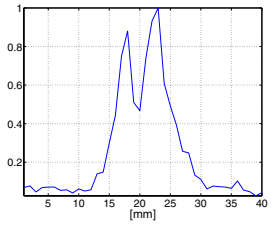

(p) $\Delta d = 7$ mm: Processed Profile

Figure 3.23: MMSE: 7 mm transducer.

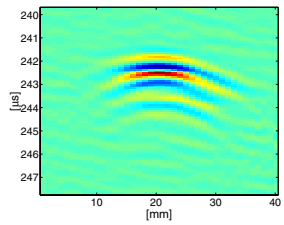

(a) $\Delta d = 1$ mm: Original B-scan

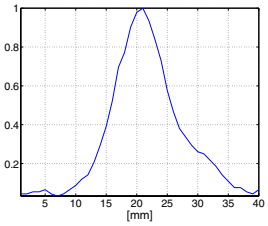

(b) $\Delta d = 1$ mm: Original Profile

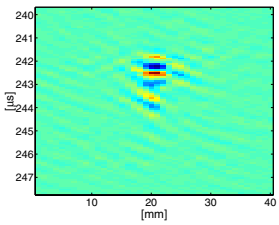

(c) $\Delta d = 1$ mm: Processed B-scan

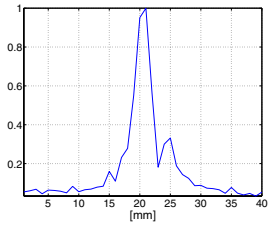

(d) $\Delta d = 1$ mm: Processed Profile

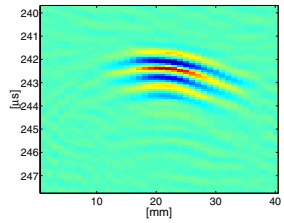

(e) $\Delta d = 3$ mm: Original B-scan

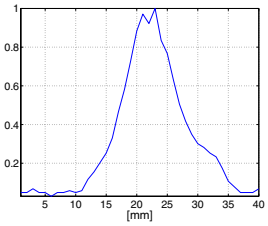

(f) $\Delta d = 3$ mm: Original Profile

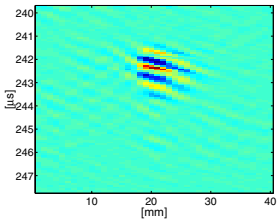

(g) $\Delta d = 3$ mm: Processed B-scan

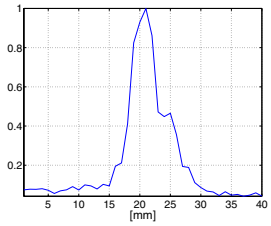

(h) $\Delta d = 3$ mm: Processed Profile

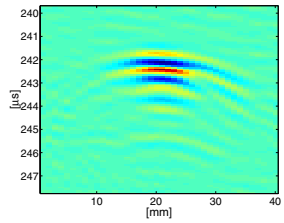

(i) $\Delta d = 5$ mm: Original B-scan

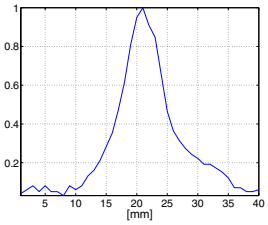

(j) $\Delta d = 5$ mm: Original Profile

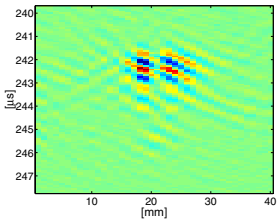

(k) $\Delta d = 5$ mm: Processed B-scan

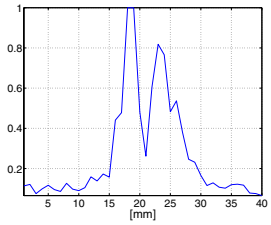

(l) $\Delta d = 5$ mm: Processed Profile

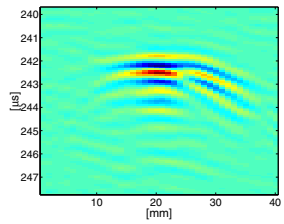

(m) $\Delta d = 7$ mm: Original B-scan

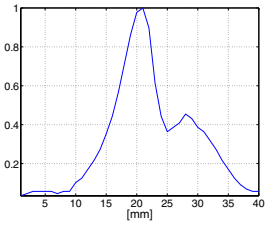

(n) $\Delta d = 7$ mm: Original Profile

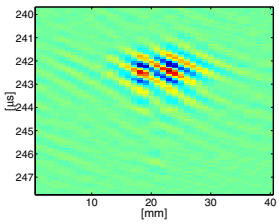

(o) $\Delta d = 7$ mm: Processed B-scan

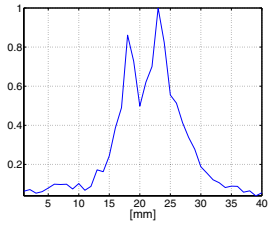

(p) $\Delta d = 7$ mm: Processed Profile

Figure 3.24: MMSE: 8 mm transducer.

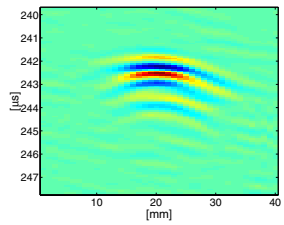

(a) $\Delta d = 1$ mm: Original B-scan

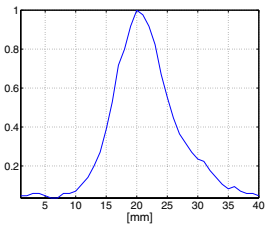

(b) $\Delta d = 1$ mm: Original Profile

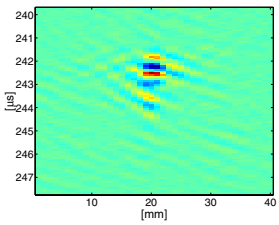

(c) $\Delta d = 1$ mm: Processed B-scan

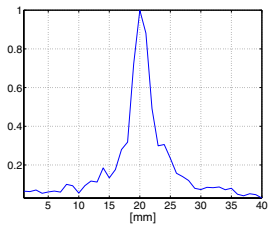

(d) $\Delta d = 1$ mm: Processed Profile

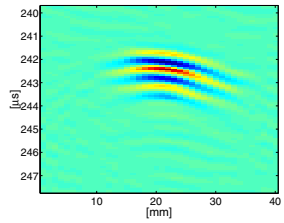

(e) $\Delta d = 3$ mm: Original B-scan

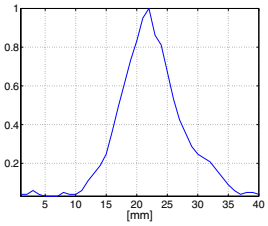

(f) $\Delta d = 3$ mm: Original Profile

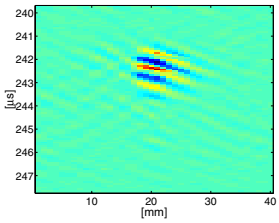

(g) $\Delta d = 3$ mm: Processed B-scan

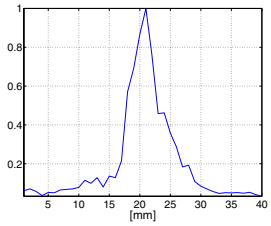

(h) $\Delta d = 3$ mm: Processed Profile

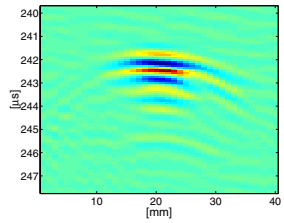

(i) $\Delta d = 5$ mm: Original B-scan

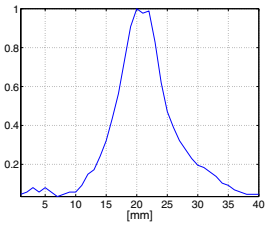

(j) $\Delta d = 5$ mm: Original Profile

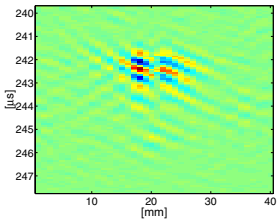

(k) $\Delta d = 5$ mm: Processed B-scan

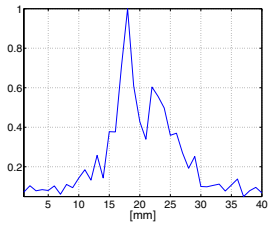

(l) $\Delta d = 5$ mm: Processed Profile

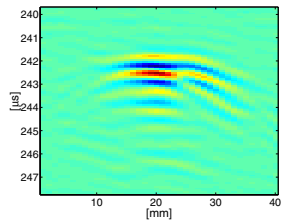

(m) $\Delta d = 7$ mm: Original B-scan

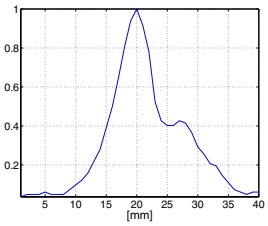

(n) $\Delta d = 7$ mm: Original Profile

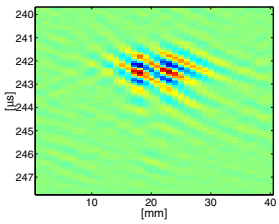

(o) $\Delta d = 7$ mm: Processed B-scan

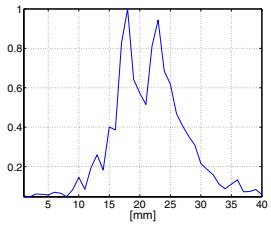

(p) $\Delta d = 7$ mm: Processed Profile

Figure 3.25: MMSE: 9 mm transducer.

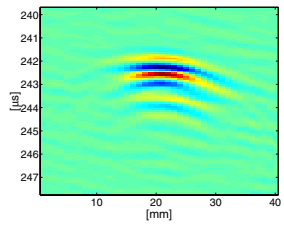

(a) $\Delta d = 1$ mm: Original B-scan

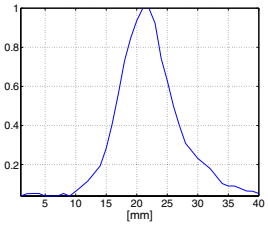

(b) $\Delta d = 1$ mm: Original Profile

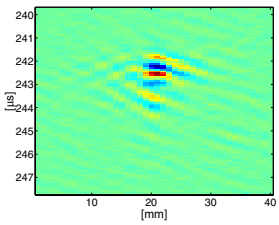

(c) $\Delta d = 1$ mm: Processed B-scan

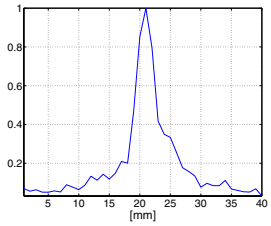

(d) $\Delta d = 1$ mm: Processed Profile

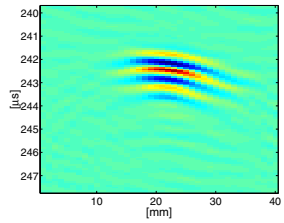

(e) $\Delta d = 3$ mm: Original B-scan

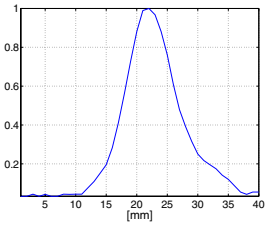

(f) $\Delta d = 3$ mm: Original Profile

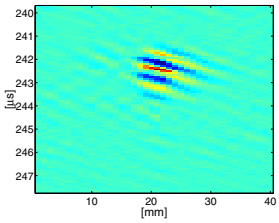

(g) $\Delta d = 3$ mm: Processed B-scan

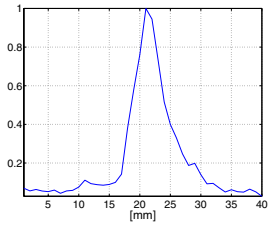

(h) $\Delta d = 3$ mm: Processed Profile

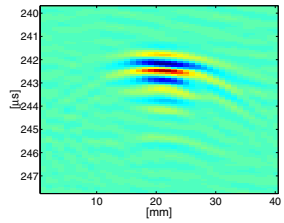

(i) $\Delta d = 5$ mm: Original B-scan

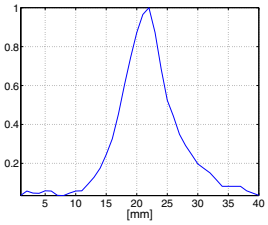

(j) $\Delta d = 5$ mm: Original Profile

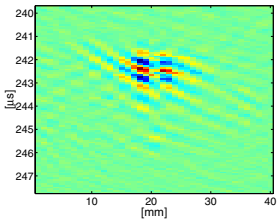

(k) $\Delta d = 5$ mm: Processed B-scan

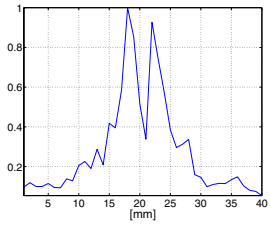

(l) $\Delta d = 5$ mm: Processed Profile

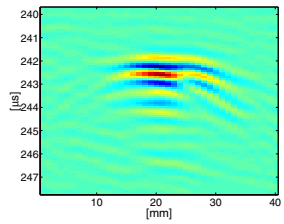

(m) $\Delta d = 7$ mm: Original B-scan

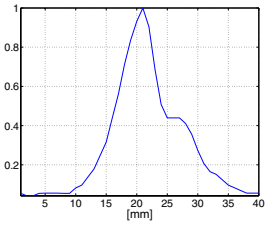

(n) $\Delta d = 7$ mm: Original Profile

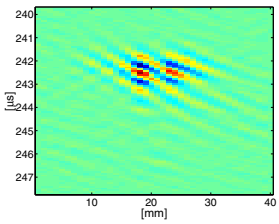

(o) $\Delta d = 7$ mm: Processed B-scan

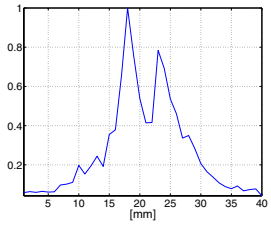

(p) $\Delta d = 7$ mm: Processed Profile

Figure 3.26: MMSE: 10 mm transducer.

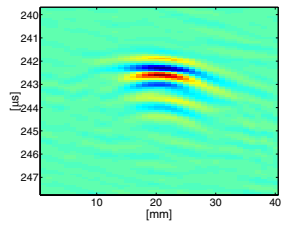

(a) $\Delta d = 1$ mm: Original B-scan

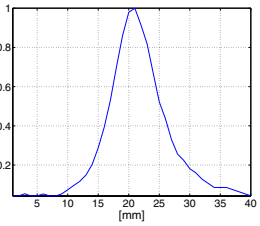

(b) $\Delta d = 1$ mm: Original Profile

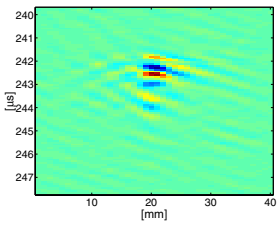

(c) $\Delta d = 1$ mm: Processed B-scan

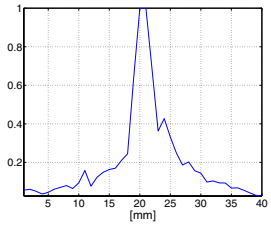

(d) $\Delta d = 1$ mm: Processed Profile

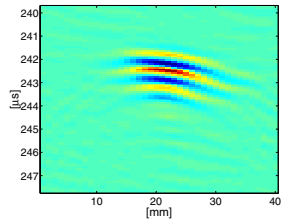

(e) $\Delta d = 3$ mm: Original B-scan

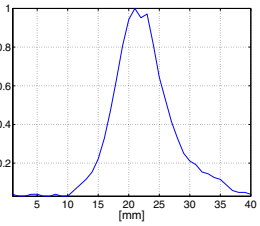

(f) $\Delta d = 3$ mm: Original Profile

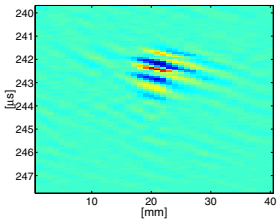

(g) $\Delta d = 3$ mm: Processed B-scan

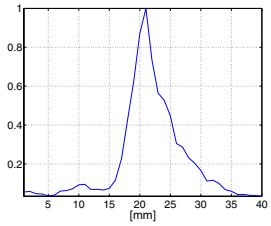

(h) $\Delta d = 3$ mm: Processed Profile

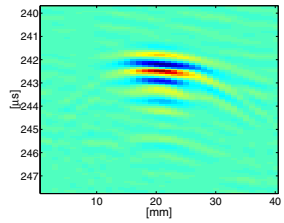

(i) $\Delta d = 5$ mm: Original B-scan

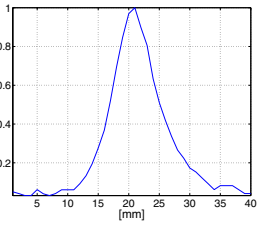

(j) $\Delta d = 5$ mm: Original Profile

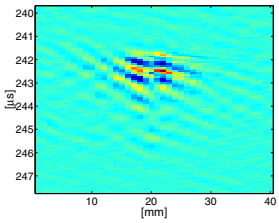

(k) $\Delta d = 5$ mm: Processed B-scan

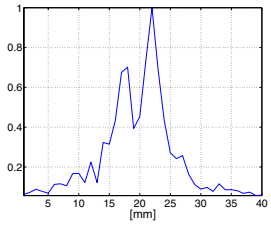

(l) $\Delta d = 5$ mm: Processed Profile

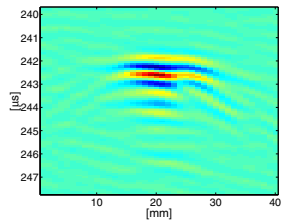

(m) $\Delta d = 1$ mm: Original B-scan

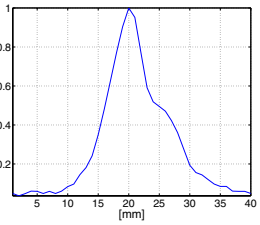

(n) $\Delta d = 7$ mm: Original Profile

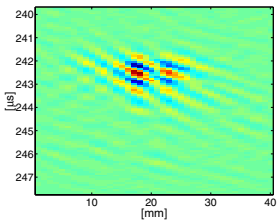

(o) $\Delta d = 7$ mm: Processed B-scan

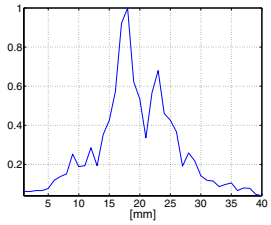

(p) $\Delta d = 7$ mm: Processed Profile

Figure 3.27: MMSE: 11 mm transducer.

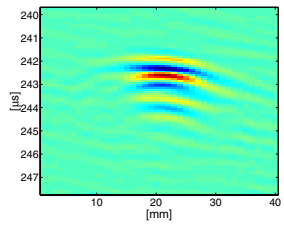

(a) $\Delta d = 1$ mm: Original B-scan

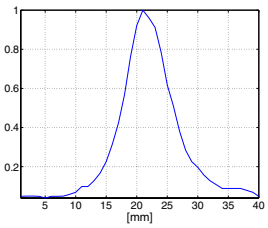

(b) $\Delta d = 1$ mm: Original Profile

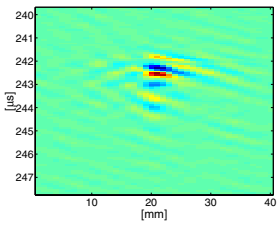

(c) $\Delta d = 1$ mm: Processed B-scan

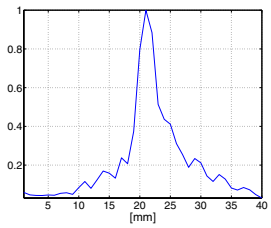

(d) $\Delta d = 1$ mm: Processed Profile

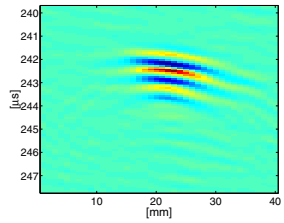

(e) $\Delta d = 3$ mm: Original B-scan

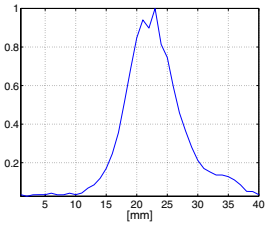

(f) $\Delta d = 3$ mm: Original Profile

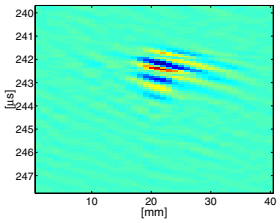

(g) $\Delta d = 3$ mm: Processed B-scan

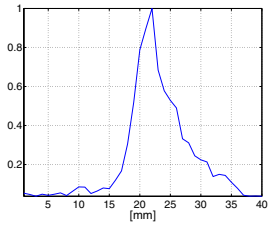

(h) $\Delta d = 3$ mm: Processed Profile

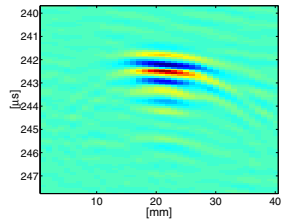

(i) $\Delta d = 5$ mm: Original B-scan

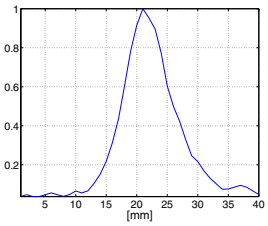

(j) $\Delta d = 5$ mm: Original Profile

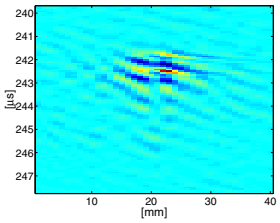

(k) $\Delta d = 5$ mm: Processed B-scan

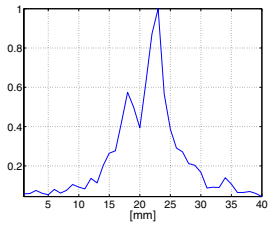

(l) $\Delta d = 5$ mm: Processed Profile

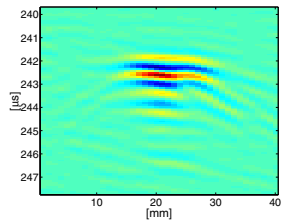

(m) $\Delta d = 7$ mm: Original B-scan

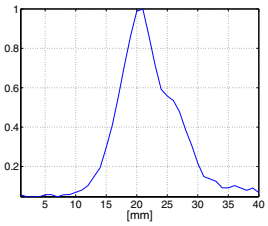

(n) $\Delta d = 7$ mm: Original Profile

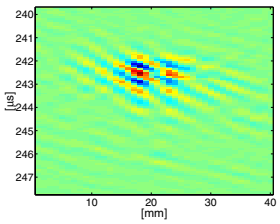

(o) $\Delta d = 7$ mm: Processed B-scan

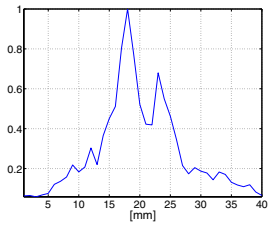

(p) $\Delta d = 7$ mm: Processed Profile

Figure 3.28: MMSE: 12 mm transducer.

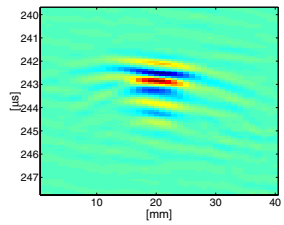

(a) $\Delta d = 1$ mm: Original B-scan

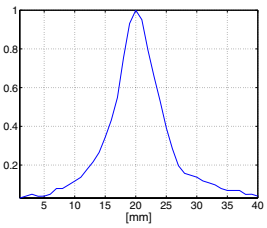

(b) $\Delta d = 1$ mm: Original Profile

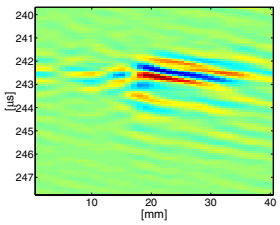

(c) $\Delta d = 1$ mm: Processed B-scan

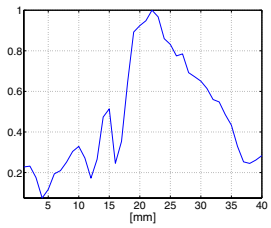

(d) $\Delta d = 1$ mm: Processed Profile

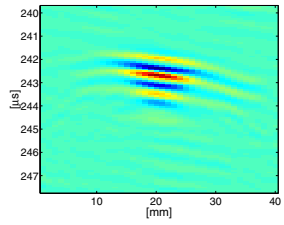

(e) $\Delta d = 3$ mm: Original B-scan

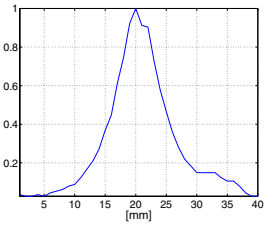

(f) $\Delta d = 3$ mm: Original Profile

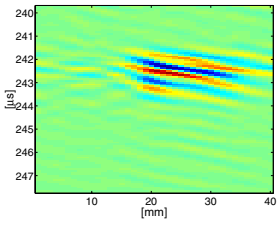

(g) $\Delta d = 3$ mm: Processed B-scan

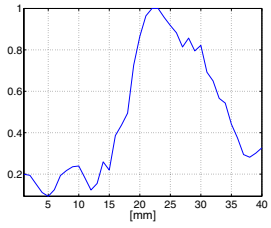

(h) $\Delta d = 3$ mm: Processed Profile

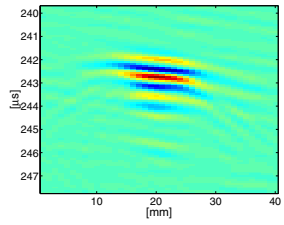

(i) $\Delta d = 5$ mm: Original B-scan

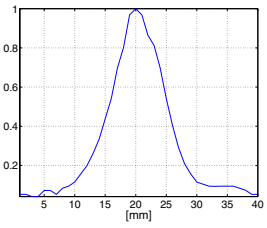

(j) $\Delta d = 5$ mm: Original Profile

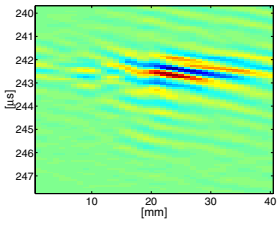

(k) $\Delta d = 5$ mm: Processed B-scan

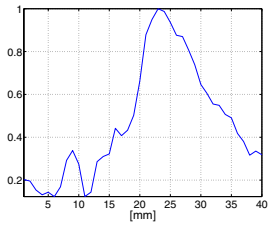

(l) $\Delta d = 5$ mm: Processed Profile

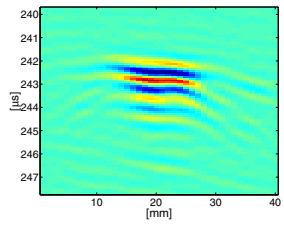

(m) $\Delta d = 7$ mm: Original B-scan

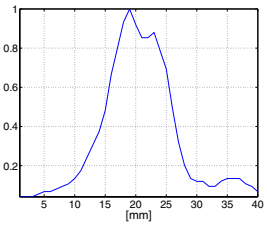

(n) $\Delta d = 7$ mm: Original Profile

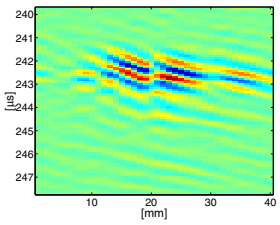

(o) $\Delta d = 7$ mm: Processed B-scan

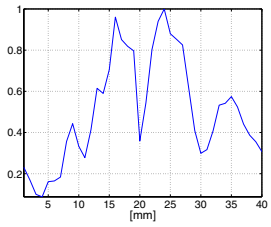

(p) $\Delta d = 7$ mm: Processed Profile

Figure 3.29: MMSE: 20 mm transducer.